Analysis of Liquefaction Induced Lateral Ground Displacement Using Smoothed Particle Hydrodynamics

Graduate School of Systems and Information Engineering

University of Tsukuba

March 2006

NAILI Mounir

Analysis of Liquefaction Induced Lateral Ground Displacement Using Smoothed Particle Hydrodynamics

NAILI Mounir

Dissertation submitted to the Graduate School of Systems and Information Engineering, University of Tsukuba in partial fulfillment of the requirements for the degree of Doctor of Philosophy in Engineering

March 2006

Abstract

This research introduces a smoothed particle hydrodynamics (SPH) technique to analyze liquefaction induced ground displacements in the framework of fluid dynamics concept.

Lateral spreading induced by seismic liquefaction causes the ground to experience large displacement and shear strains which are difficult to simulate by ordinary techniques like FEM, FDM or VOF. In this respect, the primary objective of this research was to investigate the applicability and feasibility of a Lagrangian meshfree particle method to analyze problems involving large ground displacements.

On the basis of field observations and laboratory tests findings on the mechanism of liquefaction induced lateral spreading as well as on the nature of the liquefied soil, the viscous fluid analogy and the Bingham constitutive model was used to represent the behavior of the liquefied subsoil.

The ability and the efficiency of the SPH to simulate Newtonian and non-Newtonian flow was checked using three benchmark problems for which exact solution and experimental results exist. The method was then extended to simulate lateral spreading experiments conducted on 1g shaking table test by Hamada et al. and to investigate the flow of the liquefied soil around a model pile. The dilatancy propriety of the liquefied soil was simulated by introducing a phenomenological bilinear constitutive model to reproduce the regain of the rigidity. The obtained results show that the SPH technique represents a powerful and promising tool to simulate large displacement, large shear strain and to track the free surface without any need for remeshing techniques.

CONTENTS

List of tables

List of figures

Acknowledgments

I would like to express my deepest thanks and gratitude to Professor Yasuo Yamada my supervisor, for giving me the opportunity to join his laboratory and conduct this research. Without his guidance, encouragement, patience, help and support, this research would not have been completed.

My thanks are extended to Associate Professor Takashi Matsushima for the fruitful discussions we had, as well as for the instructive and constructive advices that gave more insights and ideas to this research.

I am also thankful to the dissertation committee members, Professor Hiroshi Miki, Associate Professor Harumichi Kyotoh and Assistant Professor Gaku Shoji for reviewing this thesis and for their comments and suggestions.

I am thankful to Dr Mohamed Belazougui, Director of the National Center for Applied Research in Earthquake Engineering, Algiers, for allowing my leave and giving me the opportunity to pursue my doctoral studies.

I am grateful to my parents and to my wife for their understanding, encouragement and support throughout the course of this research.

Finally, I would like to thank the members of the Geotechnical Engineering laboratory for the friendly and warm working atmosphere, without forgetting Dr Hidetaka Saomoto, a former member in our laboratory for the fruitful discussions we had particularly in programming issues.

Chapter 1

Introduction

1.1 Research background

Liquefaction of loose, saturated, cohesionless soils and other granular materials represents one of the most devastating geotechnical hazards during large earthquakes. For instance, liquefaction induced ground failures have caused tremendous damage and disruption to pile foundations of buildings and bridges, embankments, river dikes, pipelines, lifelines system and waterfront structures. During the 1964 Alaska earthquake, over 250 bridges and numerous embankments along the Alaskan Railroad and Highway were damaged. In the same year, the Niigata earthquake caused substantial damage in Niigata city and its vicinity. Earth structures and foundations were severely affected due to liquefaction of saturated loose sand (Yamada, 1966). According to Kawakami and Asada (1966), structures in harbors and revetments of river banks moved, tilted or overturned. In Niigata Power Plant, cast iron pipes of 1500 mm in diameter for cooling water supply moved upward by 50 cm and sideways by 110 cm, although they were full of water and laid at 4m depth. Liquefaction induced lateral spread caused also extensive damage to Showa Bridge as its pile foundations could not resist the cumulative movement of the laterally spreading soil, leading them to deflect toward the river's centerline and cause the collapse of several bridge spans. During the 1995 Hyogo-ken Nanbu earthquake, soil liquefaction caused widespread damage on reclaimed lands and induced large ground displacements in the horizontal direction, resulting in distress to buried lifelines and piles foundations of buildings and bridge piers along the Kobe shoreline (Hamada et al, 1996). Lateral spread at the margins of Port Island and Rokko Islands caused widespread seaward displacement of caisson walls that

severely disrupted port operations (Inagaki et al, 1996). At Takahama in Kobe, wharves supported on vertical piles moved 1.3–1.7 m toward the sea. Furthermore, in Nishinomiya area, ground displacement in the order of 2 m caused the caisson type foundation supporting the Nishinomiya Bridge to move about 0.6 m resulting in the collapse of a girder.

By reviewing and analyzing four case studies from past Japanese earthquakes namely the 1923 Kanto earthquake, Fukui earthquake of 1948, the 1964 Niigata earthquake and the 1983 Nihonkai-Chubu earthquake, Doi and Hamada (1992) investigated the mechanism of the occurrence of liquefaction induced ground displacements and its influence on underground structures. They showed that the resultant damage may extend over a region of hundreds square meters and the permanent displacements may reach several meters even for mild ground slope. They stated that during Fukui earthquake, the maximum observed displacement in Morita area was greater than 4 m, and during Niigata earthquake, the maximum displacement reached 8 m in Ohgata area (Fig.1.1). Using the GPS before and after the Hyogoken-Nambu earthquake, Inagaki et al. (1996) measured the induced displacements along the Rokko Island and Port Island, and found that a quay wall line in the northern area of Port Island moved about 4 m toward the north, while the sea wall along the north end of the Rokko Island moved 3.5 m toward the sea at the maximum (Fig.1.2).

1.2 Purpose of the present research

In view of the previous post-earthquakes investigations, we can state that bridges, buildings and waterfronts structures lost their stability and serviceability due to the deficiency of their foundations to resist the load imposed by the surrounding soil, while pipelines, lifelines systems (gas and fuel delivery, water supply and sewage), and embankments lost their functionality due to their inability to sustain large displacements and deformations caused by the lateral spread. In order to protect these structures and to ensure their stability and serviceability during and after the earthquake shaking, the assessment of the likelihood *induced permanent*

displacement and *lateral spreading load* is a matter of great concern in seismic proof design.

In the framework of performance based seismic design, the magnitude of the induced ground displacement is considered to be a major factor in designing in-ground structures. In fact, the current approach tends towards allowing the induced deformations to be within an acceptable level even if the subsoil liquefies, rather than preventing overall liquefaction by taking preventive countermeasures.

The primary objective of the present work is to develop a numerical approach based on smoothed particle hydrodynamics (SPH) for liquefaction induced lateral spreading analysis. By essence, the SPH is an adaptive Lagrangian meshfree particle technique that is capable of modeling large displacement and tracking free surface boundary. However, its application and extension to the field of geomechanic has been only recently attempted. Zhu et al. (1999) developed a pore-scale numerical model for flow through porous media using SPH. Using the same numerical technique, Maeda and Sakai (2004) were able to model seepage analysis of granular flow, and Saomoto (2004) used a coupled DEM-SPH technique to model boiling problem.

On the other hand, although many studies were carried out to investigate the characteristics of the liquefied soil, the relationship between the stress and the strain which reaches sometimes 100 % is difficult to establish. In this study, the approach is developed within the framework of fluid dynamics by considering the soil to behave as a viscous fluid during shaking and as a solid after the cease of shaking. In this case, a constitutive model that simulates both behaviors is expressed in the form of a non-Newtonian fluid and its implementation allows the assessment of large displacement.

1.3 Previous research

Several models have been developed to predict the magnitude of the liquefaction induced ground displacements. They can be classified into the following categories:

- Empirical methods
- Numerical methods
- Simplified analytical methods.

- **Empirical methods**

Several empirical methods to predict liquefaction induced ground displacements have been developed by deriving the relationship between the observed displacements and various sites parameters. In this section, three empirical models for lateral spread will be reviewed.

Using data from the 1964 Niigata, the 1983 Nihonkai-chubu and the 1971 San Fernando earthquakes, Hamada et al. (1986) developed a simple empirical model for horizontal displacements expressed in the following form:

$$D = 0.75\sqrt{H}\sqrt[3]{\theta} \qquad (1.1)$$

Where D is the horizontal displacement (m), H is the thickness (m) of the estimated liquefied layer and θ (%) is the larger value of the slope of either the ground surface or the base of the liquefied layer. However, Hamada et al (1994) reported that the proposed formula provides only an approximate fit to the field data since the predicted ground displacements by the above formula are scattered between half and twice the measured values. Furthermore, most of the case observation came from Noshiro city and thus represent a narrow range of seismic data and site conditions.

Bartlett and Youd (1995) used a large database of lateral spreading case histories with multiple linear regression (MLR) analysis to derive empirical equations for ground surface displacement caused by lateral spread. In total, 467 displacements vectors compiled from eight earthquakes in Japan and Western United States were used to fit the MLR model of which, 337 are from the 1964 Niigata and 1983 Nihonkai-Chubu earthquakes and 111 are from US earthquakes. Bartlett and Youd developed two model equations: a free face component for lateral spreading toward a steep vertical face and a ground slope component for lateral spread without a free face. The derived MLR equations are expressed as:

- Free face component:

$$\begin{aligned}\log D = {} & -16.366 + 1.178M_W - 0.927\log R + 0.657\log W + \\ & 0.348\log T_{15} + 4.527\log(100 - F_{15}) - 0.922D50_{15}\end{aligned} \qquad (1.2)$$

- Ground slope component:

$$\log D = -15.787 + 1.178M_W - 0.927\log R + 0.429\log S + 0.348\log T_{15} + 4.527\log(100 - F_{15}) - 0.922D50_{15} \quad (1.3)$$

Where D is the horizontal displacement (m), M_W is the moment magnitude of the earthquake and R is the closest horizontal distance (km) to the seismic energy source of fault rupture. T_{15} is the thickness (m) of the saturated, cohensionless soils (excluding soils deeper that 20m or with ≥ 15 % clay content) with $N_{1,60} \leq 15$ ($N_{1,60}$ is the standardized SPT blowcount). F_{15} is the average fines content in T_{15} and D_{15} is the average grain size (mm) in T_{15}.

In the free surface component, W is the free surface (%) defined as the ratio between the toe-to-crest height and the horizontal distance to the face toe. For the ground slope component, S is the gradient of the ground surface (%). By looking at the data base used by Bartlett and Youd, we can see that the MLR model is valid only for $6 \leq M_W \leq 8, 1 \leq W \leq 20\%$, $0.1 \leq S \leq 6\%$, $1 \leq T_{15} \leq 15m$ and a depth to the top of the liquefied soil from 1 to 10 m.

Using the same database as Bartlett and Youd, Rauch (1997) developed an empirical procedure which includes three complementary components that could be used with different levels of site information. Rauch grouped nearby displacement vectors into individual slides and computed an average displacement D (m) and average soil properties for each slide, expressed by the following equations:

Regional: $D = (D_R - 2.21)^2 + 0.149$ $\sigma_D = 0.589D$ (1.4)

Site: $D = (D_R + D_S - 2.44)^2 + 0.111$ $\sigma_D = 0.560D$ (1.5)

Geotechnical: $D = (D_R + D_S + D_G - 2.49)^2 + 0.124$ $\sigma_D = 0.542D$ (1.6)

Where:

D_R = $(613M_W - 13.9R_f - 2420a_{\max} - 11.4T_d)/1000$

D_S = $(0.526L_{slide} + 42.3S_{top} + 31.3H_{face})/1000$

D_G = $(50.6Z_{FS\min} - 86.1Z_{liq})/1000$

R_f = the shortest horizontal distance (km) to the fault rupture.

M_W = the moment magnitude.

$a_{\max}$ = the peak horizontal acceleration at the ground surface.

T_d = the bracketed duration (s).

L_{slide} = the length (m) of slide area from head to toe.

S_{top} = the average slope (%) across the surface of the lateral spread.

H_{face} = the height (m) of the free face measured vertically from toe to crest.

$Z_{FS\min}$ = the average depth (m) to the minimum factor of safety.

Z_{liq} = the average depth (m) to the top of liquefied layer.

It is important to mention that a special care should be taken regarding the use of the empirical models for liquefaction induced ground displacement prediction, especially for conditions other than those corresponding to the database from which they were developed. This concerns the range of the recorded strong motions and site conditions. Accordingly, the use of the mechanical based methods for liquefaction induced lateral spreading seems more consistent with experimental results and field observations.

- **Numerical methods**

Numerical methods to predict the magnitude of the ground displacement induced by lateral spreading depend on our understanding of the mechanical behavior of the liquefied soil. As it will be reviewed in the next chapter, the liquefied soil may behave as a solid or as a viscous fluid during the course of the shaking.

Based on the assumption that liquefied soil behaves with a reduced stiffness after the liquefaction, Yasuda et al. (1992) proposed a simple static finite element analysis in two stages to assess the permanent ground displacement. In the first stage, the distribution of the stresses in the ground is calculated using the elastic modulus before the earthquake. In the second stage, the stresses are held constant and the analysis is conducted again using the decreased modulus due to liquefaction. Finally, the permanent displacement is obtained as the difference between the displacements computed in the two analyses.

Using the principal of the minimum potential energy, Orense and Towhata (1992) proposed a three dimensional finite element approach to predict the pattern of the ultimate permanent ground displacements induced by seismic liquefaction. The three dimensional problem is reduced to two dimensional one by dividing the study area into several finite elements and assuming a sinusoidal distribution of the lateral distribution of the liquefied soil. In the simulation, the soil is considered to have no shear stiffness, and the upper soil layer acts as a linear elastic plate.

Considering the liquefied soil as a visco-elastic material, Aydan (1995) proposed a FEM procedure based on the adaptive mesh technique to simulate the lateral spreading of the liquefied ground. The method was applied to simulate model tests of liquefied soil shaked in a large box, and it was found able to simulate the behavior of ground soil ranging from a fluid-like one to solid-like behavior one. However, this method needs both elastic and viscous parameters of the liquefied soil to be defined; the determination of the viscous ones is difficult because of their non-linearity.

Uzuoka et al. (1998) developed a numerical method to predict the lateral spreading of the liquefied subsoil based on the concept of the fluid dynamics. By assuming the liquefied soil as a Bingham fluid, Uzuoka et al used a numerical code based on the finite volume method to simulate a real flow failure of an embankment as well as the results of a lateral spreading experiment on an underground structure.

Tamate and Towhata (1999) proposed a 2D finite element approach for numerical simulation of ground flow caused by seismic liquefaction. In their approach, the soil is considered to behave like a viscous fluid, and hence the ground flow is governed by the principal of minimum potential energy. To take account of the non-linearity due to large displacement, the updated Lagrangian method was used to solve the equation of motion.

Considering the same assumption for the liquefied subsoil and using the same computational framework as Uzoka et al., Hadush et al. (2001) proposed the cubic interpolated pseudo-particle (CIP) to simulate the displacement induced by lateral spreading. The method was used to simulate results from shaking table experiments of a liquefied subsoil model with an overlaying non-liquefied layer.

In summary, a variety of numerical methods have been developed to predict ground displacement induced by lateral spreading assuming the liquefied subsoil either as a solid or as a viscous fluid. Since the induced displacements are large as observed in the field, the governing equations were solved either on an updated Lagrangian or Eulerian description. In the adaptive mesh technique based on the updated Lagrangian description, the stiffness matrix is re-calculated and re-assembled at each time increment. Furthermore, the mesh is to be re-updated which may lead to time consuming and additional inaccuracy of the solution. Similarly, the volume of fluid (VOF) based on staggered grid need special treatment to track moving boundary and interface. The CIP technique can treat different materials together and track free surface by separating the advection and non-advection phase, however some numerical instability due to the constitutive equation still unresolved. Noteworthy to mention that most of these methods, particularly those using FEM require many soil parameters to be determined through laboratory testing, and thus render them costly for use. Consequently, the use of simplified analytical models is in many cases justified.

- **Simplified analytical models**

Two simplified analytical approaches to assess the ground deformation in lateral spread have been developed based either on the Newmark's sliding block concept or on Towhata's simplified approach.

By assuming a sliding block resting on a frictional plane, Newmark (1965) assessed the resulting ground displacement when the seismic inertia force exceeded the resisting forces. This condition is expressed in term of the critical yield acceleration. The induced displacement is computed by integrating twice the seismic acceleration time history minus the critical yield acceleration. The Newmark's model assumes that the deformation takes place on a well defined failure surface and the yield acceleration remains constant during shaking. However, these assumptions do not hold in the case of lateral spreads, since the sliding block is no more rigid but liquid, and the shear strength (and yield acceleration) of saturated soils varies during cyclic loading as pore pressure varies.

On the basis of observations from shaking table experiment, Towhata et al. (1992) developed an analytical model to predict the maximum displacement that will occur during lateral spreading. By considering the soil to remain liquefied for a sufficient length of time, the lateral spreading attains a complete flow and a state of minimum energy is achieved. The horizontal deformations of a vertical section in the liquefied deposit are represented by a sinusoidal curve. The model was successfully applied to analyze various shaking table tests results and to simulate real cases in Noshiro city and Ohgata area in Niigata city.

1.4 Outline of the thesis

In chapter 1, the research background and the objectives are established on the basis of post earthquake observations and the new requirements of the performance based design. The assessment of the maximum likelihood displacement induced by lateral spreading during liquefaction represents a prerequisite for the design of in-ground structures.

Chapter 2 introduces and discusses the nature characteristic of the liquefied soil with respect to the post-earthquake observations and physical modeling. It is stressed that the liquefied soil exhibits a dual behavior during the course of the shaking. Therefore, this research uses the concept of the fluid analogy with a Bingham model to represent the behavior of the liquefied soil.

In chapter 3, the basic concepts and fundamentals of the smoothed particles hydrodynamics are overviewed. The governing equations for liquefaction induced lateral spreading analysis are formulated in the framework of fluid dynamics. An existing educational SPH code is extended to model hydrodynamics problems using material strength. Its ability and efficiency to simulate Newtonian and Non-Newtonian flow is validated using three benchmark problems of a Poiseuille flow, a dam break of a water column as well as a water-column mixture for which experimental results exist.

In chapter 4, the SPH method is extended to simulate lateral spreading and to assess the induced ground displacement using results of model test conducted on 1g shaking table. A simple phenomenological bilinear model for the recovery of the soil

rigidity is proposed. It expresses the relationship between the yield viscosity and the induced shear strain. Numerical simulations are then conduced to assess the ground displacement induced during lateral spread, to validate the similitude law of the liquefied soil and to investigate the flow of a liquefied soil around a model pile.

Finally chapter 5 summarizes the findings of this research and suggests some aspects that deserve further investigations in order for the SPH to be applied to real problems.

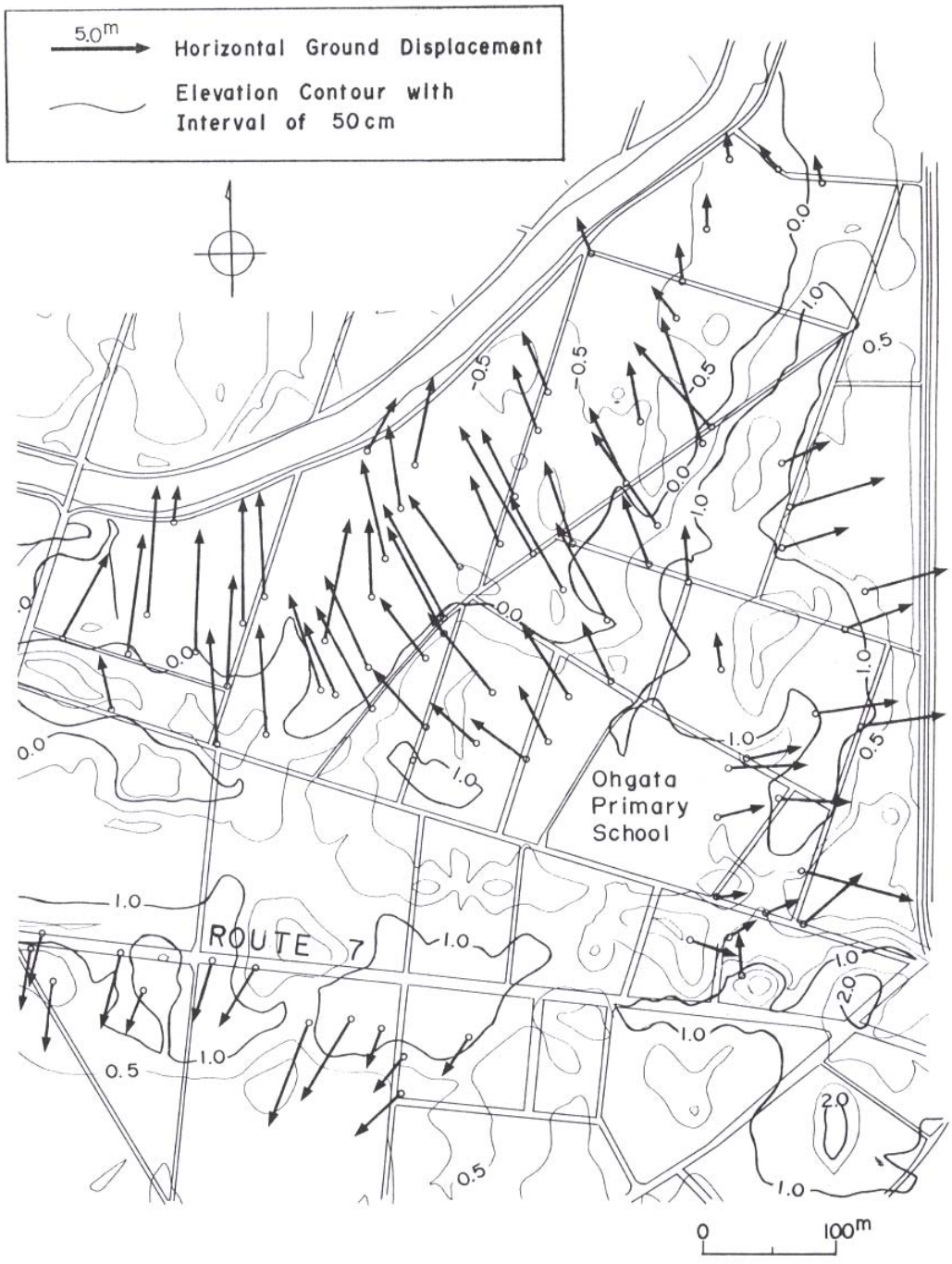

Fig. 1. 1: Permanent lateral displacement in Ohgata area in Niigata city.
Doi and Hamada (1992)

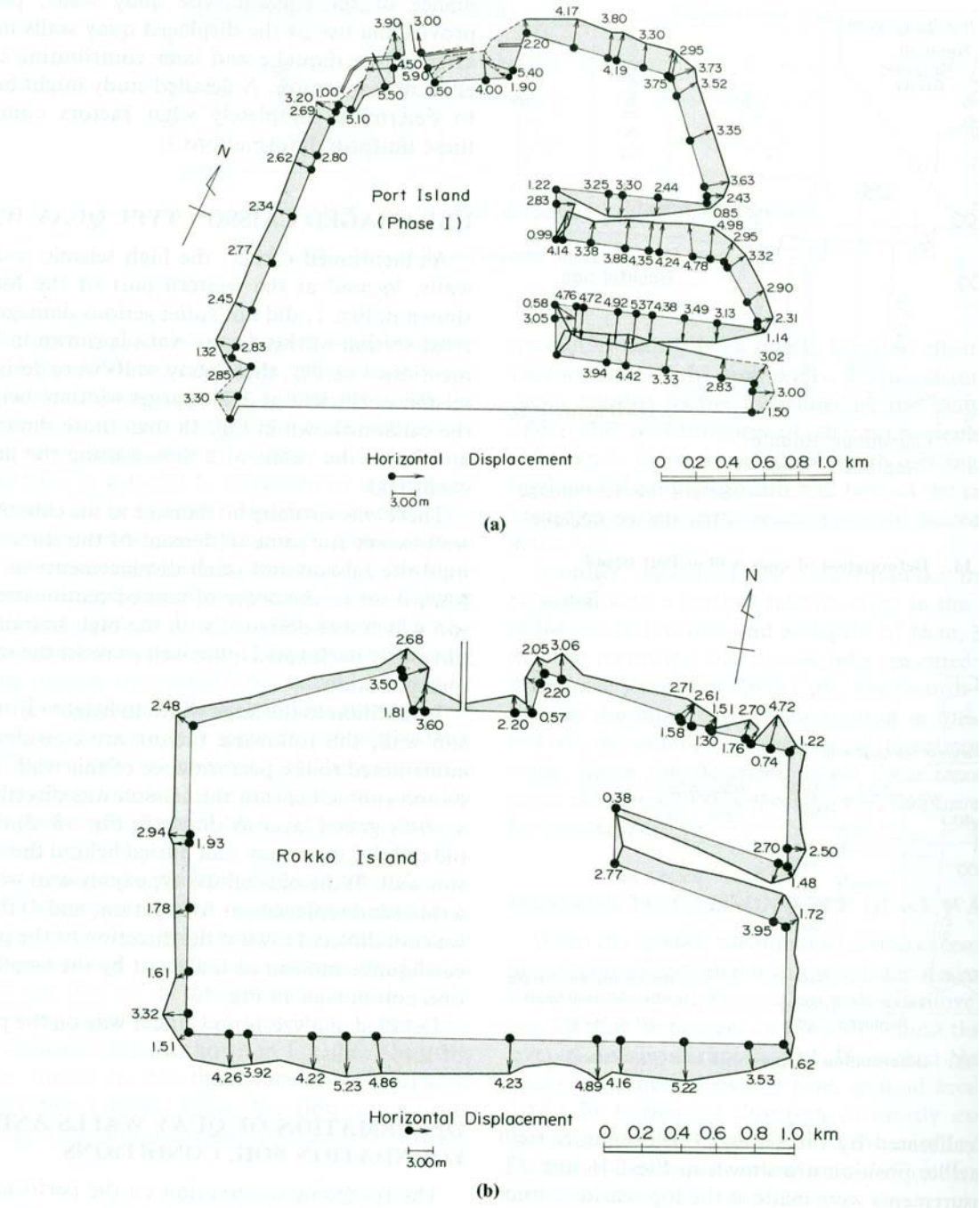

Fig. 1. 2: Permanent lateral displacement in Port Island and Rokko Island
Inagaki et al. (1996)

Chapter 2

Mechanical properties of liquefied soil and its constitutive model based on fluid dynamics

2.1 Introduction

During the last decades, the behavior of liquefied soil has been the subject of a controversy debate to whether liquefied soil behaves like a solid or a fluid or with combined characteristics (solid and fluid) during the earthquake. This debate arises as a result of some evidences from post-earthquake observations. In fact, if we look at the sinking of buildings and buried sewage tank or at the floatation of pipelines during liquefaction, a plausible explanation to this phenomenon could be related to the fluid-like behavior of the liquefied soil. If this assumption is true, the ground surface should have been flat after the occurrence of the ground movement. However, most of the documented case studies have revealed that the surface of the actual ground still preserve a certain inclination. This could suggest that the soil may have behaved as a solid with reduced shear stiffness. According to this assumption, the magnitude of the displacement should be proportional to the gradient of the ground surface because the gravity governs the deformation of the solid ground. Unfortunately, low correlation between the ground displacement and the surface gradient were found in the case studies. Accordingly, the idea of the behavior of the liquefied soil with combined characteristics of fluid and soil is the most plausible.

This chapter outlines the experimental techniques used to investigate the mechanical properties of liquefied soil. In this respect, the following aspects are overviewed:

1. The mechanical behavior of liquefied sand.
2. Experimental investigation on the viscosity coefficient of the liquefied soil.
3. The constitutive model for the liquefied soil in the framework of fluid dynamics.

2.2 Mechanical behavior of liquefied sand

Undrained triaxial compression tests, cyclic torsional shear tests and shaking table experiments have revealed that the liquefied soil behaves either as a solid or as viscous fluid or with combined characteristics during the course of the shaking.

- **Solid like behavior**

Ishihara (1993) presented some undrained triaxial compression tests of loose saturated Toyoura sand undergoing large strain under different confining pressures. He showed that the sand exhibits a strain hardening behavior, and the deviatoric stress and the effective confining stress reach a constant value when the steady state is achieved. The stress mobilized at this state has been termed the steady-state strength or the undrained residual strength (Castro), and the state of the minimum shear strength is called the state of phase transformation.

In another experiment, Yasuda et al. (1995) studied the post liquefaction behavior of loose Toyoura sand by conducting cyclic torsional shear tests followed by monotonic loading under several testing conditions. During the tests, the effect of the relative density, the confining pressure, the excess pore pressure ratio and the severity of the liquefaction were investigated. The tests results showed that the post liquefaction behavior of sand was strain hardening and the stiffness of liquefied soil recovered in a large strain region. The presence of the residual strength in the first set of experiments and the recovery of the soil stiffness in the second set suggest that the liquefied soil behave as a solid.

- **Fluid like behavior**

Sasaki et al. (1992) reviewed field observations of the ground displacements at Noshiro city after the Nihonkai Chubu earthquake in 1983 as well as at other sites in other regions. They revealed the following nature of the permanents displacements:

- The permanent displacement is oriented down toward the foot of a slope, suggesting an influence of the gravity.
- The displacements at the top of the slope are greater than those at its foot.
- As for the vertical displacement, subsidence is predominant near the top, while heaving occurs at the bottom.

To investigate the mechanism of the permanent displacement, Sasaki et al. conducted a series of shaking table tests on model ground of level surface or with embankment. Both models were subjected to a continuous shaking in the longitudinal direction to reach the maximum possible displacement. Ultimately, the ground surface became level when it reached the final equilibrium irrespective of the relative density of the ground model. The authors made the following observation:

- The liquefied ground behaves similar to liquid. Hence, its movement is affected by the total head gradient defined in terms of the total overburden stress and the elevation heads.
- The magnitude of the lateral displacement in a liquefied sandy layer is null at the base and increases towards the surface.
- The permanent displacement is caused by the gravity force. The cyclic acceleration influences the movement only indirectly.

Hamada et al. (1992) conducted shaking table experiments to clarify the effect of the liquefaction induced ground displacement on in-ground structures. Experiments to measure the pressure of liquefied soil on rigid in-ground wall and the effect of liquefaction induced ground displacement on a pile were performed. The findings showed that the pressure exerted by liquefied soil on a rigid in-ground wall was approximately equal to the pressure of a liquid with an equivalent specific gravity, and the force due to lateral flowing ground is affected by the flow velocity rather than the magnitude of the ground displacement.

Based on case studies and shaking table experiments, Hamada and Wakamatsu (1998) pointed out that the behavior of liquefied soil during earthquake shaking is similar to a viscous fluid. However, this behavior has a limited time interval and the soil regains its rigidity after the dissipation of excess pore water pressure.

In an attempt to investigate the behavior of liquefied sand undergoing large deformation during and after the shaking, Towhata et al. (1999) conducted a special shaking table experiment by monitoring the drag force needed to pull laterally a model pipe embedded in a loose deposit of Toyoura sand. The idea behind this experiment is that the relationship between the drag force and the displacement of the pipe may give an idea of the stress-strain behavior of sand undergoing large deformation. Tests results showed that the drag force vs. displacement diagram is equivalent to a stress-strain diagram of sand undergoing high excess pore water pressure and shaking. Moreover, the force vs. displacement relationship after the shaking is similar to the stress-strain curves of sand undergoing cyclic mobility. During the experiment, the relationship between the drag force and the velocity of the pipe at 100% excess pore water pressure was also derived. Fig. 2.1 shows the proportional relationship between the drag force and the velocity of the pipe for different value of void ratio. This may suggest that the liquefied sand behaves similar to a viscous liquid and that the viscosity increases with the density of the sand.

Results from previous experiments highlighted the nature of the dual behavior of liquefied sand. While the idea of a fluid-concept behavior of the sand is the result of shaking table experiments with 100% pore water pressure rise, the theory of the steady state strength of sand developed by running undrained monotonic shear tests (for which effective stress exists) resulted in the solid- concept of the liquefied soil.

On the light of the previous experimental results, we can assert that the liquefied soil behaves similar to a viscous fluid during the course of the shaking even for a limited time; but after the dissipation of the pore water pressure, the soil recovers its rigidity and returns to behave as a solid.

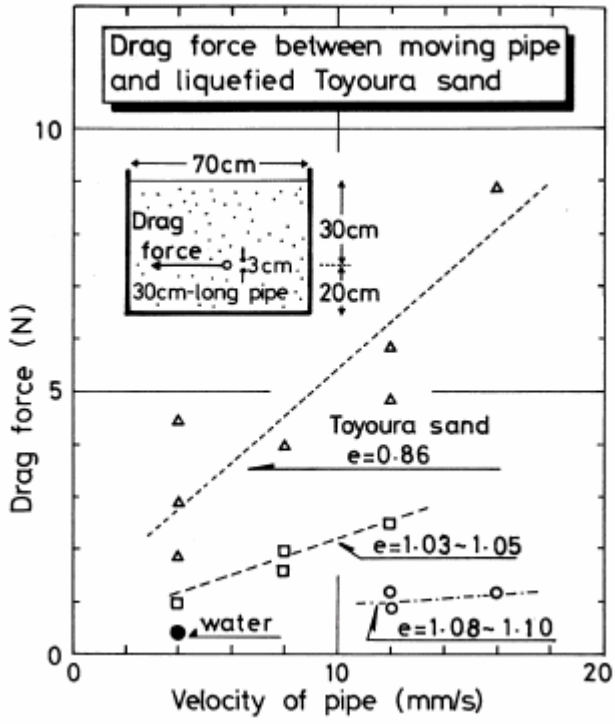

Fig. 2. 1: Relationship between the drag force and the velocity of the pipe (After Towhata et al, 1999)

2.3 Experimental investigations on the viscosity of liquefied sand

Several experimental techniques have been employed to assess the viscosity coefficient (or apparent viscosity) of liquefied sand assuming the viscous fluid analogy.

In this respect, the viscosity coefficient has been investigated using shaking table experiments by Towhata et al. (1999) and Hamada and Wakamatsu (1998), pull-up and dropping ball method by Miyajima et al. (1995), viscometer by Kawakami et al. (1994) and laboratory shear test by Nishimura et al. (2002). This section outlines each of these techniques and discusses the discrepancy between the values of the apparent viscosity obtained by different methods.

1. Shaking table test

- Towhata et al. (1999)

By pulling laterally a pipe embedded in loose Toyoura sand during shaking table experiment, Towhata et al. (1999) were able to monitor the drag force exerted on the pipe. On the basis of the relationship between the drag force and the velocity of the pipe presented in Fig.2.1, an attempt was made to back calculate the apparent viscosity of the liquefied subsoil. The drag force exerted on a cylinder by a flow of viscous fluid has been expressed by Lamb as follows:

$$F_D = \frac{4\pi\mu VL}{2.022 - \ln \mathrm{Re}} \tag{2.1}$$

Where:

Re is the Reynolds number ($\mathrm{Re} = \rho VD / \mu$). D and L are the diameter and the length of the cylinder and V is the pulling velocity respectively.

By substituting the experimental data in Eq.2.1, the apparent viscosity of liquefied sand was assessed. Towhata et al concluded that the looser sand has the smaller apparent viscosity. Moreover, the drag force measured during the shaking gave the smaller apparent viscosity.

- Hamada and Wakamatsu (1998)

Hamada and Wakamatsu (1998) conducted shaking table test to investigate the viscosity coefficient of liquefied soil. A model ground of 3 m wide and 1 m thick was prepared inside a soil container. Liquefaction was induced by vibrating the soil box using a sinusoidal wave with a maximum acceleration of $400\,cm/s^2$. After the occurrence of liquefaction, the lateral spread was caused by inclining the soil container and applying a sinusoidal wave with a maximum acceleration of $100\,cm/s^2$. By representing the flow velocity of the liquefied soil as ¼ of sinusoidal wave, the authors derived the following analytical expression for the maximum velocity at the ground surface.

$$V_S = 16\frac{H^2}{\pi^3}\frac{\rho_g}{\mu}\theta\left[1-\exp\left\{\left(\frac{\pi}{2H}\right)^2\frac{\mu}{\rho}t\right\}\right] \qquad (2.2)$$

Where: V_s is the velocity at ground surface, H is the thickness of the liquefied soil, ρ is the density, μ is the viscosity coefficient and θ the inclination angle of the ground soil, g is the gravity acceleration and t is the time.

By replacing the measured flow velocities during the experiments in Eq (2.2), the viscosity coefficient μ was estimated.

2. Pulling up and dropping ball method

Miyajima et al. (1995) performed two types of experiment using steel ball to measure the viscosity coefficient of liquefied soil. In the first experiment, an immerged steel ball placed inside a model ground was pulled laterally using a motor. The liquefaction was induced by flowing water from the bottom of the soil container and controlling the excess pore water pressure. During the experiment, the relationship between the drag force and the speed of the ball was obtained by measuring the drag force necessary to pull the ball for three levels of pulling velocities. By assuming the liquefied ground to be a perfect Newtonian fluid, Miyajima et al. used the stockes's law to express the drag force acting on the ball and were able to estimate the viscosity coefficient of the liquefied ground. In the second experiment, the authors measured the viscosity coefficient of a completely liquefied soil by monitoring the dropping movement of a steel ball inside a soil container subjected to different shaking intensity. During the tests, 4 balls with different diameters were used. Tests results showed that balls with diameter less than 6.0 cm exhibit the same viscosity coefficient irrespective of the input acceleration, while viscosity coefficient obtained using ball with diameter bigger than 6 cm seem to decrease with an increase of the input acceleration. According to the authors, this phenomenon is attributed to the ball's weight that might have caused densification of surrounding soil. The viscosity coefficient obtained by disregarding the soil densification is 10^5 times larger than the water's viscosity.

3. Assessment of viscosity using viscometer

Kawakami et al. (1994) used a viscometer to measure the viscosity of a liquefied soil inside a cylindrical soil container having 8.5 cm in diameter and 30 cm in depth. The liquefaction was induced by flowing water from the bottom of the container connected to a water tank. Experiment was performed on soil specimen having three different relative densities *Dr* using six different number of rotation of the viscometer. The viscosity coefficient is expressed by the following equation:

$$\eta = K \frac{M(R^2 - r^2)}{4\pi H R^2 r^2 \Omega} \tag{2.3}$$

Where, *R* and *r* are the radius of the soil container and the rotor respectively. *M* is the torque moment and Ω denotes the angular velocity. *K* is a correction factor.

Results from viscometer experiment showed that there is a correlation between the viscosity coefficient, the relative density and the number of rotation. In fact, the viscosity increases as the relative density increases and the larger is the number of rotation, the smaller is the viscosity coefficient.

In conclusion, viscosity coefficient (or apparent viscosity) of liquefied sand has been investigated using several experimental setup

4. Laboratory shear test on viscous nature of liquefied sand

Nishimura et al. (2002) attempted to measure the rate dependent behavior of sand at low confining effective stress levels. The main idea consisted in monitoring the delayed strain response of the specimen after reducing the isotropic consolidation stress and applying a quick axial load. The tests have revealed that the shear stress consisted of a frictional component and a rate-dependant component that enabled the assessment of the viscous coefficient of the liquefied sand. Tests results showed that the measured viscosity depends on the magnitude of both shear strain and shear strain rate. In the case of Toyoura sand, the value of the viscosity coefficient lies in the range of 600 ~ 4000 kPa·s.

2.4 A constitutive model for liquefied sand based on fluid dynamic

Previous experimental results by Hamada and Wakamatsu (1998) and Nishimura et al. (2002) highlighted the rate-dependent nature of liquefied sand. Wakamatsu and Hamada (1998) represented on a logarithmic scale, the relationship between the shear strain rate and the viscosity coefficient measured by different experiments using shaking table test of a lateral spread, steel ball pull-up test and viscometer.

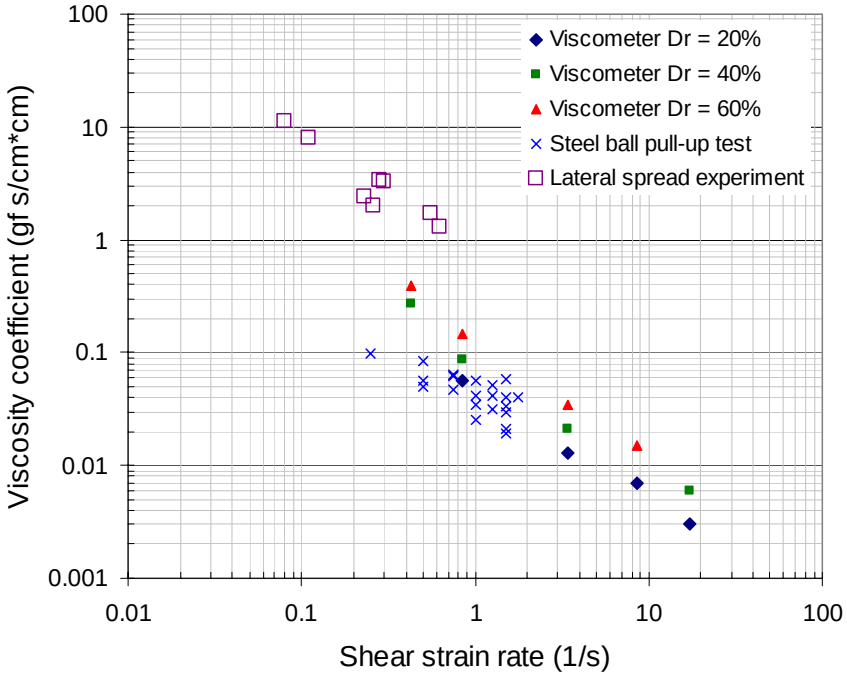

Fig. 2. 2: Relationship between the shear strain rate and viscosity coefficient (After Hamada and Wakamatsu, 1998)

As shown in Fig.2.2, the viscosity coefficient of the liquefied soil decreases with increasing shear strain rate and thus denoting its non-linear nature. Based on these findings, Hamada and Wakamatsu proposed a constitutive model assuming the liquefied soil to behave as Non-Newtonian fluid in the form of a pseudo-plastic fluid. They proposed the following relation between the shear stress and the shear strain rate:

$$\tau = \eta_0 \dot{\gamma} \Big/ (1 + \dot{\gamma} / \dot{\gamma}_r) \qquad (2.4)$$

In this equation, η_0 represents the initial viscosity coefficient, while $\dot{\gamma}_r$ is called the reference shear strain rate and represents the shear strain rate when the secant viscosity becomes $\eta_0/2$.

Using Kawakami's experimental results of the viscosity obtained with the viscometer, Uzuoka et al. (1998) derived the relationship between the shear stress and the shear strain rate as shown in figure 3.

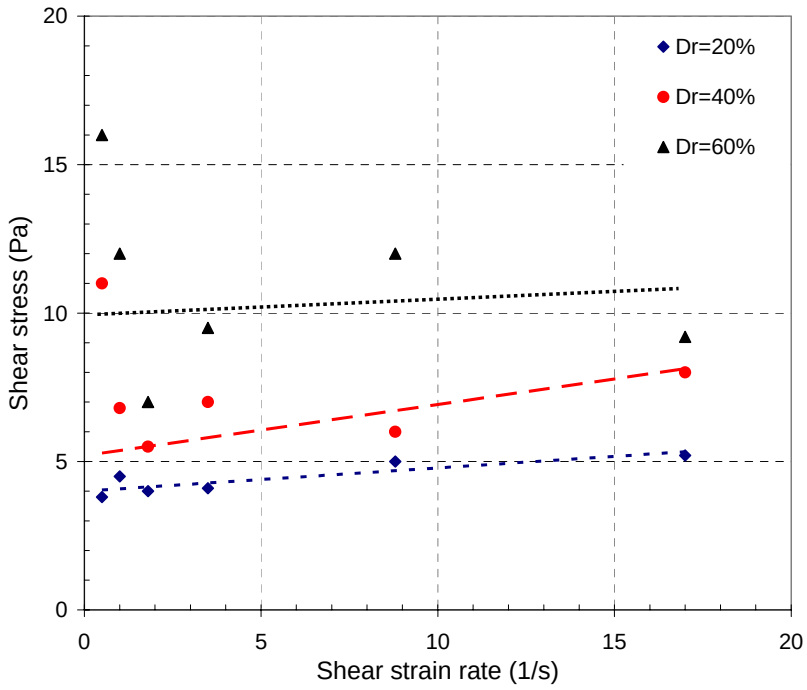

Fig. 2. 3: Shear strain rate - shear stress relation of liquefied soil obtained by viscometer

(after Uzuoka et al, 1998)

In Fig.2.3, the non linear property of the liquefied soil is seen from the relationship between the shear stress and the strain rate. According to Uzuoka et al. (1998), these relations have had intercepts on the shear stress axis that corresponded to the steady state strength. Moreover, the steady state strength increases with

increasing relative density. This result is consistent with laboratory tests on the steady shear strength. Based on this observation, Uzuoka et al. suggested that the behavior of liquefied soil can be represented by a Bingham type constitutive model which is one of the viscoplastic models with respect to the residual strength.

The authors proposed the following

$$\tau = \tau_y + \eta_y \dot{\gamma} \tag{2.5}$$

This model is very advantageous from a practical viewpoint since it is defined by two parameters; the yield viscosity η_y and the yield shear stress τ_y. The yield shear stress according to Uzuoka, corresponds to the minimum undrained shear strength.

In this study, we make use of this useful finding to adopt the Bingham constitutive model and extend its use within a Lagrangian meshfree particle approach to assess the deformation induced during lateral spreading. As shown in Fig.2.4, the Bingham model is able to represent the dual behavior of the liquefied soil with respect to the minimum undrained shear strength or the residual strength. According to this figure, the liquefied subsoil behaves as a solid when it is subjected to a driving stresses smaller than the residual strength, and starts to behave as a viscous fluid exhibiting a linear relationship with the shear strain rate when the driving stresses are larger than the residual strength.

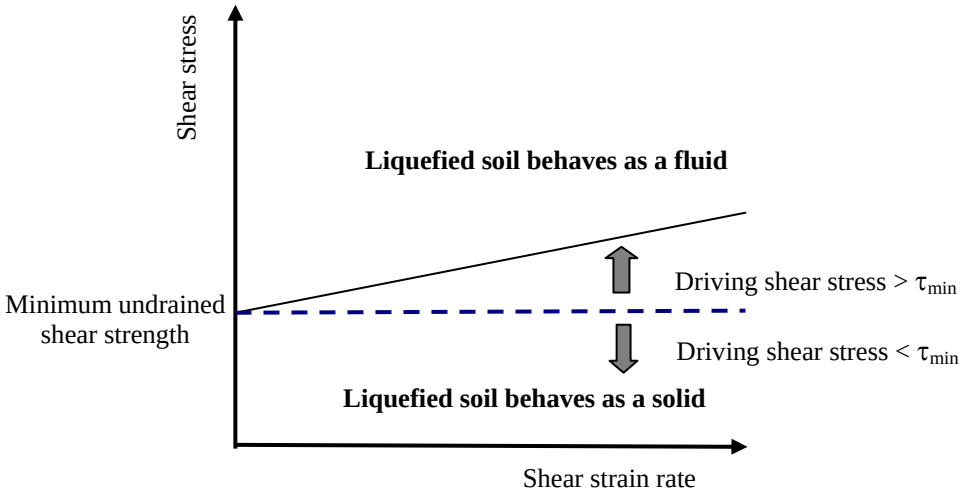

Fig. 2. 4: Behavior of liquefied soil by Bingham model (after Uzuoka et al, 1998)

2.5 Summary

This chapter introduced and discussed the nature characteristics of liquefied soil with respects to post-earthquakes observations and physical modeling. It was emphasized that the viscous liquid analogy is a useful concept in understanding the deformation of the liquefied soil deposit in lateral spread and the damage that occurred to many engineering facilities. However, this concept can not stand at the end of the shaking when the pore water pressure has totally dissipated and the subsoil has recovered part of its rigidity. It was concluded then, that the liquefied soil exhibits a dual behavior and a plausible explanation consists in assuming the liquefied soil as a viscous fluid during the course of the shaking, and as a solid with reduced rigidity after the dissipation of the pore water pressure.

Because the viscous fluid analogy is a useful concept, many researchers attempted to assess the apparent viscosity (or the viscosity coefficient) of the liquefied soil using various experimental testing. Shaking table experiment on model ground, laboratory shear test as well as viscometer, pile and steel ball pulling-up have been used to measure the viscosity of the liquefied soil. Tests results showed that the measured value lie in a range between 10 ~ 10000 Pa·s. Most importantly are the Hamada and Wakamatsu's test results that highlighted the non linear nature of the liquefied soil, by showing that the viscosity coefficient decreases with increasing shear strain rate. Using viscosity results obtained by viscometer, Uzuoka et al. derived a non linear relationship between the shear strain rate and the shear stress and proposed a Bingham type constitutive model for liquefied soil.

In this study, we adopt the viscous fluid analogy and the Bingham model representation of the behavior of the liquefied subsoil, as general concept to assess the liquefaction induced large displacement in the framework of fluid dynamics using Lagrangian meshfree particle method.

Chapter 3

Smoothed particle hydrodynamics for liquefaction induced lateral spreading analysis

3.1 Introduction

Several methods to predict the magnitude of the induced displacement due to lateral spreading have been overviewed in chapter 1. These methods range from pure numerical methods using FEM, volume of fluid method (VOF), cubic interpolated pseudoparticle (CIP) to empirical approaches and simplified analytical techniques involving the Newmark's sliding block and the minimum potential energy. Although, these methods were able to assess with an acceptable accuracy the induced displacement, tedious and time consuming numerical techniques were supplemented to overcome mesh distortion and to allow tracking moving boundary and interfaces.

Accordingly, this study proposes a numerical technique based on SPH in the framework of fluid dynamics to assess the large displacement and track the free surface shape without additional numerical treatment.

This chapter introduces the basic concepts of the smoothed particle hydrodynamics (SPH), as well as its formulation and implementation to assess large displacements induced by lateral spreading. Discussion on the appropriate kernel function, optimal smoothing length, adequate sound speed and treatment of numerical diffusion will be presented. To validate this approach, benchmark problems of a Newtonian Poiseuille flow for which a time series solution exists will be compared to those obtained by SPH technique. Moreover the results of a dam breaking flow of a water column problem will be compared with experimental ones.

3.2 Concepts and formulation of SPH

3.2.1 SPH concepts

The SPH is a meshfree, Langragian particle method used for modeling hydrodynamics problems. It was simultaneously invented by Lucy (1977) and Gingold and Monaghan (1977) to solve astrophysical problems. Since then, the method has been extended to solve various physical problems including free surface flow (Monaghan, 1994), multi-phase flow (Monaghan et al., 1995), simulation of brittle solids (Benz et al., 1995), flow through porous media (Zhu et al., 1999), etc.

Unlike the finite element method or the discrete element method, the physical domain in SPH is discretized by a set of equi-spaced unconnected particles that follow its motion and advect its contact discontinuities. The particles carry the domain's quantities such as the mass, the velocity vector, the position vector, etc. and thus forming not only the geometrical domain but also the computational domain for the partial differential equations representing the conservation laws (Randles and Libersky, 1996).

The idea behind the SPH is the estimation of the physical properties of the domain by interpolating from a set of disordered particles by means of a kernel function, which represents a weighted sum over neighboring particles within an area defined by the smoothing length. In other words, the contribution of each particle to the physical property is weighted according to their distance from the particle of interest by means of the kernel function which transform a point mass to a spatially spread one. Fig. 3.1 illustrates the concept of the weighted sum and the smoothing over neighboring particles.

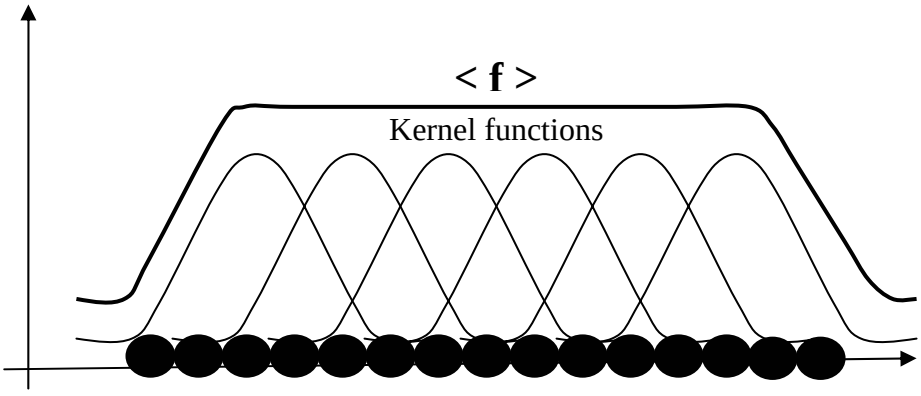

Fig. 3. 1: Smoothing averaging concept in SPH

3.2.2 SPH formulation

Basically, the SPH formulation is achieved by the following two steps: the kernel approximation and the particle approximation. The kernel approximation allows any function, provided it is defined and continuous, to be represented by an integral form:

$$f(\mathbf{x}) = \int_{\Omega} f(\mathbf{x}')\delta(\mathbf{x}-\mathbf{x}')d\mathbf{x}' \tag{3.1}$$

f is a function of *3D* position vector **x** and δ(**x-x**') is the Dirac Delta function. If the Dirac function is replaced by a smoothing kernel function *W* (**x-x**'), the integral representation of *f*(**x**) is given by:

$$< f(\mathbf{x}) >= \int_{\Omega} f(\mathbf{x}')W(\mathbf{x}-\mathbf{x}',h)d\mathbf{x}' \tag{3.2}$$

In Eq. (3.2), *h* represents the smoothing length or the inter-particle distance. The kernel function *W* (**x-x**') should satisfy the following conditions:

- The normalization condition expressed by Eq. (3.3).

$$\int_{\Omega} W(\mathbf{x}-\mathbf{x}',h) = 1 \tag{3.3}$$

- The Delta function property which states that when the smoothing length $h \to 0$, the kernel function should satisfy the Dirac function property.

$$\lim_{h\to 0} W(\mathbf{x}-\mathbf{x}',h) = \delta(\mathbf{x}-\mathbf{x}') \tag{3.4}$$

- The compact support Eq. (3.5).

$$W(\mathbf{x}-\mathbf{x}',h) = 0 \quad \text{when } |\mathbf{x}-\mathbf{x}'| > \lambda h \tag{3.5}$$

In Eq. (3.5), λ is a constant defining the effective area of the smoothing length.

Once the kernel approximation has been defined, the particle approximation can be achieved in the following way:

$$f(\mathbf{x}_i) = \int_{\Omega} f(\mathbf{x}')W(\mathbf{x}_i - \mathbf{x}', h)d\mathbf{x}' \approx \sum_{j=1}^{N} \frac{m_j}{\rho_j} f(\mathbf{x}_j)W(\mathbf{x}_i - \mathbf{x}_j, h) \tag{3.6}$$

Where, $\mathbf{x}_i$ is the position of the particle i at which the function is evaluated; m_j and ρ_j are respectively the mass and the density of the neighboring particles j (j=1, 2, ….., N) within the support domain. Eq. (3.6) states that the value of a function at particle i is approximated using the average of those values of the function at all the surrounding particles within the support domain of particle i weighted by the kernel function. Fig. 3.2 depicts the principle of the support domain and sphere of influence.

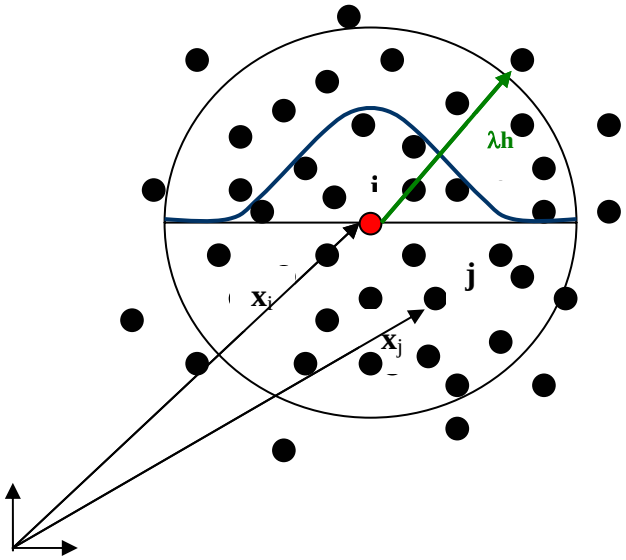

Fig. 3. 2: Support domain and particle approximation for particle i.

If the function $f(\mathbf{x})$ is replaced by ρ in Eq. (3.6), the SPH approximation for the density is obtained as:

$$\rho_i = \sum_{j=1}^{N} m_j W(\mathbf{x}_i - \mathbf{x}_j, h) \tag{3.7}$$

In the same manner, the spatial derivative of the function is given by Eq. (3.8):

$$\nabla \cdot f(\mathbf{x}_i) = \sum_{j=1}^{N} \frac{m_j}{\rho_j} f(\mathbf{x}_j) \cdot \nabla_i W(\mathbf{x}_i - \mathbf{x}_j, h) \tag{3.8}$$

Where:

$$\nabla \cdot W(\mathbf{x}_i - \mathbf{x}_j, h) = \frac{\mathbf{x}_i - \mathbf{x}_j}{r_{ij}} \frac{\partial W_{ij}}{\partial r_{ij}} \tag{3.9}$$

Where, r_{ij} represents the distance between particle i and j.

The smoothing function in SPH represents an important step in achieving the kernel approximation and the particle approximation. In this respect, different smoothing functions based on a Gaussian or spline kernel have been derived.

In order to assure a physical interpretation of the SPH formulation, Monaghan (1994) stated that the best choice for the kernel function is a Gaussian function which is sufficiently smooth even for high order derivatives. He expressed the smoothing function as:

$$W(R,h) = \alpha_D e^{-R^2} \tag{3.10}$$

Where:

$R = \frac{r}{h} = \frac{|\mathbf{x} - \mathbf{x}'|}{h}$ and $\alpha_D = 1/\sqrt{\pi}h$, $1/\pi h^2$ and $1/\sqrt[3]{\pi}h^3$ in one, two and three-dimensional space respectively.

Fig. 3.3 illustrates the Gaussian kernel and its 1st derivative.

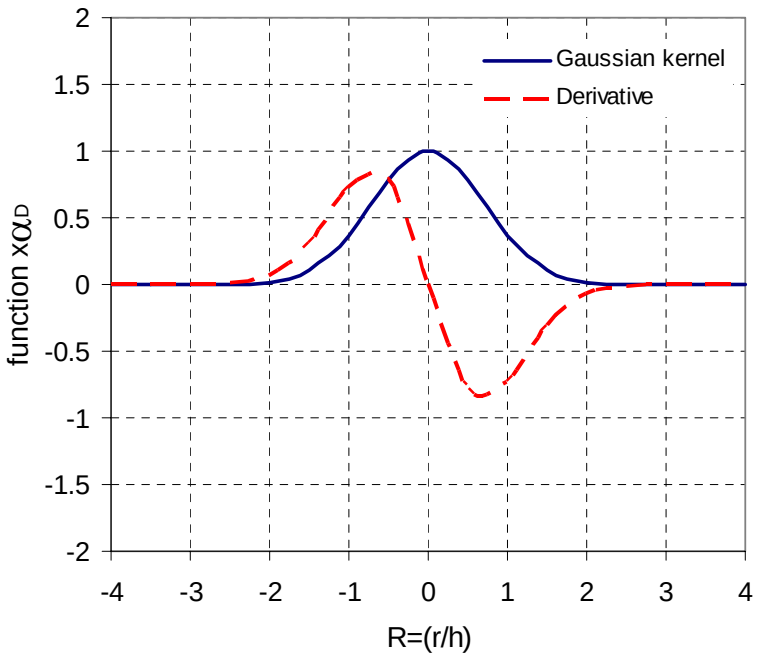

Fig. 3. 3: Kernel Gaussian and its 1st derivative

Although the Gaussian kernel is simple and interpolates with high accuracy, it has the practical disadvantage to be infinite in extent. Hence all the particles in a system contribute to the summation in Eq. (3.7), even the ones that are at such a distance that their contribution is effectively zero and this leads to an increased computational effort. To overcome this problem, many authors derived piecewise splines kernel which are more spatially compact and finite in extent. In this work, we use the quintic spline kernel function proposed by Morris (1997) and expressed by Eq. (3.11).

$$W(R,h)=\alpha_D\begin{cases}(3-R)^5-6(2-R)^5+15(1-R)^5 & \text{if } 0\le R<1\\ (3-R)^5-6(2-R)^5 & \text{if } 1\le R<2\\ (3-R)^5 & \text{if } 2\le R<3\\ 0 & \text{if } R\ge 3\end{cases} \tag{3.11}$$

Where R is equal to r/h, r is the distance between the particles, and α_D is a normalization constant having the values of $1/120h$, $7/478\pi h^2$ and $3/359\pi h^3$ in one, two and three-dimensional space, respectively

The kernel function and its 1st derivative are illustrated in Fig. 3.4.

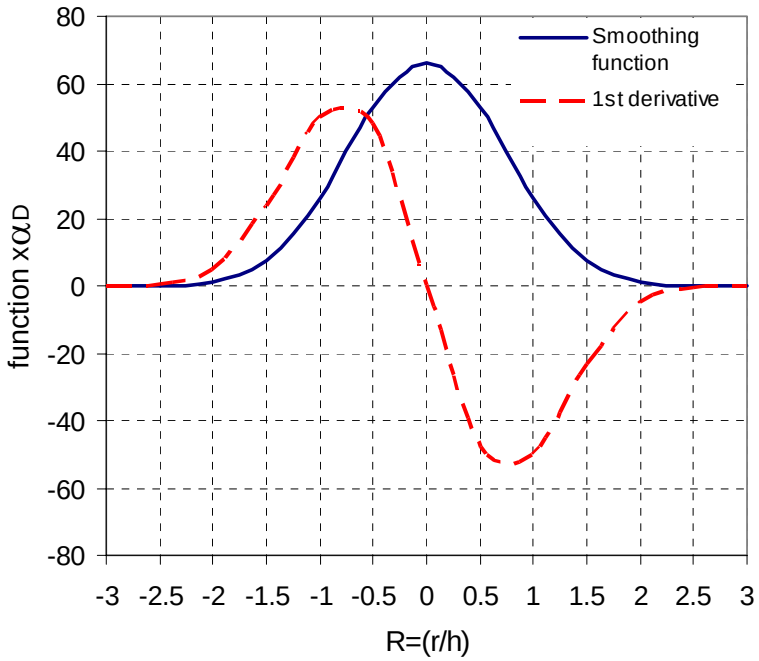

Fig. 3. 4: Quintic spline function and its 1st derivative

The physical properties of the quintic spline function are weighted over a region whose radius equals three times the smoothing length. This provides the advantage not only for a compact support but also for smoothness.

3.3 SPH formulation for liquefaction induced lateral spreading

In Chapter 2, the nature of liquefied soil has been discussed on the basis of post-earthquake observations and experiments. It was clarified that the liquefied soil possesses a dual behavior, i.e. a viscous fluid behavior during the course of the shaking and a solid one after the dissipation of the pore water pressure. On the basis of this concept, we consider a Bingham type constitutive model for the liquefied soil, which is one of the visco-plastic models taking account of the minimum undrained shear strength.

This section introduces the main modification we have implemented so that SPH may simulate non-Newtonian fluid and thus assess ground displacement induced by lateral spreading due to liquefaction. In this respect, this section discusses the following aspects:

- Expression of the governing equations using SPH formalism.
- Implementation of the effective equivalent viscosity to model non-Newtonian fluid.
- Treatment of boundary.

3.3.1 Governing equations

In this study, the liquefied soil is regarded as an incompressible fluid whose behavior is governed by the mass and the momentum conservation principles expressed by the following equations:

$$\frac{D\rho}{Dt} + \rho \frac{\partial v^{\beta}}{\partial x^{\beta}} = 0 \tag{3.12}$$

$$\frac{Dv^{\alpha}}{Dt} = \frac{1}{\rho} \frac{\partial \sigma^{\alpha\beta}}{\partial x^{\beta}} + \mathbf{g}^{\alpha} \tag{3.13}$$

In Eqs. (3.12) and (3.13), ρ represents the density and $\mathbf{g}$ the acceleration of gravity. $\sigma^{\alpha\beta}$ is the total stress tensor which can be written as the sum of an isotropic component p and a deviatoric component $\tau^{\alpha\beta}$.

$$\sigma^{\alpha\beta} = -p\delta^{\alpha\beta} + \tau^{\alpha\beta} \tag{3.14}$$

For a Newtonian incompressible fluid, the shear stress-shear strain rate relationship can be expressed by the following equation:

$$\tau^{\alpha\beta} = \mu \dot{e}^{\alpha\beta} \tag{3.15}$$

Where μ : Dynamic viscosity

$\dot{e}^{\alpha\beta}$: Deviatoric strain rate tensor.

$$\dot{e}^{\alpha\beta} = \frac{\partial \mathbf{v}^{\alpha}}{\partial \mathbf{x}^{\beta}} + \frac{\partial \mathbf{v}^{\beta}}{\partial \mathbf{x}^{\alpha}} - \frac{2}{3}(\nabla \cdot \mathbf{v})\delta^{\alpha\beta} \tag{3.16}$$

Where $\mathbf{v}$: Velocity vector

Substituting Eq. (3.14) into the momentum Eq. (3.13) leads to the equation of motion expressed in the form of:

$$\frac{D\mathbf{v}^{\alpha}}{Dt} = -\frac{1}{\rho}\frac{\partial p}{\partial \mathbf{x}^{\alpha}} + \nu \frac{\partial}{\partial \mathbf{x}^{\beta}}\left(\frac{\partial \mathbf{v}^{\alpha}}{\partial \mathbf{x}^{\beta}}\right) + \mathbf{g}^{\alpha} \tag{3.17}$$

Where: $\nu = \mu / \rho$ represents the kinetic viscosity.

Using the following two properties, the SPH formulation for the mass and momentum conservation are expressed by Eqs. (3.20) and (3.21).

$$\nabla \cdot f(\mathbf{x}_i) = \frac{1}{\rho_i}\left[\sum_{j=1}^{N} m_j \left[f(\mathbf{x}_j) - f(\mathbf{x}_i)\right] \cdot \nabla_i W_{ij}\right] \tag{3.18}$$

$$\nabla \cdot f(\mathbf{x}_i) = \rho_i \left[\sum_{j=1}^{N} m_j \left[\left(\frac{f(\mathbf{x}_i)}{\rho_i^2}\right) + \left(\frac{f(\mathbf{x}_j)}{\rho_j^2}\right)\right] \cdot \nabla_i W_{ij}\right] \tag{3.19}$$

$$\frac{D\rho_i}{Dt} = \sum_{j=1}^{N} m_j (\mathbf{v}_i^{\beta} - \mathbf{v}_j^{\beta}) \frac{\partial W_{ij}}{\partial \mathbf{x}_i^{\beta}} \tag{3.20}$$

$$\frac{D\mathbf{v}_i^{\alpha}}{Dt} = \sum_{j=1}^{N} m_j \left(\frac{\sigma_i^{\alpha\beta}}{\rho_i^2} + \frac{\sigma_j^{\alpha\beta}}{\rho_j^2}\right) \frac{\partial W_{ij}}{\partial \mathbf{x}_i^{\beta}} + \mathbf{g}^{\alpha} \tag{3.21}$$

Roman subscripts *ij* are used to denote the particles identification; while Greek indices $\alpha\beta$ are used to express the coordinate system. Therefore, in Eqs. (3.10) and (3.21), *Wij* represents the smoothing function of particle *i* evaluated at particle *j*.

Using Eq. (3.14) for the total stress, Eq. (3.21) can be written as:

$$\frac{D\mathbf{v}_i^{\alpha}}{Dt} = -\sum_{j=1}^{N} m_j \left(\frac{p_i}{\rho_i^2} + \frac{p_j}{\rho_j^2}\right) \frac{\partial W_{ij}}{\partial \mathbf{x}_i^{\alpha}} + \sum_{j=1}^{N} m_j \left(\frac{\mu_i \varepsilon_i^{\alpha\beta}}{\rho_i^2} + \frac{\mu_j \varepsilon_j^{\alpha\beta}}{\rho_j^2}\right) \frac{\partial W_{ij}}{\partial \mathbf{x}_i^{\beta}} + \mathbf{g}^{\alpha} \tag{3.22}$$

In Eq. (3.22), the first part of the right hand side represents the SPH approximation for the pressure term, while the second part represents the viscous forces. The pressure terms are computed using an appropriate equation of state which relates the hydrostatic pressure to local densities. Monaghan (1994) suggested the following equation of state while modeling free surface problem.

$$p = B\left(\left(\frac{\rho}{\rho_0}\right)^{\gamma} - 1\right) \tag{3.23}$$

Where γ is a constant and it is taken equal to 7 in this study. ρ_0 represents the initial density while B is a parameter that sets a limit for the maximum change of the density so that the liquefied soil may be considered nearly incompressible. Usually, B is taken equal to the initial pressure $P_{0.}$ To limit the density fluctuation to an acceptable value of 1%, the value of the sound speed should be carefully chosen so that the Mach number is equal to 0.1.

3.3.2 SPH formulation for Non-Newtonian fluid

The previous SPH formulation is valid for a Newtonian fluid only. To extend this method to treat non-Newtonian fluid which is the assumed behavior of the liquefied subsoil, we introduce an equivalent viscosity in the SPH approximation of the viscous forces in Eq. (3.22).

A Bingham type fluid has the following shear stress-shear strain rate relationship.

$$\tau = \tau_{\min} + \mu_B \dot{\gamma} \tag{3.24}$$

Where τ_{min} represents the minimum undrained shear strength and μ_B the yield viscosity.

If we define an equivalent viscosity in the form of Eq. (3.25), a non Newtonian fluid can be modeled as a Newtonian type fluid.

$$\mu_{eff} = \mu_B + \frac{\tau_{\min}}{\dot{\gamma}} \tag{3.25}$$

Where $\dot{\gamma}$ is given by the second invariant of the deviatoric strain rate tensor.

$$\dot{\gamma} = \sqrt{\frac{1}{2} \dot{e}^{\alpha\beta} \dot{e}^{\alpha\beta}} \tag{3.26}$$

The concept of the equivalent viscosity is illustrated in Fig. 3.5. As it is seen, the relationship between the shear stress and the shear strain rate is represented by a solid line for the Bingham model, while the dashed lines express the behavior of the liquefied soil when the Bingham model is replaced by an equivalent Newtonian model. In this particular case, the equivalent effective viscosity represents the slope of the Newtonian model. During the simulation, this equivalent viscosity is evaluated and adjusted stepwise depending on the induced shear strain rate. If the shear strain rate increases, the dashed line moves towards the region 2 giving rise to a smaller equivalent viscosity, whereas when the shear strain rate decreases, the dashed line moves towards the region 1 giving rise to a larger equivalent viscosity.

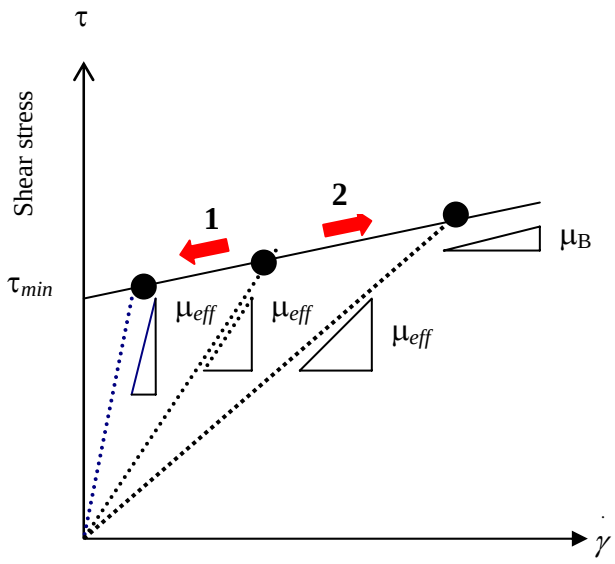

Fig. 3. 5: Concept of the equivalent effective viscosity

At this stage, the SPH formulation for the mass and the momentum conservation can be used to simulate the behavior of a Newtonian and a non-Newtonian fluid as well. However like most physical problems, numerical consideration on how to simulate the free surface conditions and wall boundary should be introduced.

In fact, near the free surface or the wall boundary, the SPH suffers from the edge effect due to the integral truncation that causes only the particles inside the boundary contribute to the summation of the particle interaction (see Fig. 3.6). In this case, the densities of the particles drop drastically and generate huge pressure term. To overcome this deficiency, the density of each particle should be estimated by means of the continuity approach using Eq. (3.20) instead of the summation equation Eq. (3.7). This let decrease the computation time and resolves the density deficiency near the boundary. Moreover as for the solid particles forming the boundary conditions near the wall, many techniques were developed using either ghost particles or virtual particles exerting repulsive forces to prevent the particles from penetrating through the boundary.

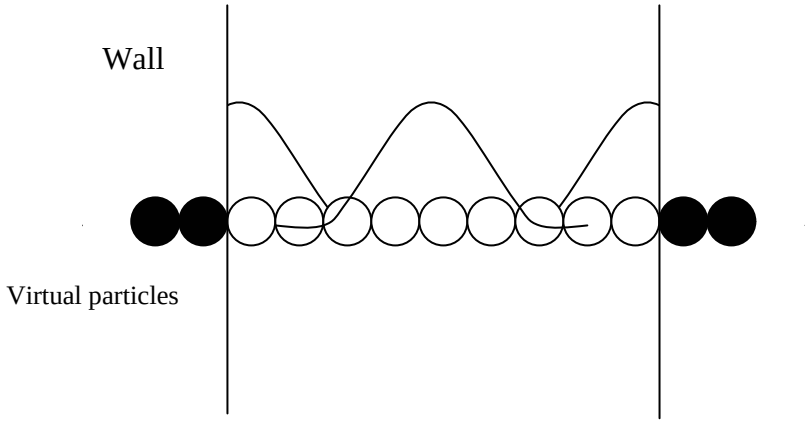

Fig. 3. 6: Integral deficiency near the boundary

In this study, the solid boundaries consist of virtual particles exerting a repulsive force expressed by Lennard-Jones potential given by Eq. (3.27).

$$f(r)=\begin{cases} D\left[\left(\frac{r_0}{r_{ij}}\right)^{n_1}-\left(\frac{r_0}{r_{ij}}\right)^{n_2}\right]\frac{\mathbf{x}_{ij}}{r_{ij}^2} & \text{if } \left(\frac{r_0}{r_{ij}}\right)\le 1 \\ 0 & \text{if } \left(\frac{r_0}{r_{ij}}\right)>1 \end{cases} \tag{3.27}$$

Where: D is a problem dependant parameter chosen in the same scale as the velocity. r_0 is the cutoff distance which represents the distance from which the repulsive forces are active. In this respect, if the cutoff distance is too large, the particles feel the repulsive forces from the initial distribution. However, if r_0 is too small, the particles may already have penetrated the wall before the repulsive forces start acting. Monaghan (1994) recommended choosing a cutoff distance equals to the initial distribution of the particles. The parameters n_1 and n_2 are taken equal to 12 and 6 respectively.

3.4 SPH code for liquefaction induced lateral ground displacements

In this section, the SPH code used to simulate the ground displacement during lateral spreading is introduced. The structure of the code, the particle interaction searching algorithm and the time integration scheme are discussed.

We used and enhanced an educational SPH code source written by (Liu and Liu, 2003) by implementing the following routines:

- Modeling of the hydrodynamics problems using material strength. The Bingham constitutive model proposed by Uzuoka et al. (1998) is implemented.
- Using a rather simple constitutive bilinear model for the recovery of the rigidity of the liquefied soil.
- Resolving the numerical instability induced by the small values of the shear strain rate at the beginning of the simulation. The Bingham model is rather described by a bilinear model in this case.
- Resolving the numerical instability using either an appropriate artificial viscosity or the XSPH technique proposed by Monaghan (1992) to stabilize the numerical scheme and prevent particles penetration.

3.4.1 Structure of the SPH code

So far, the details of the calculation process have been introduced. Fig. 3.7 summarizes the different steps involved during the simulation process. At the beginning, the initial configuration and the physical parameters are defined. An appropriate smoothing length is then chosen to define the support domain of each particle for which the list of the neighboring particles is established. Using the particle approximation technique, the density of each particle is evaluated using the continuity approach. The viscous force, the pressure force using the state equation and the external force due to gravity are evaluated for each time step. To stabilize the numerical scheme, the force due to the artificial viscosity is also computed and added to the previous terms (viscous, pressure, external). The velocity and the new position are evaluated by solving the equation of motion. After each time step, the density and the momentum are updated. The process is repeated until the overall simulation time is completed.

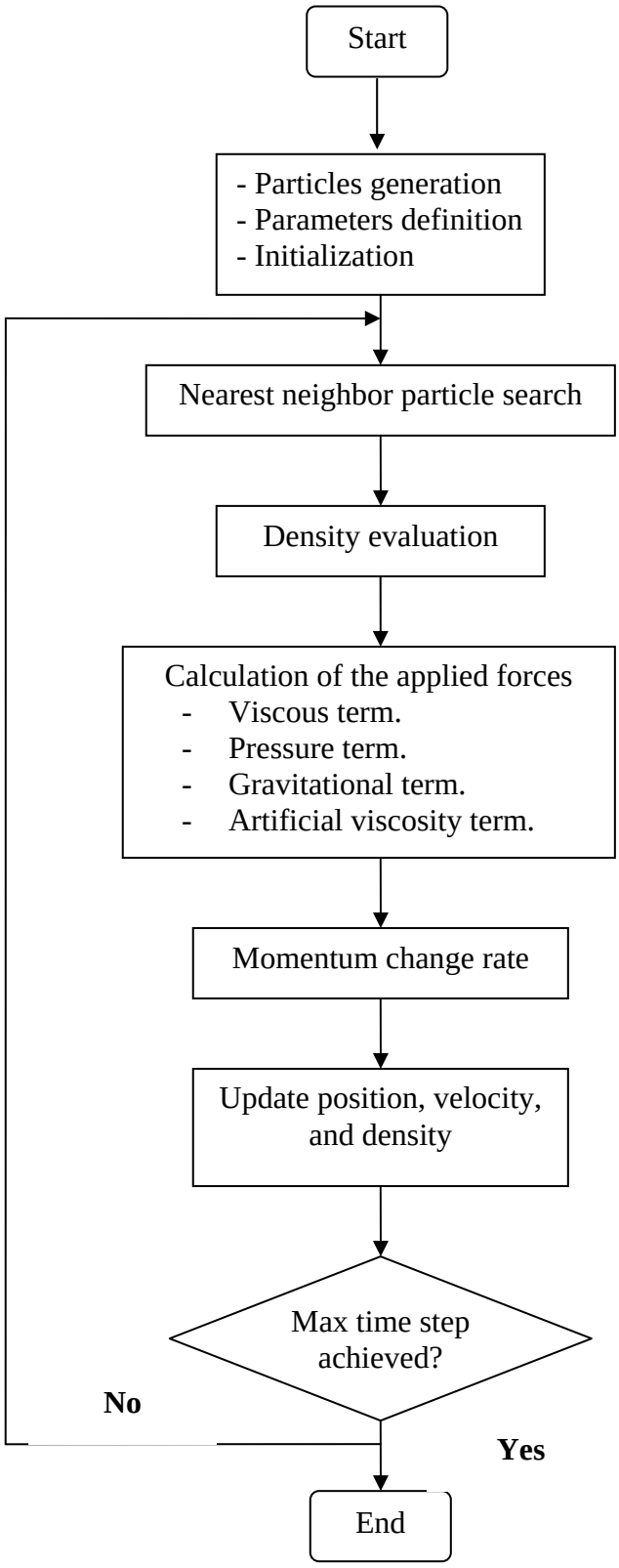

Fig. 3. 7: Flowchart of the SPH code

3.5 Numerical validation of the SPH code

To check the ability and efficiency of the SPH code to simulate a Newtonian and a non-Newtonian flow, two benchmark problems of a Poiseuille flow and a dam breaking of a water column for which experimental results exist are conducted. Moreover, a numerical simulation of a gravitational flow of a Newtonian viscous fluid and a non-Newtonian water-clay mixture governed by a Bingham type constitutive model is performed to reproduce the free surface shapes and the time history of the flow velocity and the induced displacement.

3.5.1 Poiseuille flow

A reliable benchmark problem to test the ability and accuracy of the SPH code is provided by a Poiseuille flow between parallel plates for which the exact solution exists, as well as a time series solution derived by Morris et al. (1997). A Poiseuille flow involves the flow between two parallel infinite plates driven from the stationary state by a body force. The flow starts moving till it reaches the steady state regime. The exact solution of the distribution of the velocity at the steady state is expressed by Eq. (3.28):

$$V_x(y) = \frac{F}{2\nu} y(L-y) \tag{3.28}$$

Where, ν represents the kinetic viscosity and L the channel's width.

Morris et al. proposed a time series solution for the Poiseuille flow having the following form:

$$V_x(y,t) = \frac{F}{2\nu} y(y-L) + \sum_{n=0}^{\infty} \frac{4FL^2}{\nu\pi^3(2n+1)^3} \sin\left(\frac{\pi y}{L}(2n+1)\right) \exp\left(-\frac{(2n+1)^2\pi^2\nu}{L^2} t\right) \tag{3.29}$$

In order to simulate the Poiseuille flow using SPH, the infinite plates should be correctly modeled. This can be accomplished either by taking the dimensions of the infinites plates large enough compared with the width of the channel or using periodic boundaries in the direction of the flow with a quite reasonable number of particles. In the first case, the involved number of particles should be large enough to reach the steady state. In this simulation, we rather implemented the periodic

boundaries in the direction of flow. The problem domain consists of a rectangle of 0.5 mm long and 1 mm wide. Total 800 particles spanning the channel in a regular Cartesian mesh were used; 40 particles along the distance between the plates and 20 along the channel length which give an initial spacing distance of $2.5x10^{-5}$ m. To model the solid walls, 20 virtual particles were used on each side of the plate. Fig. 3.8 illustrates the numerical setup.

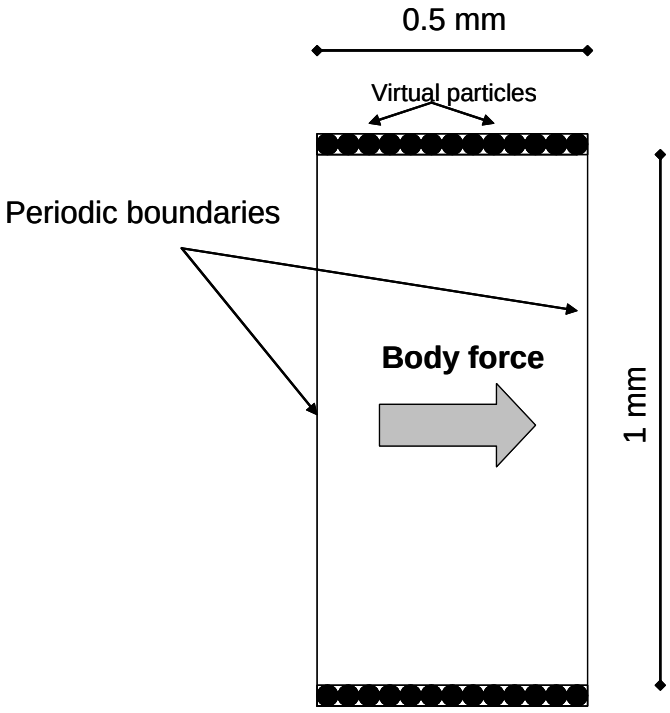

Fig. 3. 8: Numerical setup for Poiseuille flow simulation

During the simulation, a smoothing length 1.05 times the initial spacing was assigned to each particle. This gives a total of 24 neighbors within a circle of radius 3*h*. To limit the density fluctuation within 1%, Eq. (3.28) is used to assess the maximum flow velocity at the steady state which is equals to $2.5x10^{-5}$ m/s. Accordingly a sound speed equals to 1/10 of the maximum velocity was adopted to get a Mach number of 0.1.

Table 3.1 bellow summarizes the physical parameters used during the simulation.

Table 3. 1: Numerical parameters for Poiseuille flow simulation

Dimensions of the channel	0.0005x0.001m
Number of particles	20x40
Density of particles	$1000kg/m^3$
Viscosity	10^{-6} m^2/s
Body force **F**	$2x10^{-4}m/s^2$
Time increment	$10^{-4}s$
Sound speed	$2.5x10^{-4}$ m/s

The simulation was executed during 1s giving 10000 total time steps. After 5000 steps, the steady state was reached and the flow attains its maximum velocity. Fig. 3.9 depicts the SPH results with the time series solution given by Eq. (3.29). The SPH results are smaller than the time series solutions with a relative error less than 0.6% which can be assumed as a good approximation.

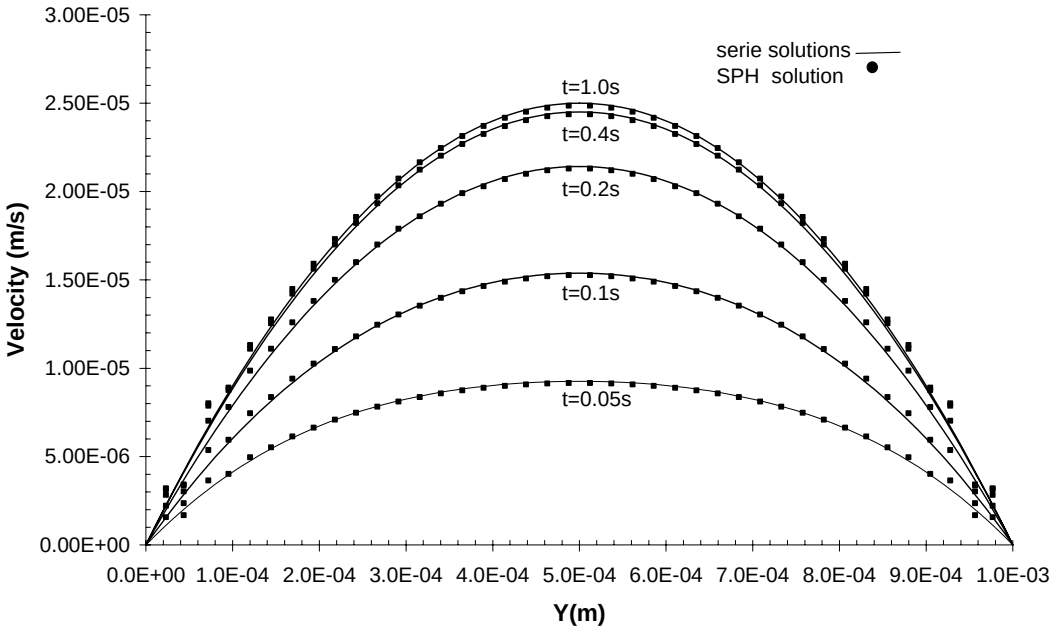

Fig. 3. 9: Time series solution .vs. SPH solution for Poiseuille flow

Fig. 3.10 depicts the flow velocity distribution at time t = 0.1 s, 0.5 s, 0.8 s and 1.0 s respectively.

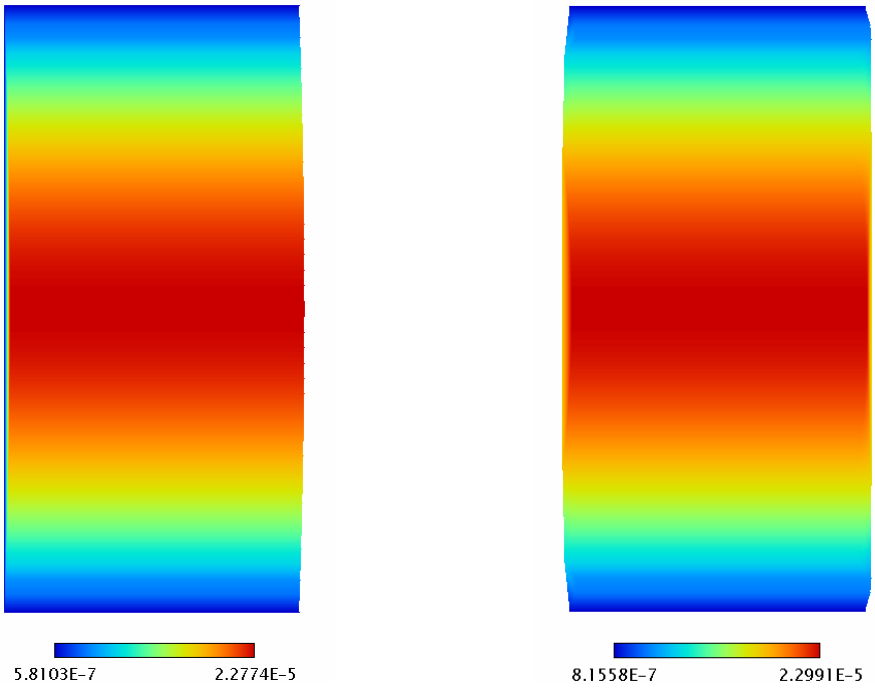

(a) t = 0.1 s (b) t = 0.5 s

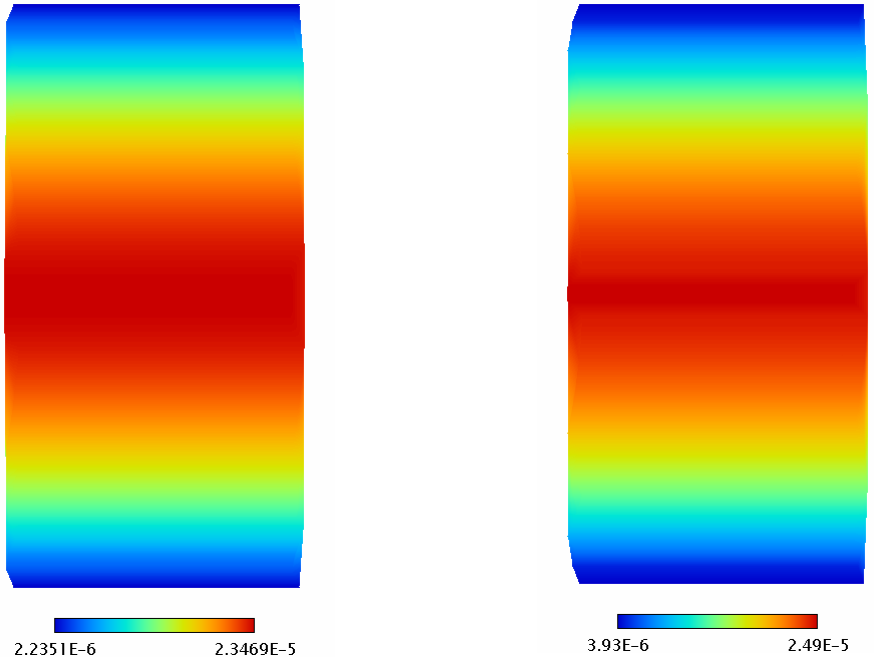

(c) t = 0.8 s (d) t = 1.0 s

Fig. 3. 10: Flow velocity distribution along the channel for 4 times reference

3.5.2 Dam break flow analysis

Another practical benchmark problem often used to validate numerical methods dealing with free surface consists of the dam breaking flow of a water column for which experimental results by Martin and Moyce are available. In this study, a water column of 20 cm high and 20 cm long is released from static equilibrium by removing a barrier wall. The free surface is monitored by assessing the surge front X and the height of the dam h_i at each time step. Fig. 3.11 illustrates a typical dam break flow problem.

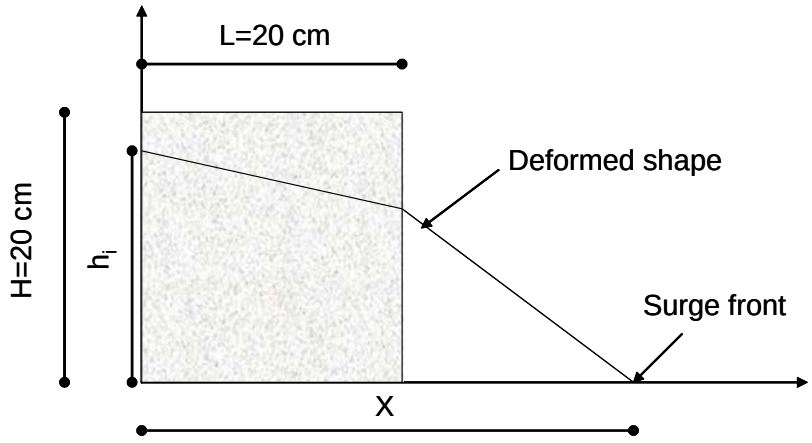

Fig. 3. 11: Initial configuration of the dam break flow

The dam was modeled using 1600 particles equally spaced having an initial distance of 0.5 cm. Solid walls boundaries at the bottom and the left were represented by 200 and 60 particles respectively. Unlike the Poiseuille flow which involves the movement of a stationary fluid driven from initial state by a body force, the flow in the dam breaking problem is induced by gravity after releasing the barrier, and thus the particles will be subjected to forces that do not keep them in order any longer. Accordingly an appropriate value of the smoothing length is chosen to obtain sufficient neighboring particles for smoothing process without altering the particles information. In this specific case, a smoothing length equals to 1.1h is found to give sufficient accuracy. Similarly to the Poiseuille flow, an appropriate sound speed

equal to 20 m/s seems to limit the density fluctuation within a range of 1% tolerance. Table 3.2 summarized the initial parameters used for the dam break flow simulation.

Table 3. 2: Numerical parameters for dam break flow analysis

Dam dimensions	0.2x0.2m
Number of particles	40x40
Density of particles	1000kg/m^3
Viscosity	10^{-6} m^2/s
Time increment	10^{-4}s
Sound speed	20 m/s

While running the simulation using the momentum Eq. (3.22), particle blowup was encountered 0.2 s after the beginning of the simulation. It was necessary to introduce an artificial viscous term into the momentum expression to avoid numerical instability. As its name indicates, the artificial viscosity has no relation with real viscosities. It is only used to stabilize the numerical scheme, prevent particles penetration and allow shock to be simulated. In this study, we employed the standard artificial viscosity proposed by Monaghan (1994) expressed by Eq. (3.30):

$$\Pi_{ij} = \begin{cases} \dfrac{-\alpha_{\Pi} \bar{c}_{ij} \phi_{ij} + \beta_{ij} \phi_{ij}^2}{\bar{\rho}_{ij}} & \text{for } \mathbf{v}_{ij} \cdot \mathbf{x}_{ij} < 0 \\ 0 & \text{for } \mathbf{v}_{ij} \cdot \mathbf{x}_{ij} \geq 0 \end{cases} \tag{3.30}$$

Where,

$$\phi_{ij} = \frac{h_{ij} \mathbf{v}_{ij} \cdot \mathbf{x}_{ij}}{\left|\mathbf{x}_{ij}\right|^2 + \varphi^2} \tag{3.31}$$

and

$$\mathbf{v}_{ij} = \mathbf{v}_i - \mathbf{v}_j ;\ h_{ij} = \frac{1}{2}(h_i + h_j) ;\ \bar{c}_{ij} = \frac{1}{2}(c_i + c_j) ;\ \bar{\rho}_{ij} = \frac{1}{2}(\rho_i + \rho_j) \tag{3.32}$$

According to Monaghan, α_{II}, β_{II} are constants set around 1 and $\varphi = 0.1h_{ij}$ is inserted to prevent numerical divergence when two particles are approaching each other. *c* and **v** are respectively the sound speed and the particle velocity vector.

When adding Eq. (3.30) to the momentum equation, we succeeded in resolving the numerical instability and particularly the particles blowup. However, we noticed that adding the first term of the Eq. (3.30) which involves shear and bulk viscosity brought additional viscosity to the system, and thus decided to disregard it. For the simulation of the dam break flow, only the second term of the artificial viscosity is retained.

Parametric study by varying the value of the constant β_{II} allowed us to find the appropriate range within which the physical phenomena is neither affected nor altered by the presence of coefficient β_{II} , which serves just to stabilize the numerical scheme.

Table 3.3 and 3.4 show the SPH results compared with the experimental ones given by Martin and Moyce (1952) for the normalized surge front X (x/H) and normalized height h (h_i/H) for each normalized time step T ($T = t\sqrt{g/H}$).

Table 3. 3: Results of the parametric study for the normalized surge front

	Exp	β_{II}=0.5	β_{II} =1.	β_{II} =3.	β_{II} =0.1 α_{II}=0.1
T	X	X(SPH)			
0.71	1.33	1.44	1.43	1.44	1.42
1.39	2.25	2.29	2.29	2.29	2.26
2.1	3.22	3.24	3.25	3.24	3.19
3.2	4.8	4.55	4.52	4.5	4.41

Table 3. 4: Results of the parametric study for the normalized height

	Exp	β_{II}=0.5	β_{II} =1.	β_{II} =3.	β_{II} =0.1 α_{II}=0.1
T	h=(h_i/H)	h(SPH)			
0.71	0.9	0.904	0.901	0.901	0.915
1.39	0.76	0.76	0.759	0.767	0.87
2.1	0.57	0.615	0.605	0.608	0.622
3.2	0.32	0.389	0.392	0.39	0.4

As it can be seen from these tables, SPH numerical results obtained by disregarding the term α_{II} give comparable results with experimental ones; particularly for β_{II} = 1. Numerical simulation performed by retaining both constants was also conducted. The results led to a good accuracy provided smaller values of α_{II} and β_{II} are appropriately chosen.

The SPH numerical results of the normalized surge front X and normalized time T are also plotted against the experimental results in fig. 3.12.

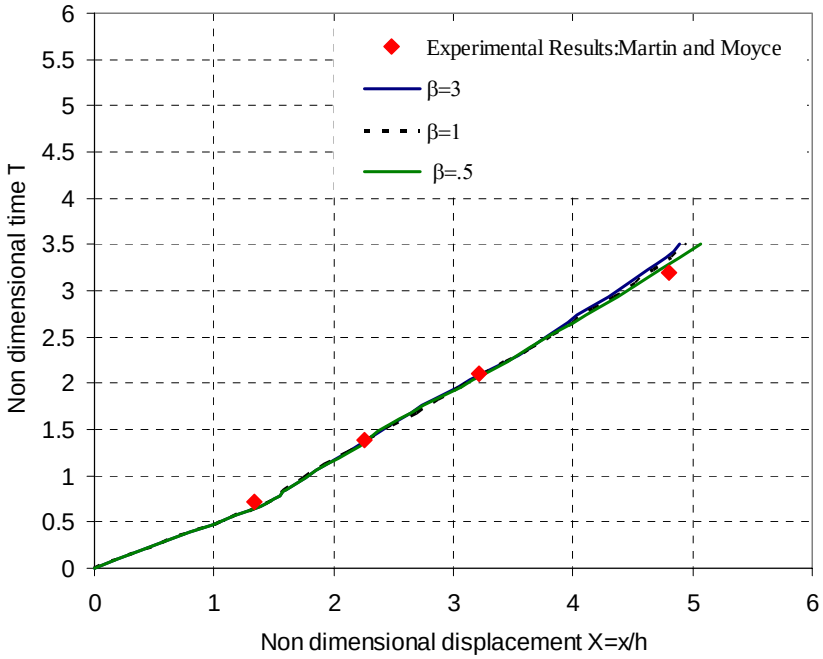

Fig. 3. 12: Non dimensional leading edge versus non dimensional time for the dam break flow analysis of a water column

Fig. 3.12 shows that the curves representing the relationship between the non dimensional leading edge and the non dimensional time are almost coincident during the overall time span although a slight discrepancy is observed for T greater than 3.

Fig. 3.13 illustrates the dam configuration at 3 time steps corresponding to t = 0.1 s, 0.2 s and 0.4 s, respectively, after releasing the wall.

Similarly, Fig. 3.14 depicts the velocity distribution along the dam for the same time steps. It is clearly seen that the front surge is animated with the high velocity which is larger in the downstream than in the upstream.

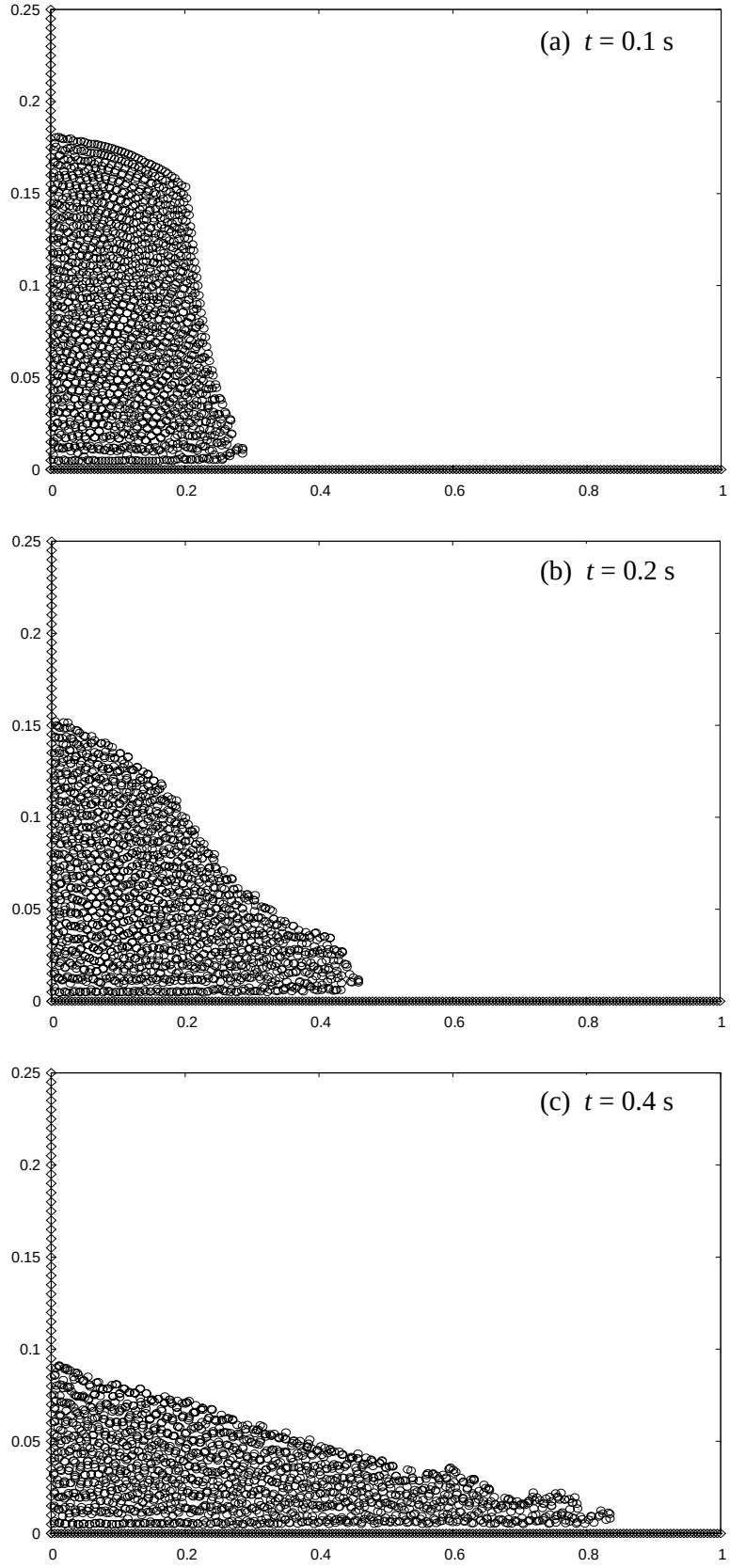

Fig. 3. 13: Dam configuration at t = 0.1 s, 0.2 s and 0.4 s

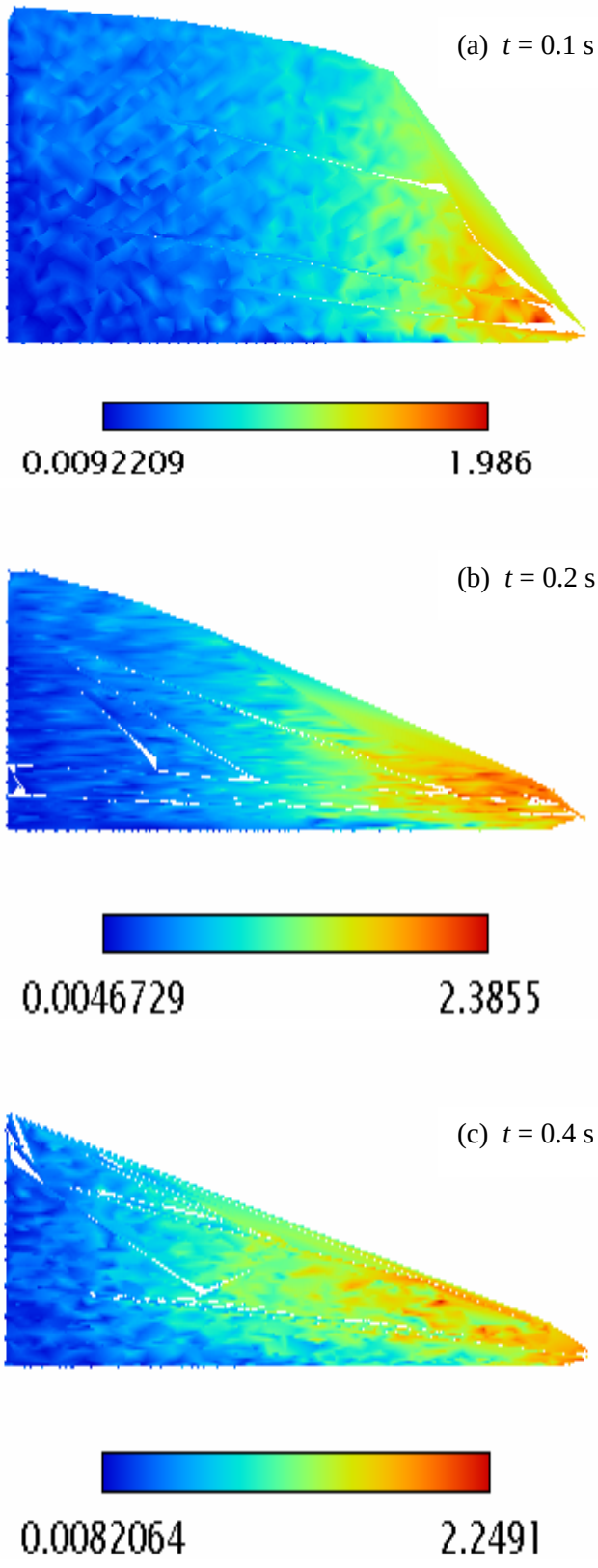

Fig. 3. 14: Velocity distribution at t = 0.1 s, 0.2 s and 0.4 s

3.5.3 Gravity flow simulation

The ability of the SPH to simulate the gravity flow of a Newtonian viscous fluid and a non-Newtonian fluid governed by a Bingham model is attempted in this section. The emphasis is put on simulating the induced displacement as well as the freezing profile when the steady state is reached. One should expect that the free surface for the viscous fluid will reach a level surface at the steady state, while a typical freezing profile denoting the behavior of a Bingham model will be observed for the non-Newtonian fluid.

A typical gravity flow problem simulated here is illustrated in Fig. 3.15.

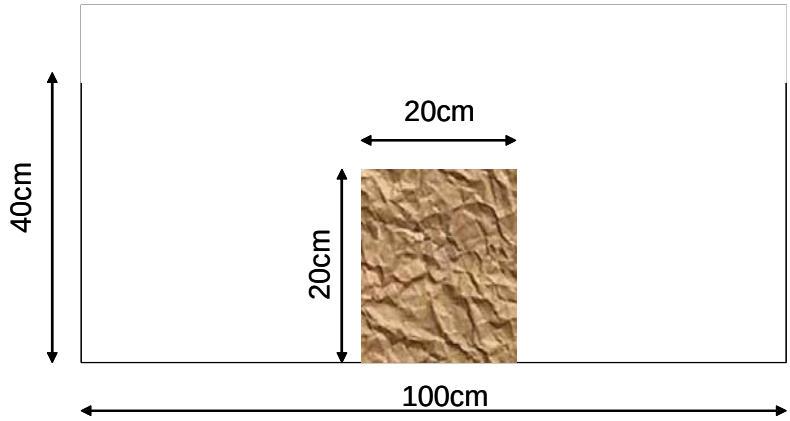

Fig. 3. 15: Numerical representation of the gravity flow problem

Likewise the simulation of the dam break flow of a water column, the same dimensions and number of particles were adopted for both analyses.

The numerical parameters for the gravity flow simulation are shown in Table 3.5 for the case of Newtonian viscous fluid.

Table 3. 5: Numerical parameters for gravity flow of a viscous fluid

Fluid dimensions	0.2x0.2m
Number of particles	40x40
Density of particles	1500kg/m^3
Viscosity	5 Pa·s
Time increment	10^{-4}s
Sound speed	20 m/s

To capture some of the features of the viscous fluid flow, we monitored the time history of the displacement and velocity of one particle located at the extreme hand side at the middle of the fluid column with coordinates X = 60 cm and Y = 10 cm. The time history is depicted in Fig. 3.16.

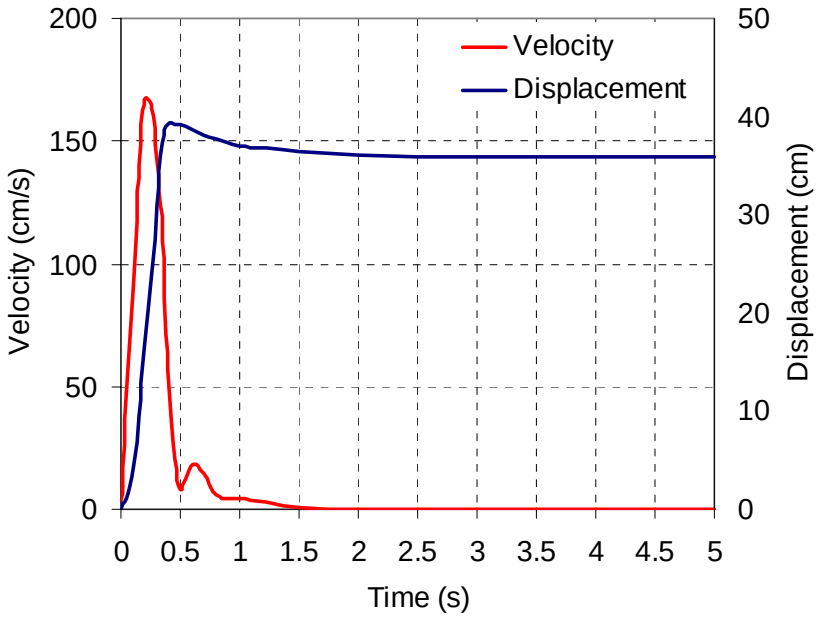

Fig. 3. 16: Displacement and Velocity time history at coordinates X = 60cm, Y = 10cm

When the fluid is released from the initial conditions, the flow is driven by the gravity forces. It starts moving as it gains in kinetic energy. The maximum flow velocity is attained at t = 0.2 s before both sides of the fluid reach the solid boundaries. As the velocity decreases, the maximum displacement is achieved at t = 0.5 s after both sides already have reached the solid walls. The displacement keeps a constant value as the flow is damped by the oscillatory movement of the fluid going back and forth. The free surface attains a level surface and the flow stops moving denoting a state of a stationary conditions. Fig. 3.17 illustrates the free surface configuration at six time steps corresponding to t = 0.1 s, 0.2 s, 0.33 s, 0.5 s, 0.8 s and 5.0 s. It is noted that the contact between the fluid and the solid boundaries occurs at t = 0.33 s.

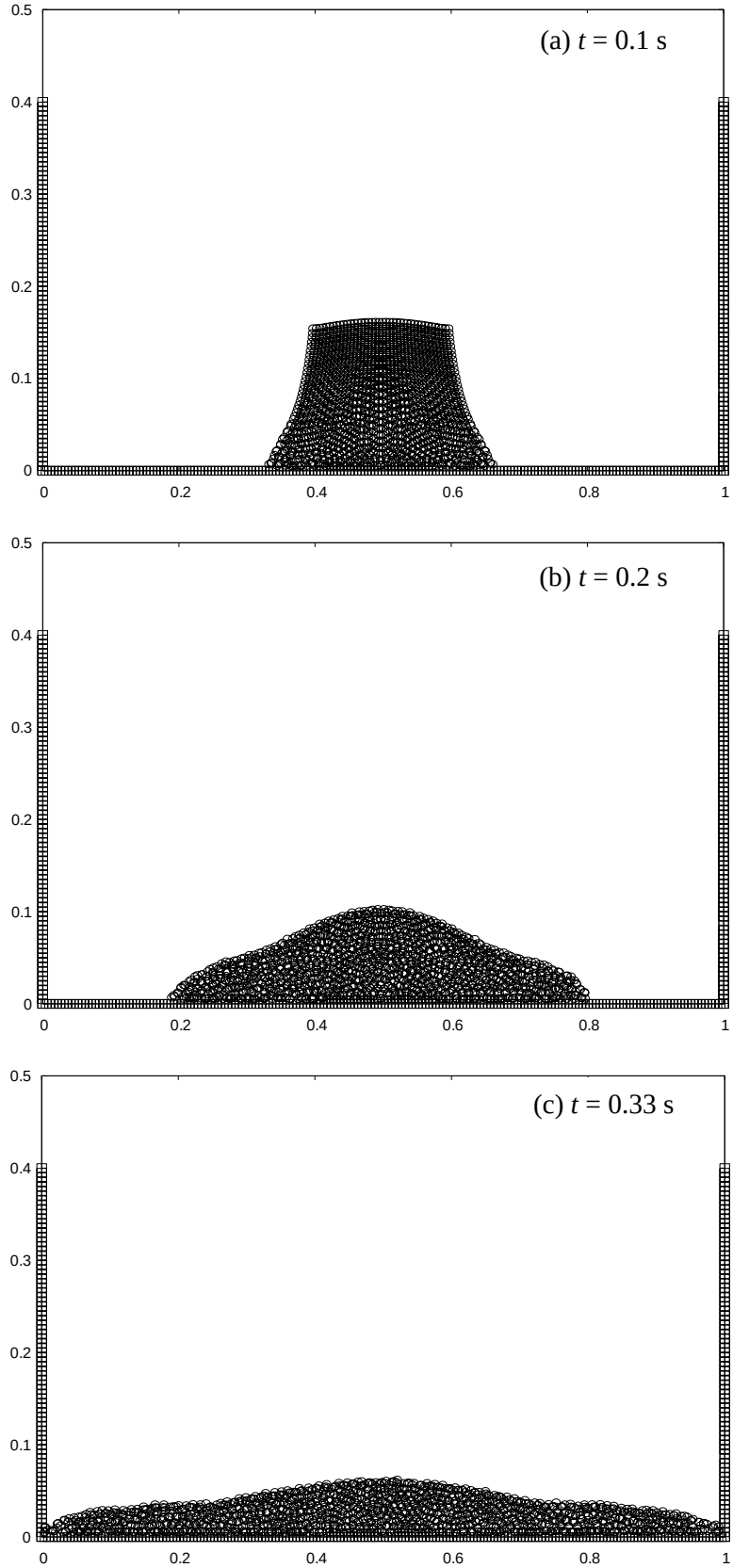

Fig. 3.17: Free surface profile at six time reference

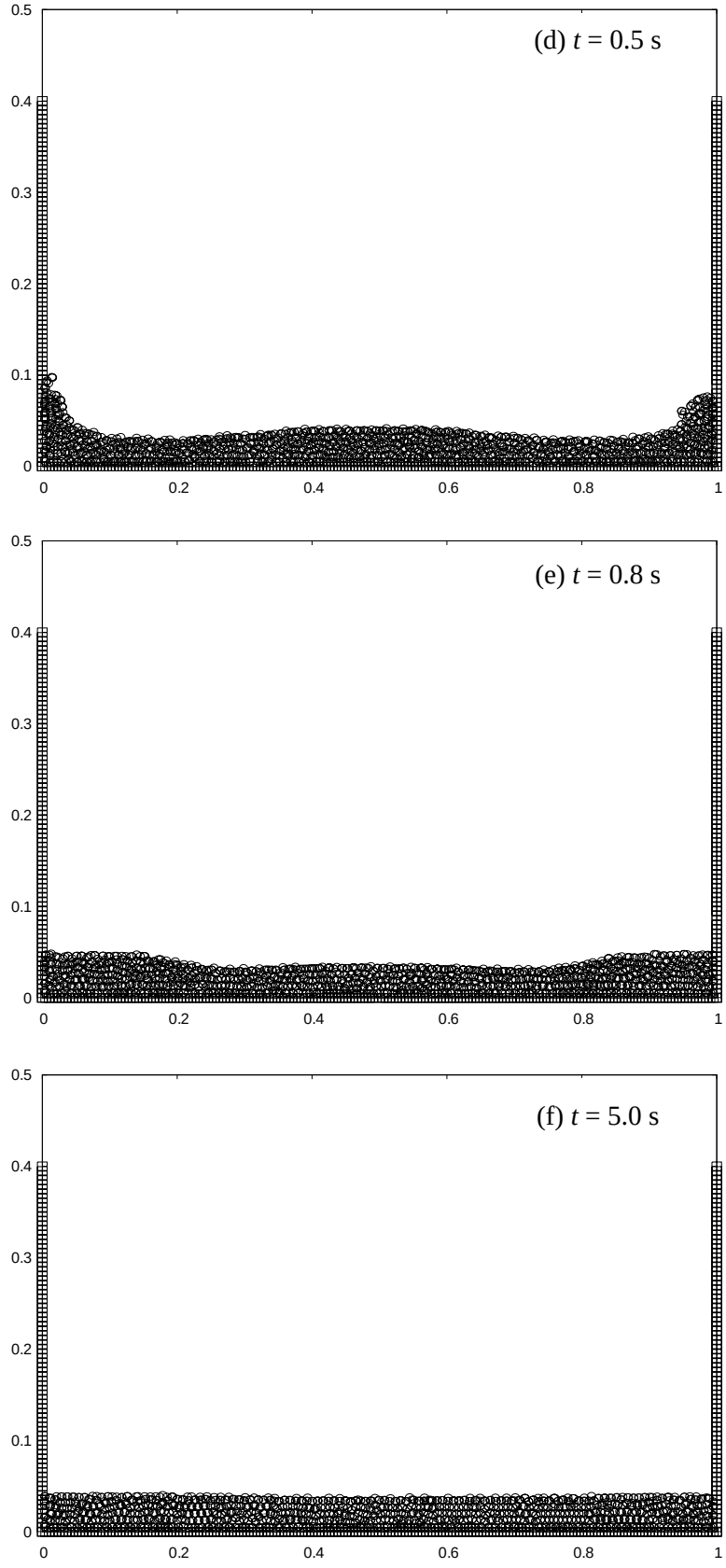

Fig. 3. 17: Free surface profile at six time reference

Simulation of a non-Newtonian water clay mixture governed by a Bingham type constitutive model was conducted using the same numerical setup and the same numerical parameters as in the case of a Newtonian fluid. The related Bingham parameters were taken from the experimental results given by Komatina and Jovanovic (1997), and summarized in Table 3.6.

Table 3. 6: Numerical parameters for gravity flow of a water-clay mixture

Fluid dimensions	0.2x0.2m
Number of particles	40x40
Volumetric concentration (%)	27.4
Density of particles	1452kg/m^3
Plastic viscosity	7x10^{-2} Pa·s
Yield shear stress (Pa)	15.0
Time increment	10^{-4}s
Sound speed	20 m/s

Similarly to the gravity flow of the viscous fluid, the time history of the flow velocity and displacement is computed for the same reference particle and depicted in Fig. 3.19.

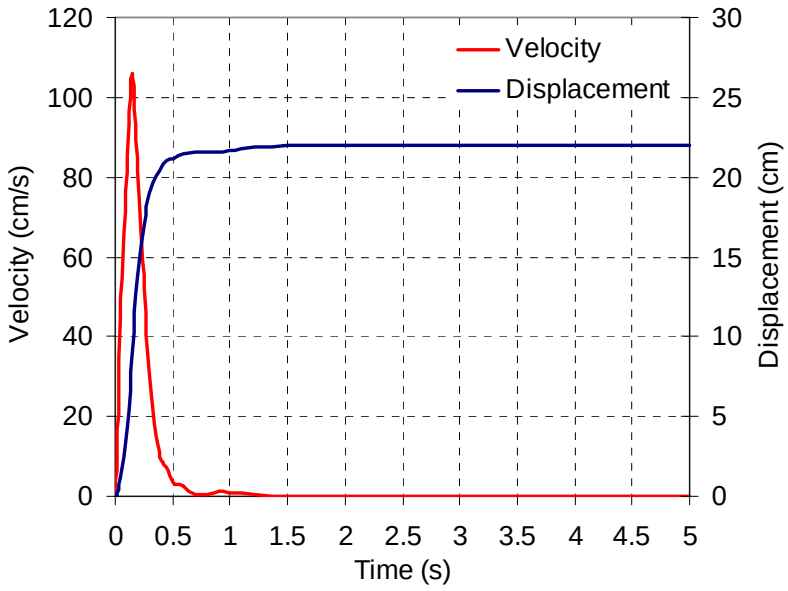

Fig. 3. 18: Time history of the flow velocity and displacement for a non Newtonian water-clay mixture

This figure shows that the maximum flow velocity is reached during the first 0.3 s after releasing the water-clay mixture from its initial condition. The magnitude of the velocity is almost 50% smaller than those obtained for the viscous fluid, while the magnitude of the displacement is half compared to the viscous case. When looking at the general behavior, we could observe some of the features of the non-Newtonian fluid characterized by a rapid decay of the front velocity and a slow propagation of the free surface which freezes when the induced shear stresses drop below the yield shear stress.

The time history of the induced displacement for the same reference particle is plotted in Fig. 3.19 for the case of the viscous fluid and water-clay mixture.

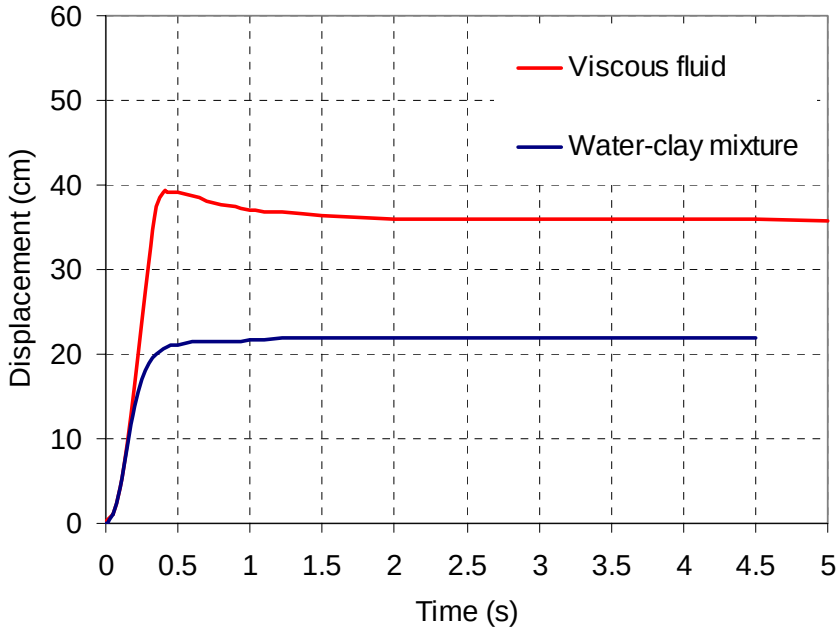

Fig. 3. 19: Displacement time history of a gravity flow problem for a Newtonian and a Non-Newtonian fluid

In the same way, the time history of the flow velocity is plotted for both fluids in Fig. 3.20. The larger is the viscosity, the smaller is the flow velocity for the case of a Newtonian fluid. Moreover, the flow velocity for the non-Newtonian fluid

decreases sharply due to the presence of the yield shear stress, and tends towards an asymptotic zero value.

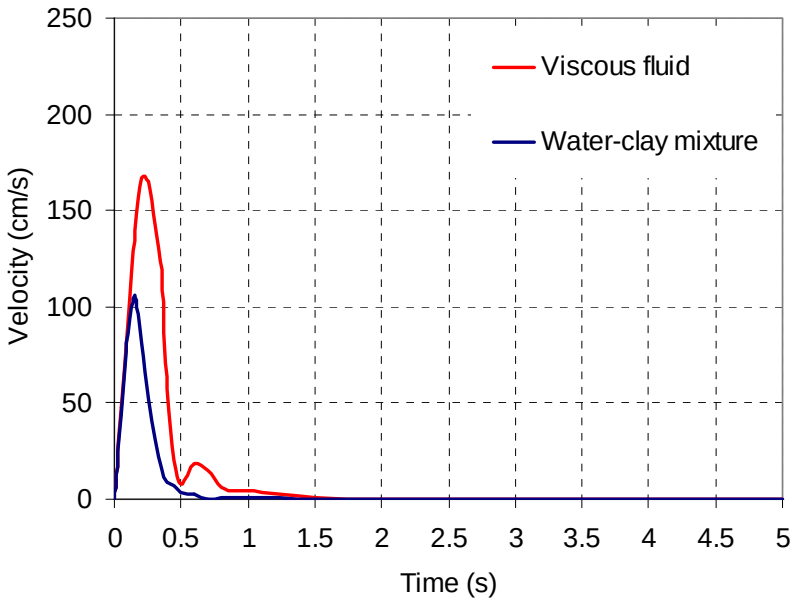

Fig. 3. 20: Velocity time history of a gravity flow problem for a Newtonian and a Non-Newtonian fluid

For the purpose of illustration, the particles configuration of the non-Newtonian fluid are plotted for three different time interval at time t = 0.1 s, t = 0.5 s and t = 1.0 s in Fig. 3.21.

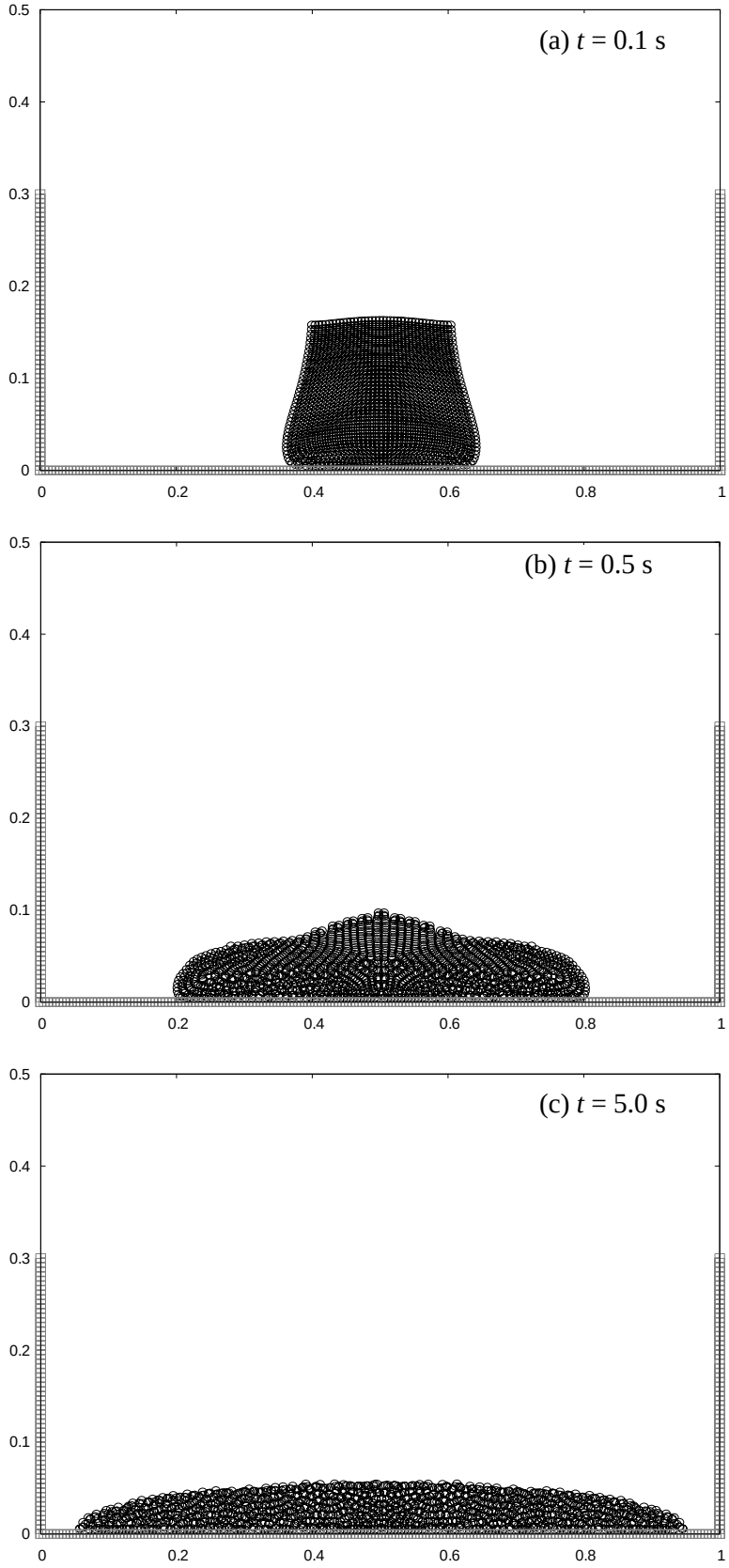

Fig. 3. 21: Particles configuration at t = 0.1 s, t = 0.5 s and t = 5 s

3.6 Summary

This chapter reviewed basic concepts and fundamentals of the smoothed particles hydrodynamics. The governing equations for liquefaction induced lateral spreading analysis were formulated in the framework of fluid dynamics, considering a Bingham type constitutive model for the liquefied soil. An existing educational SPH code was extended to model hydrodynamics problems using material strength. The numerical instability induced by the small values of the shear strain rate at the beginning of the simulation was resolved by adopting a bilinear model rather than the Bingham model. Moreover, particles blowup was solved using an appropriate modified artificial viscosity.

The ability and efficiency of the SPH code to simulate Newtonian flow was validated using two benchmark problems of a Poiseuille flow and a dam break of a water column for which experimental results exist. The SPH results obtained for the case of the Poiseuille flow are in good agreement with the time series solutions proposed by Morris. Additional numerical simulations without experimental validation were carried out to check the capability of the SPH code to simulate a non-Newtonian fluid. For this respect, a gravity flow problem of a water-clay mixture governed by a Bingham type constitutive model was simulated to reproduce the free surface shapes and the time history of the velocity flow and the induced displacement. The results show that the proposed method was able to capture free surface shape, handle large displacement and obtain a consistent time history for the induced displacement and front velocity.

With regards to the previous results, the proposed method is extended in Chapter 4 to simulate lateral spreading obtained by conducting shaking table experiments on liquefied ground.

Chapter 4

Numerical simulations of liquefaction induced lateral spreading

4.1 Introduction

The capability of the SPH method to simulate Newtonian and non Newtonian fluid has been established and introduced in Chapter 3. Its ability to handle large displacement and track free surface was examined on the light of analytical and experimental results. In this chapter, the method is extended to model lateral spreading and assess the induced ground displacement using results of model test conducted on 1g shaking table. The numerical simulations were carried out using the results of 1g shaking tests conducted by Hamada et al (1992, 1994 and 1998).

- - 1g shaking table experiment to investigate the mechanism of the liquefaction induced lateral spreading after the end of the shaking.
- - 1g shaking table experiment to examine and validate the similitude law of the liquefied soil.
- - 1g shaking table experiment to measure the effects of liquefaction induced ground displacements on a pile.

During these simulations, the emphasis concerns the magnitude of the induced displacement, the time history of the flow velocity, the time history of the shear strain as well as the shape of the free surface. Moreover, since the liquefied soil regains its rigidity after the dissipation of the pore water pressure, we attempt to

propose a simple phenomenological constitutive model in which the yield viscosity is only function of the shear strain.

Because dam breaking flow problem of water-clay mixture exhibits several similarities with lateral spreading, we start our numerical simulation by reproducing the experimental results given by Komatina and Jovanovic (1997).

4.2 Dam breaking flow of a water-clay mixture

In this section, numerical simulation of a dam breaking flow of a water-clay mixture is carried out based on the experiments carried out by Komatina and Jovanovic (1997). Komatina and Jovanovic conducted a series of 69 unsteady free surface flow experiments with a range of initial reservoir depth of 10-30 cm, bed slopes 0.0-0.1% and volumetric concentrations 0.0-36.1 %.

The simulation presented here reproduces the experiment for which the initial mixture length a = 2 m, the initial height H = 0.1 m and the bed slope S = 0.1%. The volumetric concentration of the mixture is taken as 27.4% corresponding to a pure water and mud density ρ_m=1452 kg/m^3. According to the experiment, the water-clay mixture has a Bingham yield stress τ_B = 15 Pa and a viscosity μ_B = 70 mPa·s.

The dam is modeled using 2000 particles with an initial spacing of 0.01 m in both directions. To achieve a better incompressibility condition, the sound speed is adjusted so that the density fluctuation is less than 1% during the overall time of calculation. The initial time step Δt is set equal to 10^{-4} s to satisfy the CFL condition.

Likewise the dam breaking problem of a water column, a numerical instability was encountered at t = 2 s after removing the vertical wall from its initial position. In this particular case, the artificial viscosity technique is able to solve the numerical instability. The XSPH technique proposed by Monaghan (1989) has been also attempted to investigate its ability to stabilize the numerical scheme. It is emphasized that only one of these techniques is to be used with the equation of the momentum (Eq.3.22). According to the XSPH technique, each particle moves in a velocity closer to the average velocity of the neighboring particles in accordance with the following equation:

$$\frac{dx_i}{dt} = v_i - \varepsilon \sum_j \frac{m_j}{\rho_j} v_{ij} W_{ij} \qquad (4.1)$$
$$v_{ij} = v_i - v_j$$

In Eq. (4.1), the first term denotes the velocity derived from the Navier-Stockes equation. The second term however represents the product of a parameter ε by the sum of the velocities differences between the particle of interest and its neighboring ones written in SPH formalism. The parameter ε is a constant in the range $0 \le \varepsilon \le 1$.

Since there is no clear criteria on how to select the parameter ε of the XSPH as well as the parameters α and β of the artificial viscosity (Eq.3.30) for this particular problem, we conducted a parametric investigation to find out a suitable range without altering the physical phenomenon by taking as a reference, the experimental results.

The results of this investigation are presented in the form of comparative graphs between the numerical and experimental results by expressing the relationship between the non dimensional leading edge with the non dimensional time.

Fig. 4.1 shows the relationship between the non-dimensional leading edge and the non-dimensional time when the artificial viscosity is taken into account. One can see that the introduction of the coefficient α into the momentum equation bring additional viscosity to the physical problem. As a general rule, provided smaller value of α and β are appropriately chosen, a good agreement can be reached with respect to the physical test results.

Fig. 4.2 depicts the relationship obtained for the case of the XSPH by considering values of ε parameter between 0.001 and 0.1. As it is seen, the smaller is the value of the ε parameter the better is the agreement with the experimental results. This suggests that the ε parameter is only introduced in the expression of the velocity equation to avoid the particles blowup and stabilize the numerical scheme.

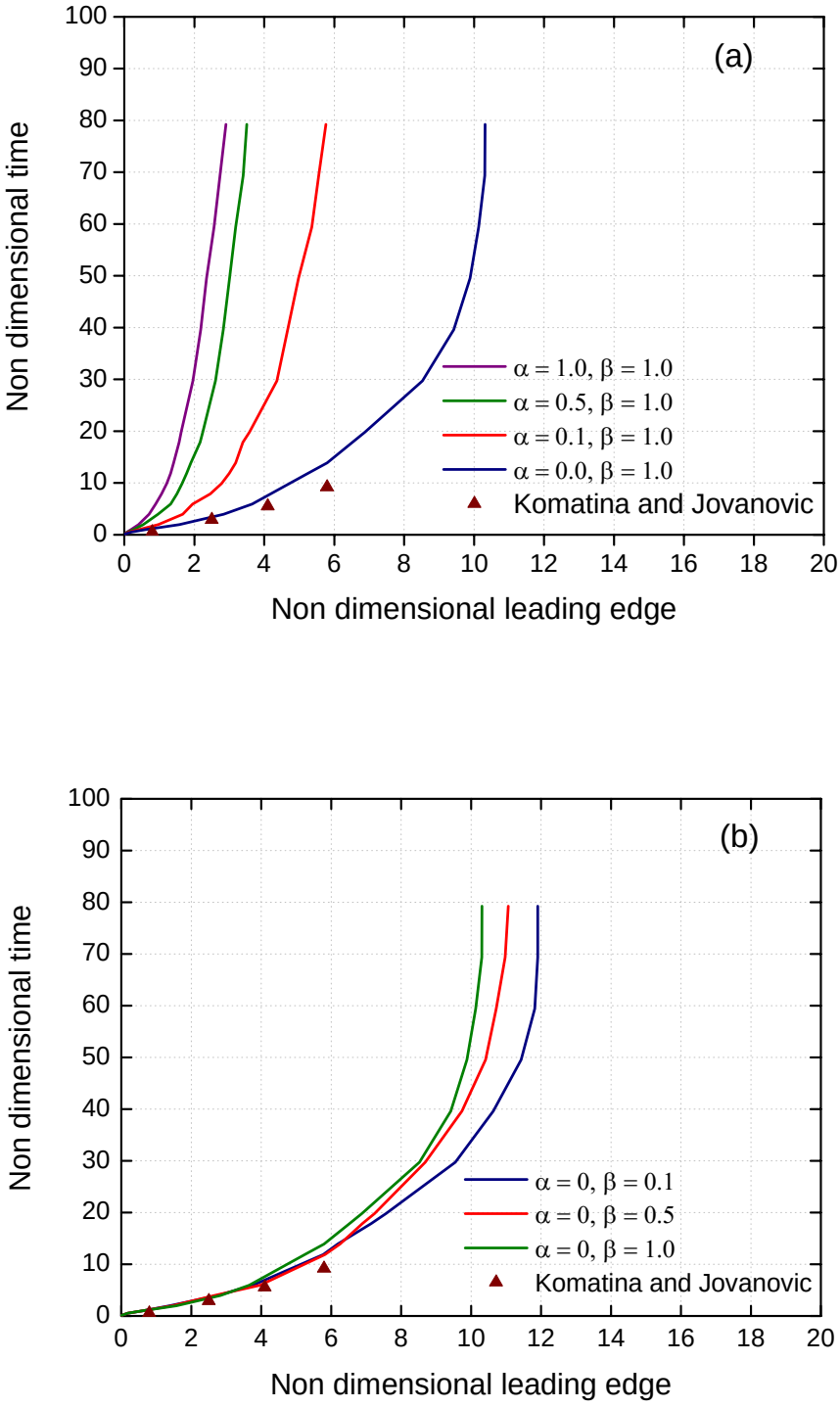

Fig. 4. 1: Relationship between the non-dimensional leading edge with respect to the non-dimensional time for the artificial viscosity technique

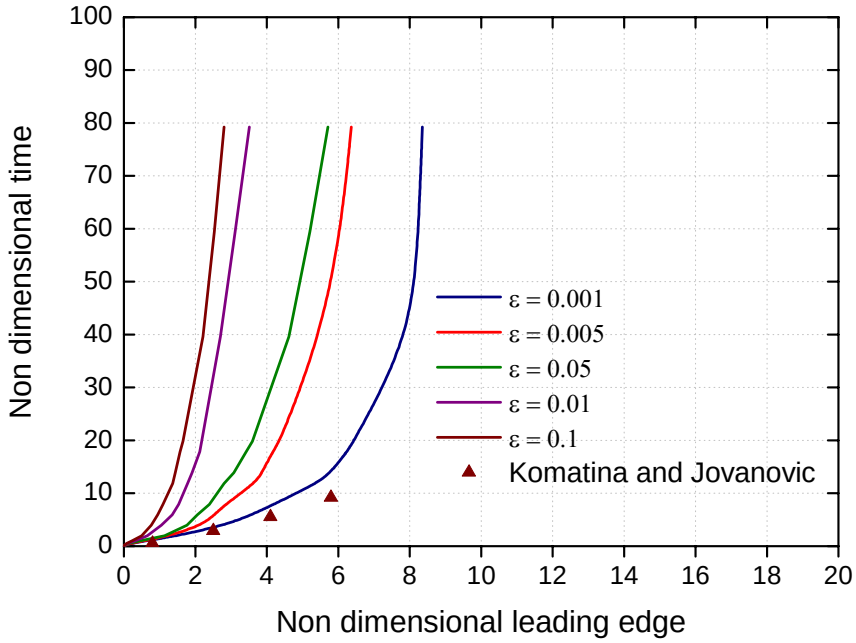

Fig. 4. 2: Relationship between the non-dimensional leading edge with respect to the non-dimensional time for the XSPH technique

The particles distribution at the initial time t = 0 s, 0.2 s, 1.0 s and 8.0 s is shown after the dam break in Fig. 4.3 with parameter ε set to 0.001.

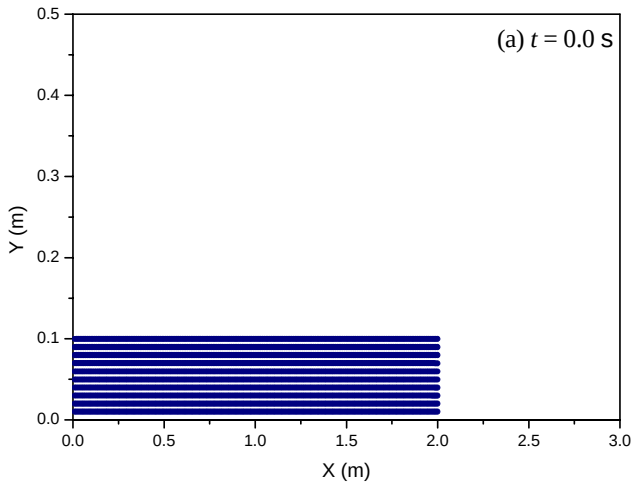

Fig. 4. 3: Flow process configurations at 4 different time reference

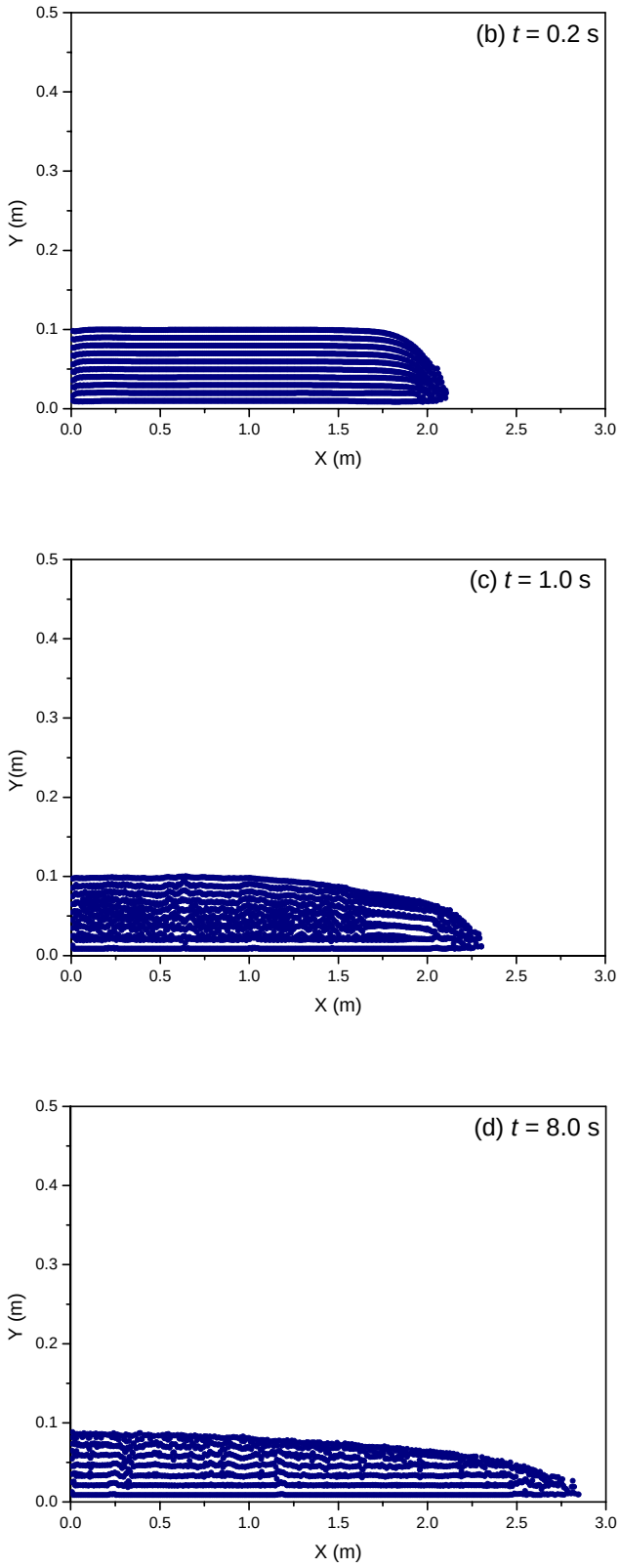

Fig. 4. 3: Flow process configurations at 4 different time reference

From Fig. 4.3, the features of the water-clay mixture flow (mudflow) can be described as follows. Starting from the initial hydrostatic pressure, the dam collapse is characterized by a rapid drop of the flow between t = 0.1 s and t = 1.0 s as the particle's shear stress strength is above the Bingham yield shear stress. In this range, the induced displacement is five times larger than the initial height of the dam. Between t = 1.0 s and t = 8.0 s, a slow decrease of the flow is then observed till reaching a frozen profile at t = 8.0 s when the shear strength drops below the yield shear stress. During this time interval, the induced displacement is about four times larger than the initial height of the dam.

Fig. 4.4 depicts the relationship between the non dimensional leading edge and the non dimensional time obtained for ε = 0.001 and the experimental results derived by Komatina and Jovanovic for both water-clay mixture and pure water.

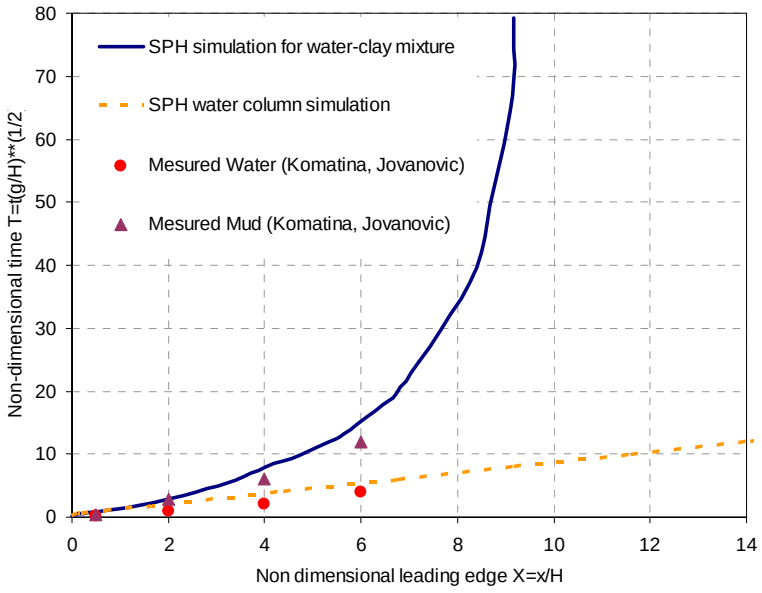

Fig. 4. 4: Relationship between the non-dimensional leading edge versus the non dimensional time

The above figure shows that the propagation of the mudflow travels within a limited distance downstream compared to the water column due to the existence of the yield Bingham stress and the high viscosity at low shear strain rate. According to the simulation results, the water-clay mixture (mud) is frozen downstream after traveling a distance of about nine times of the initial dam's height.

4.3 Numerical simulation of liquefaction induced lateral spread.

To examine the mechanism of the liquefaction induced lateral spreading after the end of the shaking, Hamada et al. (1994) conducted a series of 1g shaking table experiments, in which a model ground with an initial plane surface was constructed in a rigid soil box. The model has 3 m length, 1 m wide and 0.3 m height. The box was vibrated in the lateral direction with a sinusoidal wave acceleration of 100 cm/s^2 until a total liquefaction occurs, and then lifted with a specific gradient using a hydraulic jack as depicted in Fig. 4.5. During the experiment the final shape of the free surface was continuously monitored and the time history of the induced displacements was measured at 3 different depths in the middle of the box as shown in Fig. 4.6.

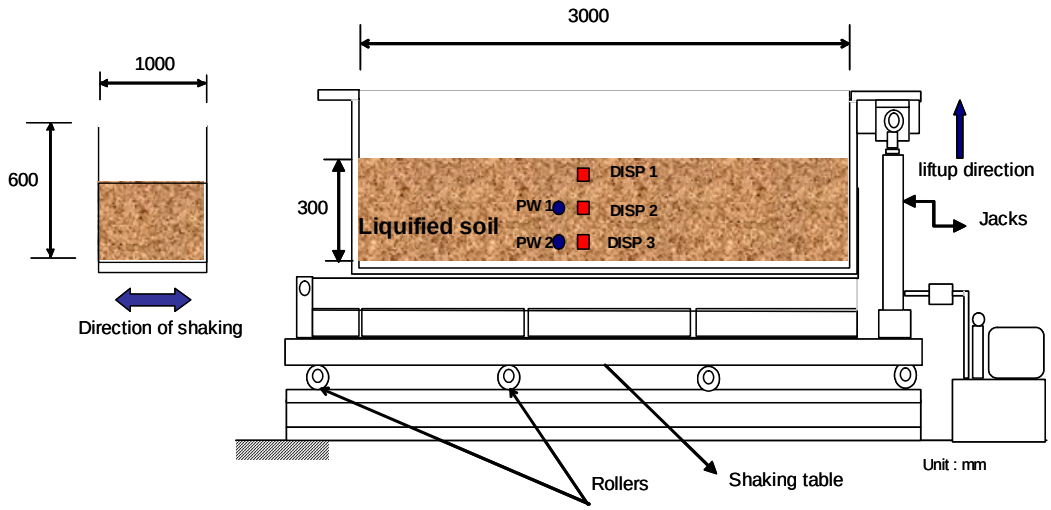

Fig. 4. 5: Experimental setup after Hamada et al.

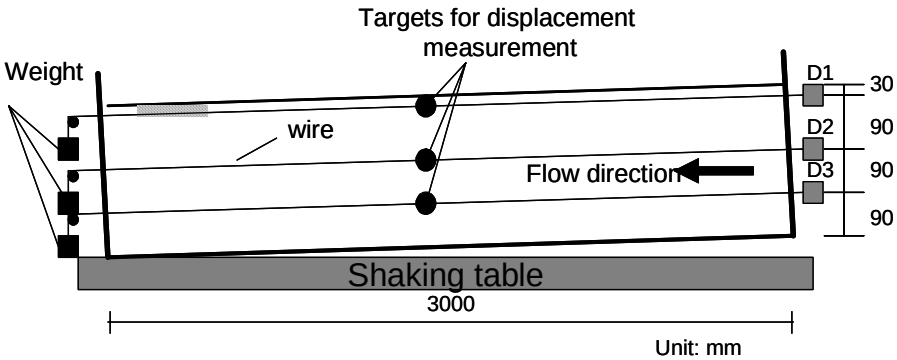

Fig. 4. 6: Experimental setup for the measurement of time history of ground motion after Hamada et al.

During the experiments, several tests were performed by considering an initial relative density between 23% and 61%, and an inclination of the soil box equals to 2.1% and 4.2% respectively.

Table 4.1 below summarizes the different models parameters as well as the obtained physical results.

Table 4. 1: Models parameters for lateral spreading experiment after Hamada and Wakamatsu, (1998)

Experimental cases	Physical parameters			Experimental results			
	D_r (%)	H (cm)	θ (10^{-2})	V_S (cm/s)	μ (gf·s/cm^2)	$\dot{\gamma}$ (1/s)	γ_c
EFM-1	23	23	4.2	14.6	1.3	0.63	0.67
EFM-2	23	25	4.2	14.0	1.7	0.56	0.45
EFM-3	41	25	4.2	7.0	3.4	0.28	0.23
EFM-4	39	26	4.2	7.8	3.3	0.30	0.21
EFM-5	61	24	4.2	2.0	11.4	0.08	0.074
EFM-6	61	22	4.2	2.4	7.9	0.11	0.063
EFM-7	41	27	2.1	7.0	2.0	0.26	0.25
EFM-8	43	28	2.1	6.3	2.4	0.23	0.16

Having access to most of the results pertaining to the experiment EMF-3, this section attempts to reproduce this case with an emphasis on the free surface shape, the time history of the induced displacement and flow velocity as well as the induced shear strain and shear strain rate before and after considering the recovery of the soil rigidity.

Owing to the fact, that it is difficult to reproduce the whole experimental conditions, the input parameters for the numerical simulations were selected on the basis of test observations and obtained results.

Since the constitutive model for the liquefied soil is based on the Bingham type model, the main input parameters consists of the yield viscosity of the liquefied soil, its minimum undrained shear strength as well as the critical shear strain for the recovery of the rigidity.

4.3.1 Selection of the numerical parameters

Many researchers have pointed out the important role that the minimum undrained shear strength plays in controlling the stability of a slope during the occurrence of the liquefaction. Therefore an appropriate estimation of its value constitutes a prerequisite for the overall simulations. In this study, the minimum undrained shear strength is defined as the resistant shear strength required for maintaining the slope into equilibrium. According to Fig. 4.7, it is given by:

$$\tau_{\min} = \gamma h \cos\theta \sin\theta \qquad (4.1)$$

Where γ and h are the saturated unit weight and the thickness of the liquefied soil layer respectively.

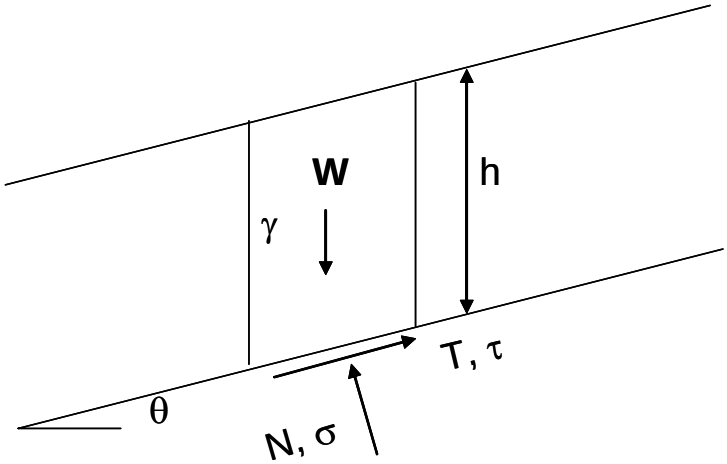

Fig. 4. 7: Schematic definition of the minimum undrained shear strength

The numerical parameters for the Bingham constitutive model (Eq.3.24) for two simulation cases denoted as Case 1 and Case 2 were selected in accordance with the experimental results given in Table 4.1. To investigate the sensitivity of the Bingham model, two values of the yield viscosity were chosen; η_y=0.1 Pa·s and η_y=10 Pa·s that fit the relationship between the viscosity coefficient and the shear strain rate derived by Hamada and Wakamatsu for the lateral spread experiment (Fig. 4.8). The minimum undrained shear strength was computed from Eq. (4.1) at the middle of the liquefied layer thickness by considering a unit saturated weight of

the liquefied soil equals to 18 kN/m^3 and an inclination angle θ = 2% at which the displacements were triggered.

Fig. 4.8 depicts the relationship between the viscosity coefficient and the shear strain rate given in Table 4.1 with respect to the proposed numerical models.

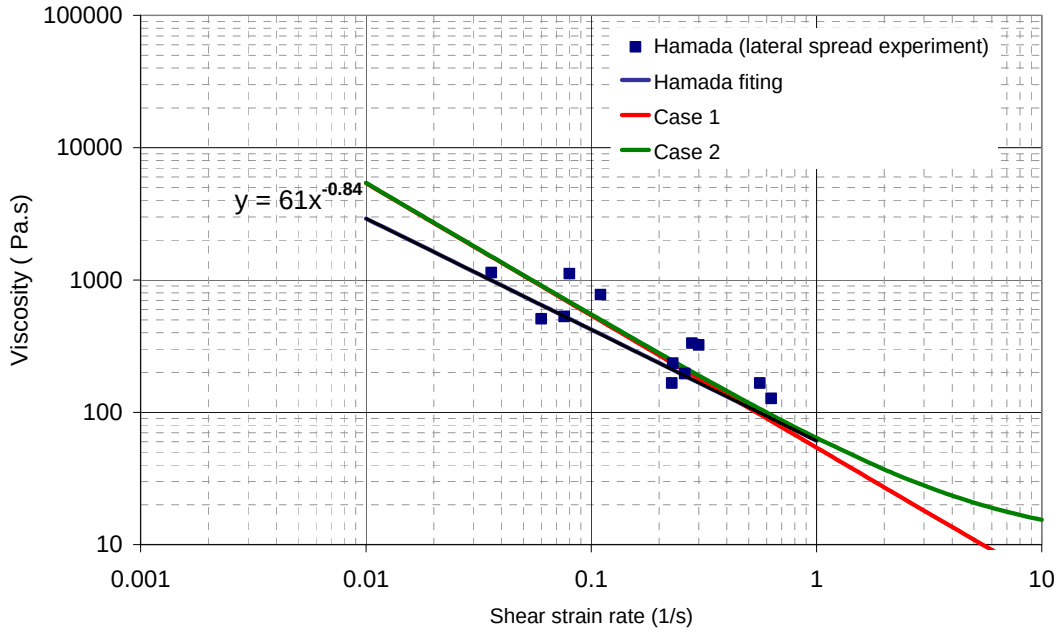

Fig. 4. 8: Relationship between the experimental shear strain rate and the viscosity with respect to the numerical models

The minimum undrained shear strength in Case 1 and Case 2 is kept constant throughout the height of the liquefied soil. Nevertheless, according to Eq. (4.1), the shear strength is a function of the confining pressure. Making use of the experimental results in which the displacement of the liquefied soil was triggered when the soil box reached an inclination θ = 2%, we defined the ratio between the shear strength and the confining pressure as:

$$R = \cos\theta \sin\theta \tag{4.2}$$

Accordingly R takes the value of 0.02 in this case

The particular Case 3, allows us to investigate the effect of the confining pressure on the minimum undrained shear strength and therefore on the induced velocity and displacement. Since the SPH method represents the continuous medium as a set of discrete particles, it is preferable for each particle to be subjected to its own external force according to its position.

Table 4.2 below summarizes the different cases considered for the numerical simulations.

Table 4. 2: Numerical parameters for the Bingham model

Simulation case	Viscosity (Pa·s)	τ_{min} or R (Pa)
1	0.1	54
2	10.	54
3	0.1	0.02

Similarly, the other numerical parameters used for the SPH simulations are shown in Table 4.3.

Table 4. 3: Numerical parameters

Model dimensions	3.x 0.3m
Number of particles	150x15
Initial spacing	0.02 m
Density of particles	1800kg/m^3
Time increment	10^{-4}s
Sound speed	50 m/s
ε (XSPH)	0.3

As a first stage, the numerical simulations are carried out without taking into account the recovery of the rigidity to analyze the incidence on the different parameters (displacement, velocity, strain and free surface). Latter, the recovery

model will be introduced in an attempt to reproduce with a consistent manner the experimental results.

4.3.2 Numerical setup

Because it is impossible to simulate the whole experimental process starting from the shaking phase up to the lifting of the soil box, the numerical model was reproduced in 2D at the final stage when the soil box reached its final position. Since the shaking was applied in the lateral direction, the only external forces acting on the model consist of the gravitational force. Fig. 4.9 shows the numerical model at the initial configuration.

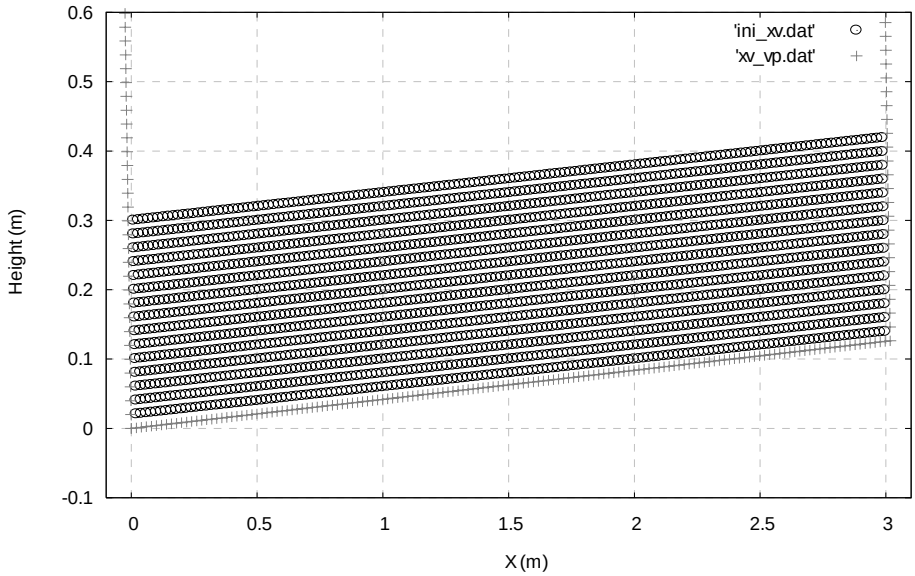

Fig. 4. 9: Initial configuration at t = 0 s

4.3.3 Simulations results

- Free surface shape

Similarly to the previous simulations involving Newtonian and non-Newtonian fluid, the artificial viscosity term was taken into account to stabilize the numerical scheme. However, shortly after the beginning of the computational process, we encountered particles blow-up which denotes an occurrence of a numerical instability. Several preliminary simulations to select the appropriate value of the coefficients α and β were attempted. However, the numerical scheme was difficult to

stabilize during the overall simulation span, since the particles at the bottom of the soil box undergo a continuing disorder movement with a clear compression zone observed at the downstream. It seems that the artificial viscosity technique is unable to handle properly problems involving movement of fluid confined between boundary walls. To overcome this instability, we made use of the XSPH technique proposed by Monaghan (1989). By conducting several preliminary simulations, we concluded that a value of 0.3 of the parameter ε was able to suppress the numerical instability in this simulation. Fig. 4.10 shows the obtained free surface shape for the three simulated cases.

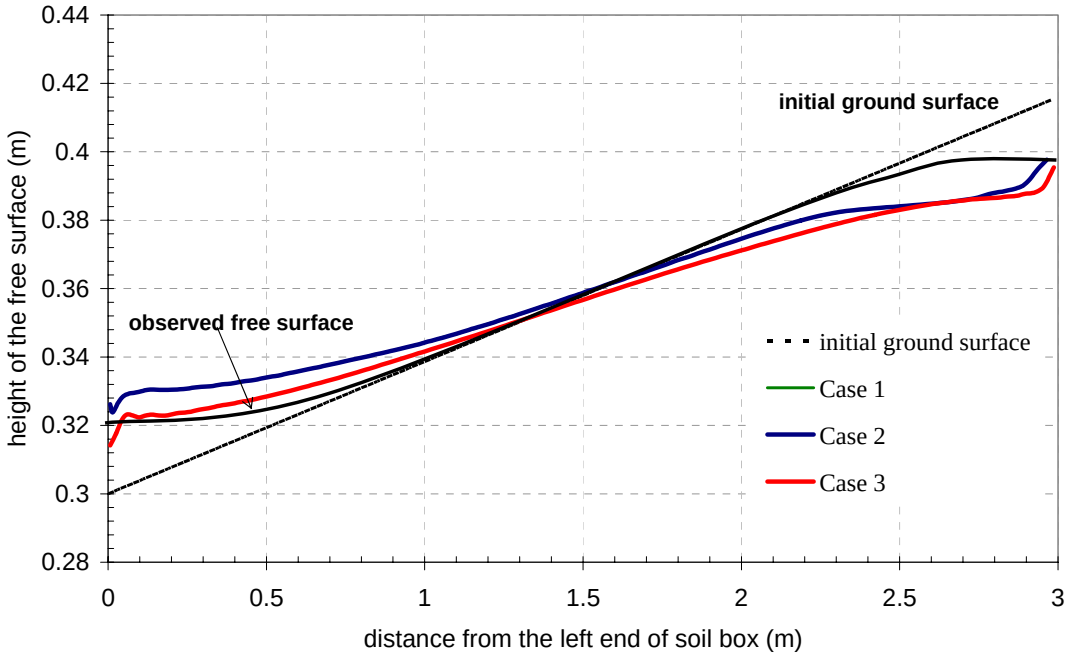

Fig. 4. 10: Simulated free surface shapes

In Fig. 4.10, the general trend of the observed free surface during the experiment is roughly reproduced for Case1 and Case 2. The upstream part subsided due to gravity and the downstream heaved due to volume transfer from the upstream; the central part didn't keep its initial inclination, where a slight rotation can be observed with respect to the initial ground surface. This trend can be seen also by plotting the vector displacements at the top of the free surface for Case 1 as shown in Fig. 4.11.

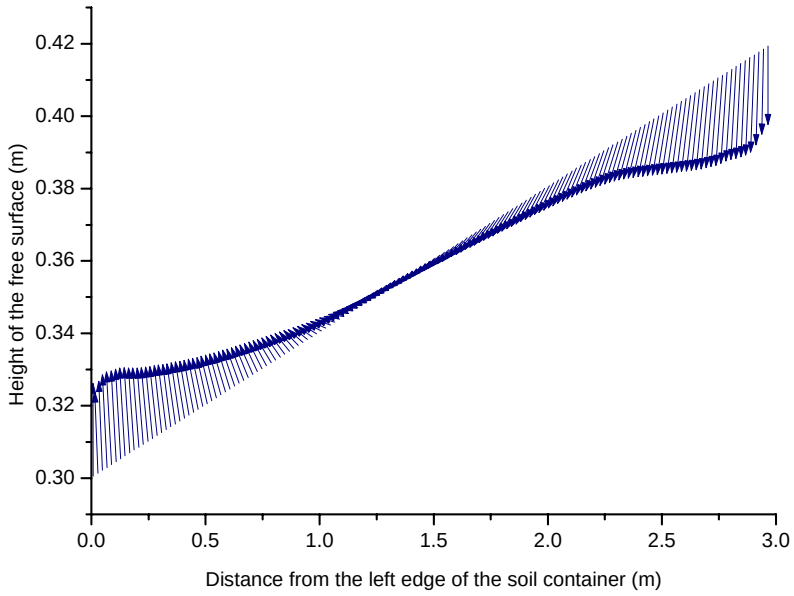

Fig. 4. 11: Vector displacements at the top of the free surface for Case 1

Since the free surface shapes in Case 1 and Case 2 are superimposed, we may conclude that the Bingham model is insensitive to the yield viscosity. A possible reason for this phenomenon could be related to the range of the induced shear strain rate that causes the equivalent viscosity to be within same level.

Similarly, we observed a subsidence in the upstream and a heaving in the downstream for Case 3. However, the central part of the induced free surface did not keep the same inclination as the initial ground surface, though in the downstream region, the free surface fits the observed one with an acceptable accuracy. This could be related to a continuous flow of liquefied soil.

- Time history of the ground flow velocity

Fig. 4.12 illustrates the time history of the ground flow velocity for Case 1 at three elevations computed at the central cross section as shown in Fig. 4.2. Since the induced free surface is insensitive to the yield viscosity, similar results for the time history of flow velocity were found for Case 2.

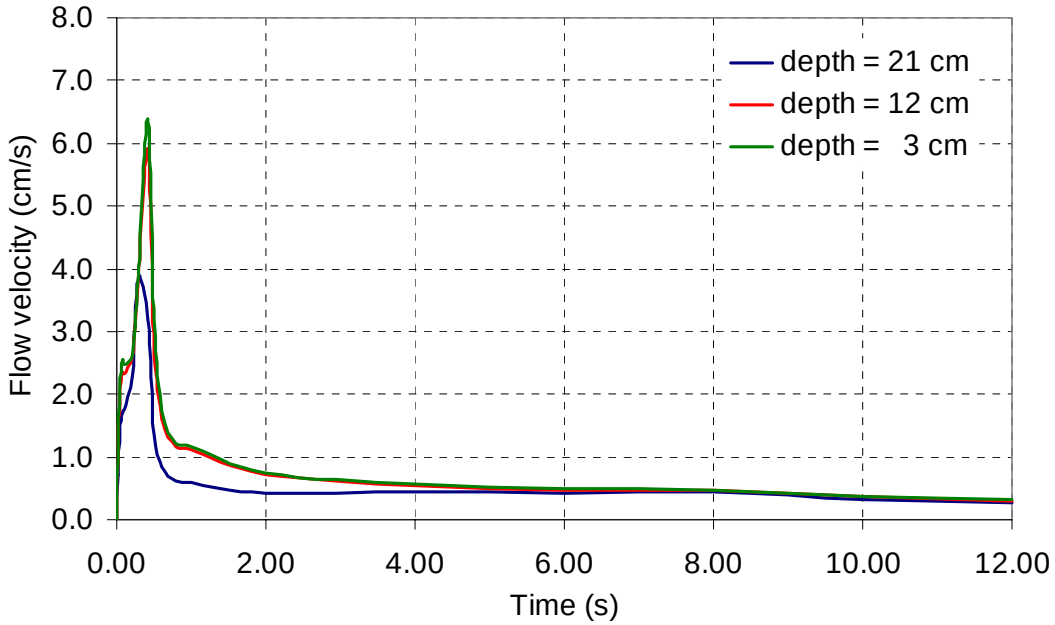

Fig. 4. 12: Time history of the ground flow velocity for Case 1

The simulated maximum ground flow velocity is closer to the experimental one given in Table 4.1. However, the flow velocity at the bottom of the soil container is overestimated. Moreover, the soil continues flowing with a velocity equals to 1/20 of the maximum velocity during the overall simulation time interval. This result is not in agreement with the experimental one, in which the soil stops flowing immediately after the ground flow velocity reached its maximum value. The reason may be related to the dissipation of the pore water pressure and the recovery of the rigidity which were not taken into account in this simulation.

Similarly, the time history of the ground flow velocity for Case 3 is depicted in Fig. 4.13.

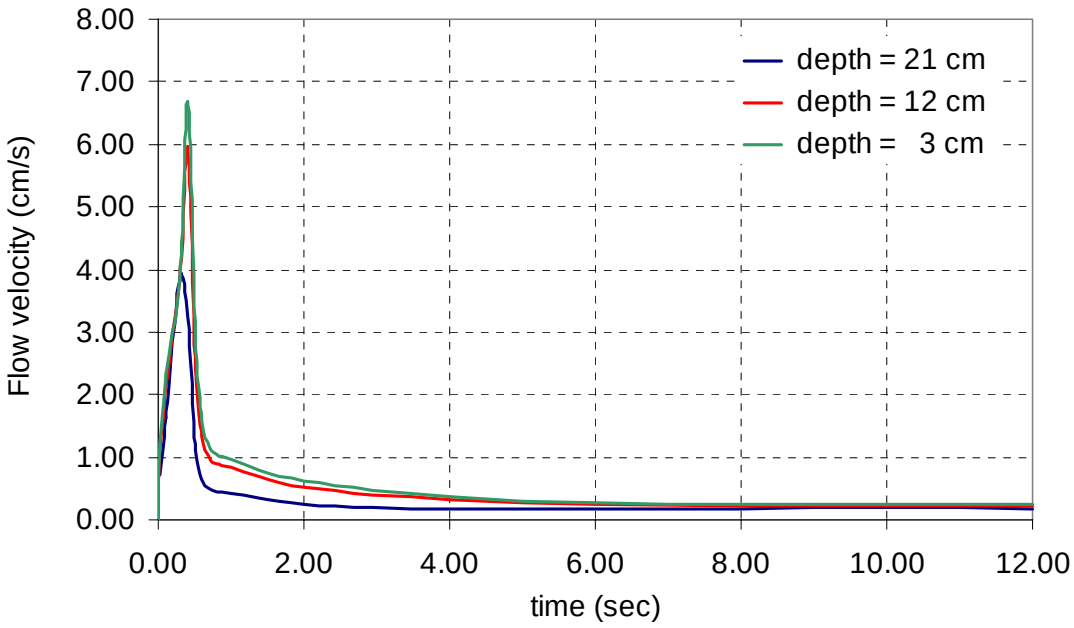

Fig. 4. 13: Time history of the ground flow velocity for Case 3

As observed from this figure, the maximum value of the simulated ground flow velocity at depth h = 3 cm is closer to the experimental one. However, the velocities at the middle of the cross section as well as at the bottom of the soil container are overestimated. Likewise the Case 1, the liquefied soil continues flowing with a magnitude equals to 1/30 of its maximum value.

- Time history of the ground flow displacements

The time history of the maximum induced lateral ground displacement is illustrated in Fig. 4.14 for Case 1. Likewise the time history of the ground flow velocity, the induced displacements are given at the central cross section for three respective elevations.

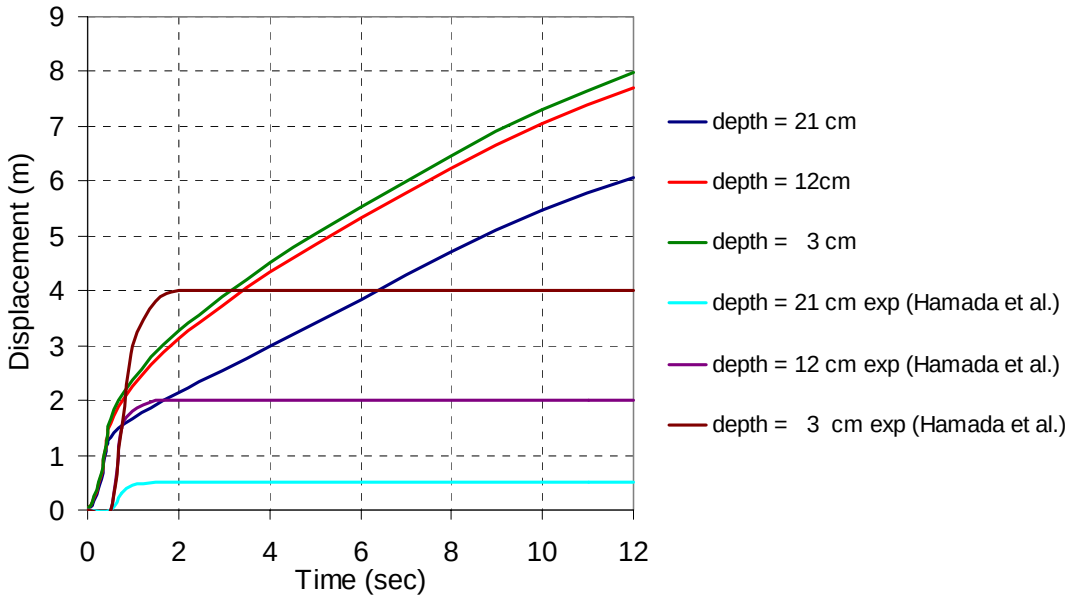

Fig. 4. 14: Time history of the ground flow displacement for Case 1

Fig.4.14 clearly shows that neither the magnitudes of the induced displacement nor the general trend of the simulated curves do fit the experimental ones. In fact, the magnitude at depth h = 3 cm is twice the observed one. Furthermore, the induced displacement at depth h = 12 cm is closer to that at depth h = 3 cm, suggesting that the upper layer deforms as a rigid body over the adjacent lower one. Similarly, the displacement at the bottom of the soil container is overestimated. Besides this, the general trend observed during the experiment in which the soil attains a maximum constant value is not reproduced. This discrepancy can be related to the high equivalent viscosity induced at small shear strain rate due, to some extent, to the constant value of the minimum undrained shear strength along the height. Another plausible explanation is associated with the high shear strain encountered at the bottom of the soil container. Since the recovery of the rigidity is not taken into account, the shear strain is not transferred to the upper adjacent layer causing them to deform as a rigid body.

Similarly, Fig. 4.15 depicts the time history of the maximum induced lateral ground displacement for Case 3. Unlike the previous case, the general trend of the ground displacement is consistent with the experimental one between the range 0-2s and the model do not suffer anymore from the high viscosity at the small strain rate.

This is attributed to the induced minimum undrained shear strength which rather depends on the confining pressure in this case. However, the displacements at the three elevations increase continuously during the whole time span of the simulation. In terms of magnitude, the maximum displacement at depth h = 3 cm is 1.75 times larger than the observed one, while it is 2.75 times larger at depth h = 12 cm. At the bottom, the simulated displacement is also overestimated.

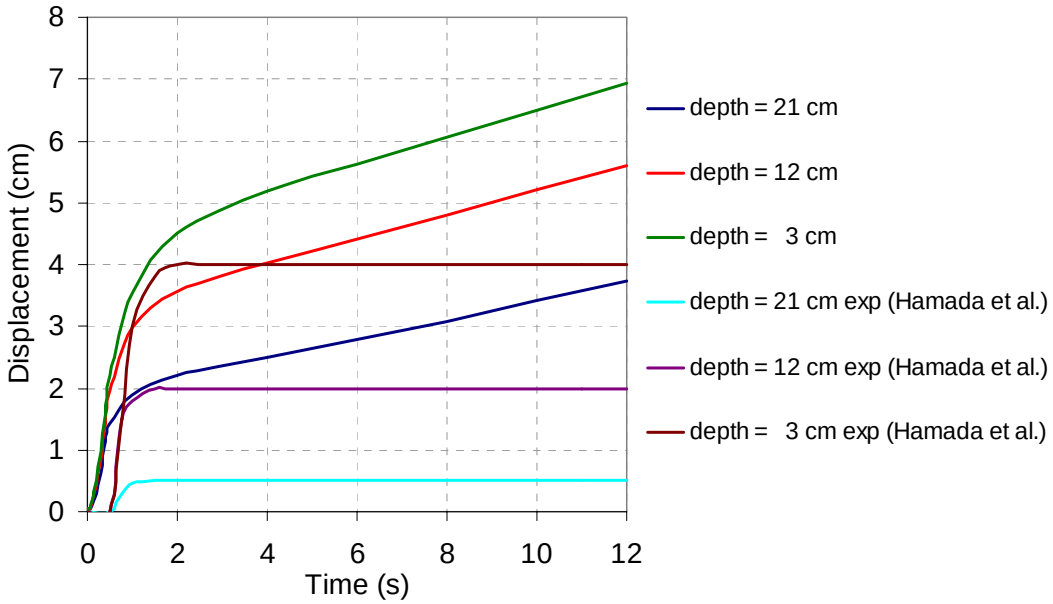

Fig. 4. 15: Time history of the ground flow displacement for Case 3

- Induced maximum shear strain rate.

The time history of the induced shear strain rate versus the equivalent Bingham viscosity was computed for Case 1 and Case 3, and the results were compared with those obtained by Hamada and Wakamatsu (1998) and given in Table 4.1.

Figures 4.16 and 4.17 show the relationship between the simulated shear strain rate versus the equivalent viscosity for Case 1 and Case 3 respectively.

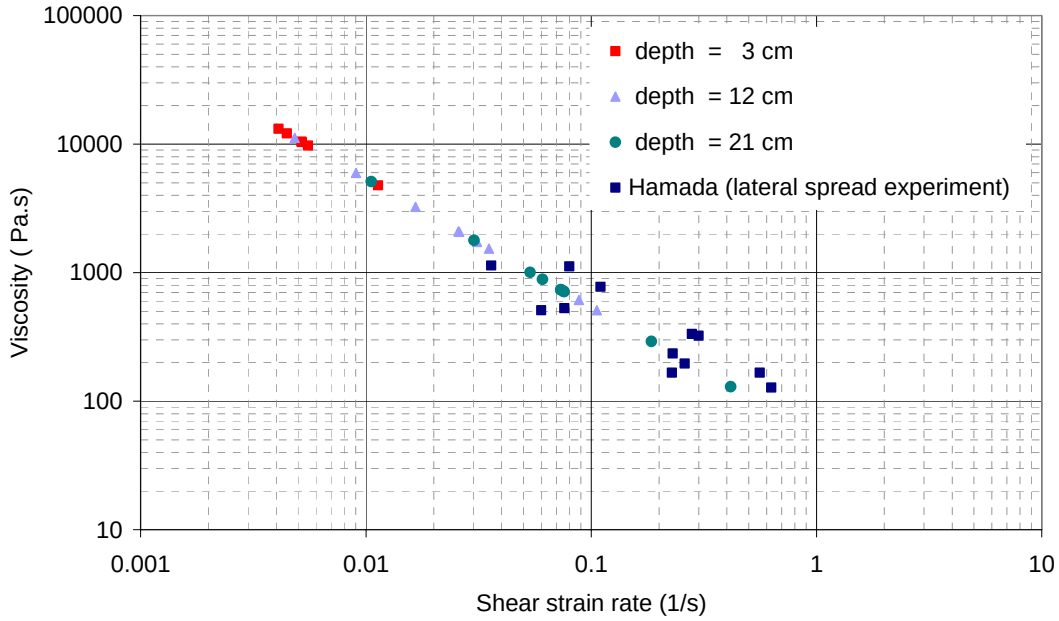

Fig. 4. 16: Relationship between the equivalent viscosity and the induced shear strain rate Case 1

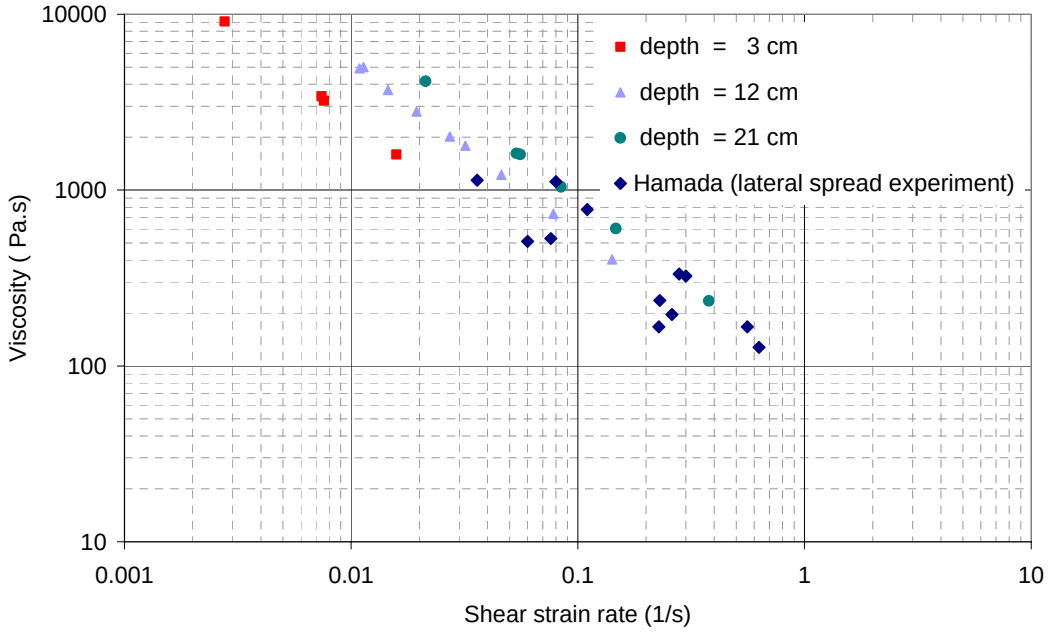

Fig. 4. 17: Relationship between the equivalent viscosity and the induced shear strain rate Case 3

In Fig. 4.16, the induced shear strain rate lay on a straight line which is nothing else than the Bingham model imposed for the simulation. The magnitude of the simulated shear strain rate at depth h = 21 cm is closer to the value of 0.30 (1/s) given by Hamada and Wakamatsu in Table 4.1. The range of the induced values of the shear strain rate at depth h = 3 cm explains in a consistent manner the small displacement we encountered at the top of the soil container.

Unlike the Case 1, the induced shear strain rate depicted in Fig. 4.17 lay on a three straight lines since the minimum undrained shear strength is a function of the confining pressure in Case 3. In terms of magnitude, the obtained results are within a consistent range with respect to the experimental value shown in Table 4.1.

- Time history of the induced shear strain

The time history of the induced shear strain was computed at three elevations from the time history of the induced shear strain rate by simple integration. This not only helps us to visualize the distribution of the shear strain within the liquefied soil, but also to select the critical value of the shear strain above which the soil regains its rigidity.

The time history for each simulated case is given for each component of the shear strain tensor as well as for the second invariant of the deviatoric shear strain.

Figures 4.18, 4.19 and 4.20 depict the time history for each component of the strain tensor for Case 1 at depth h = 3 cm, h = 12 cm and h = 21 cm respectively. The strain tensor components in these figures are denoted as ε_{xx}, ε_{yy}, ε_{xy} in the normal and transversal direction respectively, while γ represents the second invariant of the strain tensor given as follows.

$$\gamma = \sqrt{\frac{1}{2}\varepsilon_{ij}\varepsilon_{ij}} \qquad (4.3)$$

Where : ε_{ij} represent the component of the strain tensor.

The volume of the liquefied soil is well conserved as illustrated in these figures: the normal components of the strain tensor are equals in magnitude, while the absolute value of the shear strain in transversal direction is equals in magnitude to the second invariant of the strain tensor.

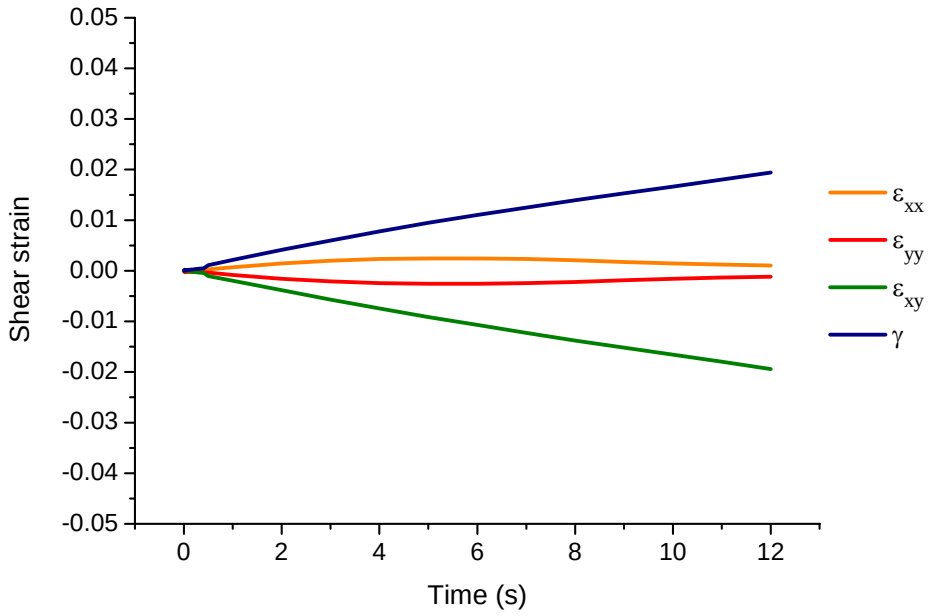

Fig. 4. 18: Time history of the induced shear strain components at depth h = 3 cm for Case 1

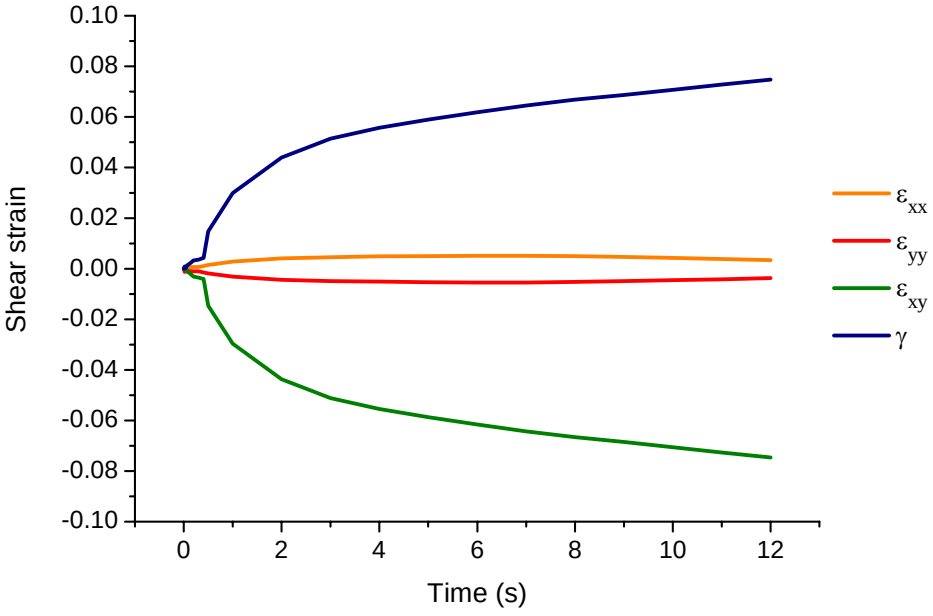

Fig. 4. 19: Time history of the induced shear strain components at depth h = 12 cm for Case 1

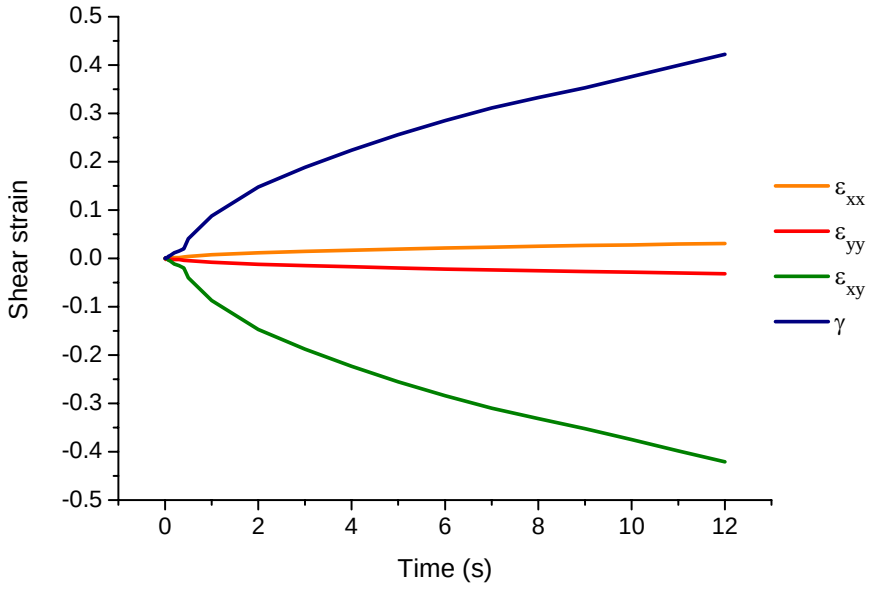

Fig. 4. 20: Time history of the induced shear strain components at depth h = 21 cm for Case 1

The time histories of the second invariant of the strain tensor at different depths are replotted and compared in Fig.4.21.

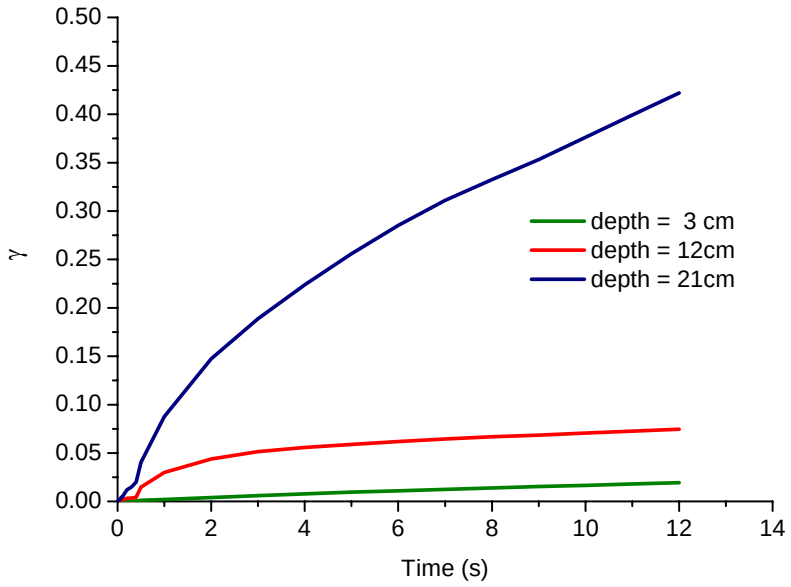

Fig. 4. 21: Time history of the second invariant of strain tensor for Case 1

In terms of magnitude of the shear strain, we can see in the above figure that the maximum shear strain occurs at depth *h* = 21 cm with a magnitude of more than 40 %, while at depth h = 12 cm and h = 3 cm the level of shear strain do not reach a level of 10 %. This result is consistent with the simulated induced lateral ground displacement, particularly at depth *h* = 21 cm, which caused the upper adjacent layer to move as a rigid body.

Likewise Case 1, figures 4.22, 4.23 and 4.24 illustrate the time history for each component of the strain tensor for Case 3 at depth *h* = 3 cm, *h* = 12 cm and *h* = 21 cm respectively.

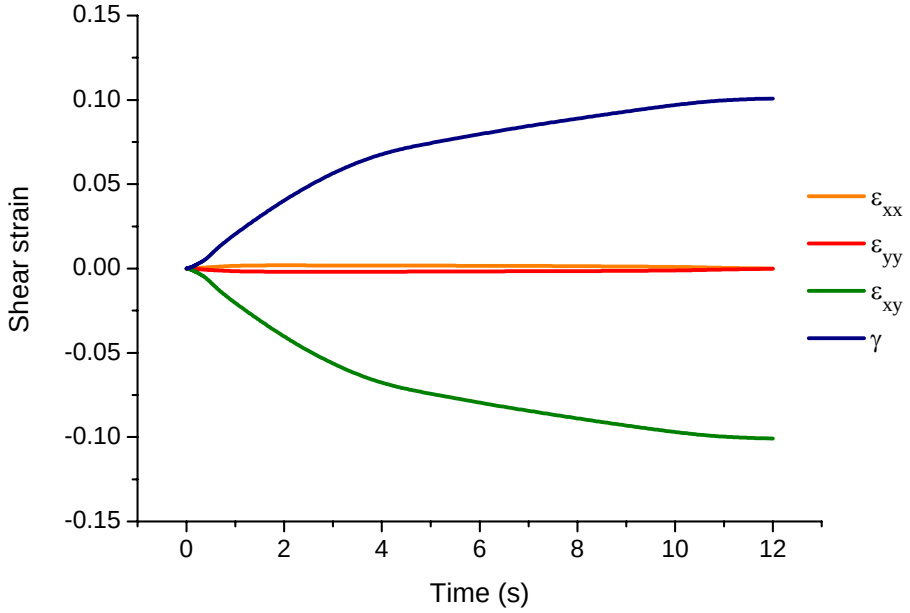

Fig. 4. 22: Time history of the induced shear strain components at depth *h* = 3 cm for Case 3

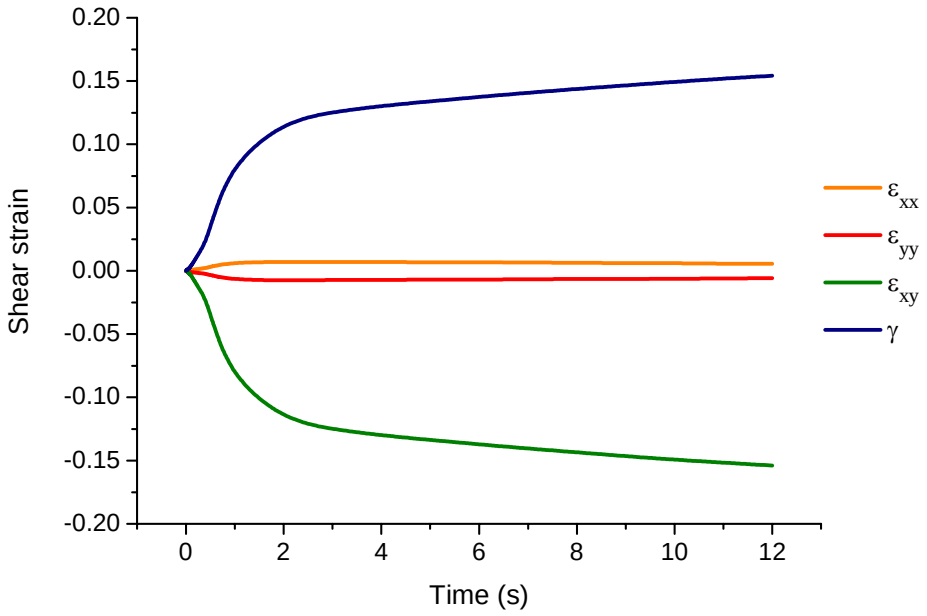

Fig. 4. 23: Time history of the induced shear strain components at depth h = 12 cm for Case 3

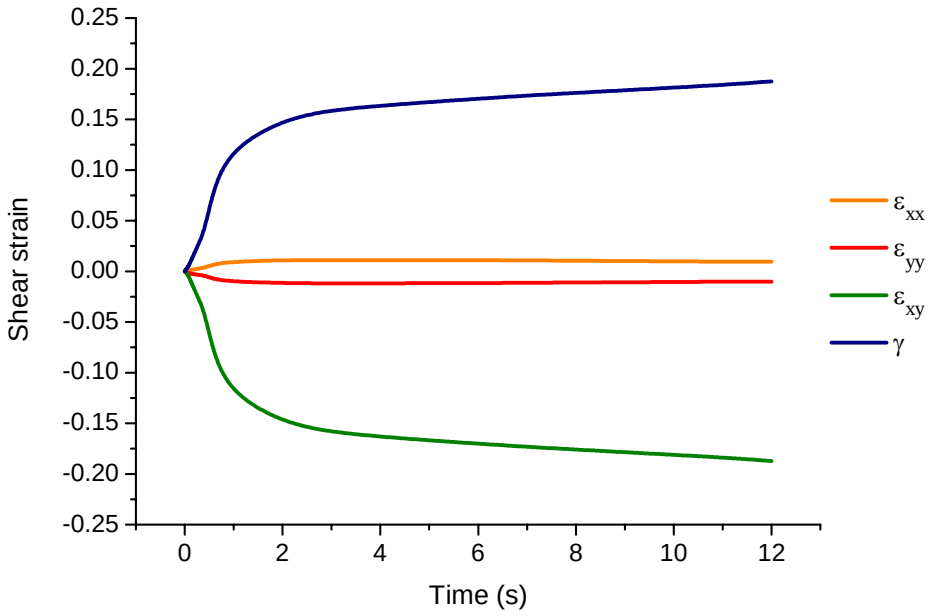

Fig. 4. 24: Time history of the induced shear strain components at depth *h* = 21 cm for Case 3

In the same way as Case 1, Fig. 4.25 shows the time history of the second invariant of the strain tensor for Case 3. Since the shear strength varies along the height, the magnitude of the shear strain at depth h = 21 cm is limited to a value less than 20 % which is closer to the critical value of 21 % computed by Hamada and Wakamatsu (1998). This observation is also in accordance with the time history of the induced lateral ground displacement depicted in Fig. 4.15.

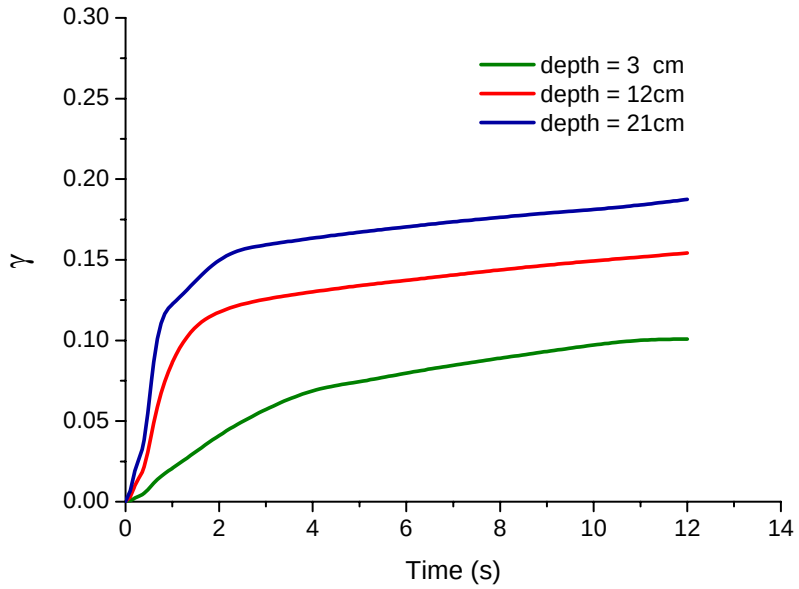

Fig. 4. 25: Time history of the second invariant of shear strain tensor for Case 3

- Spatial distribution of the induced shear strain

The spatial distribution of the second invariant of the strain tensor is illustrated in Fig. 4.26 for Case 3 for four time reference corresponding to t = 1 s, t = 3 s, t = 6 s and t = 12 s respectively.

Fig. 4.26 highlights the distribution of the shear strain where we can see that the soil near the upstream part is subjected to a compression due to the subsidence movement, while the downstream is subjected to a tension due to heaving. The bottom part of the soil box is the most strained region which attains 42 % at t = 12 s. The central part at the top of the soil box is the least stressed region.

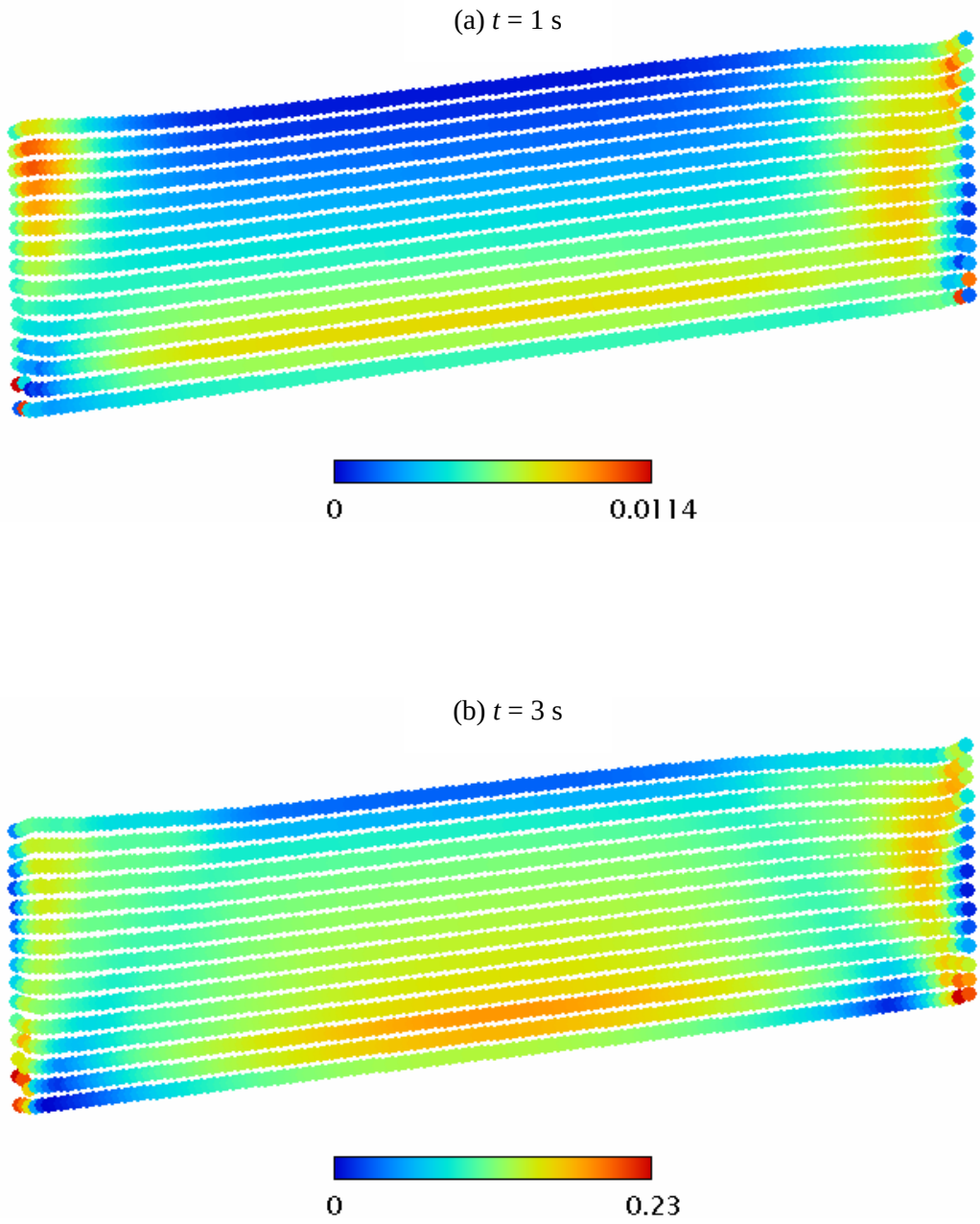

Fig. 4. 26: Spatial distribution of the shear strain at t = 1 s, t = 3 s, t = 6 s and at t = 12 s respectively

(c) t = 6 s

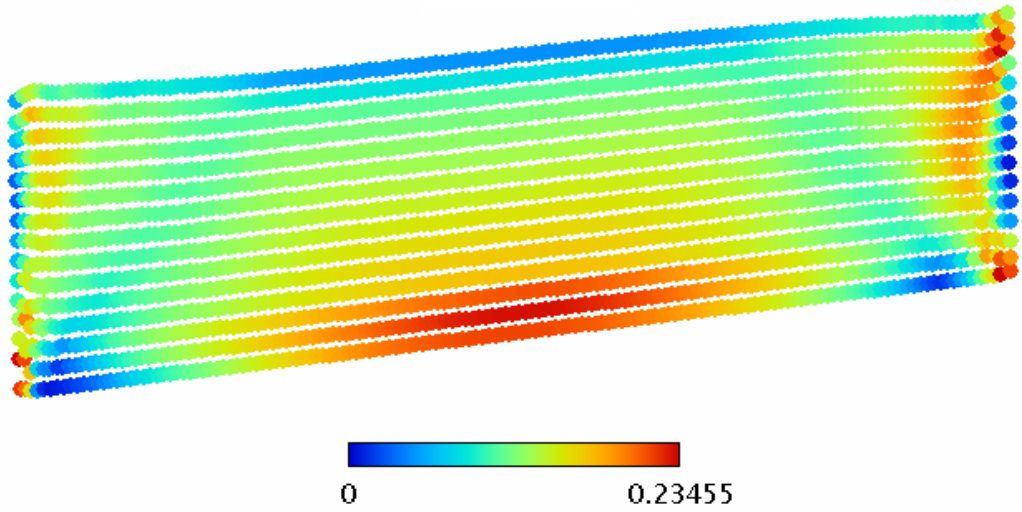

(d) t = 12 s

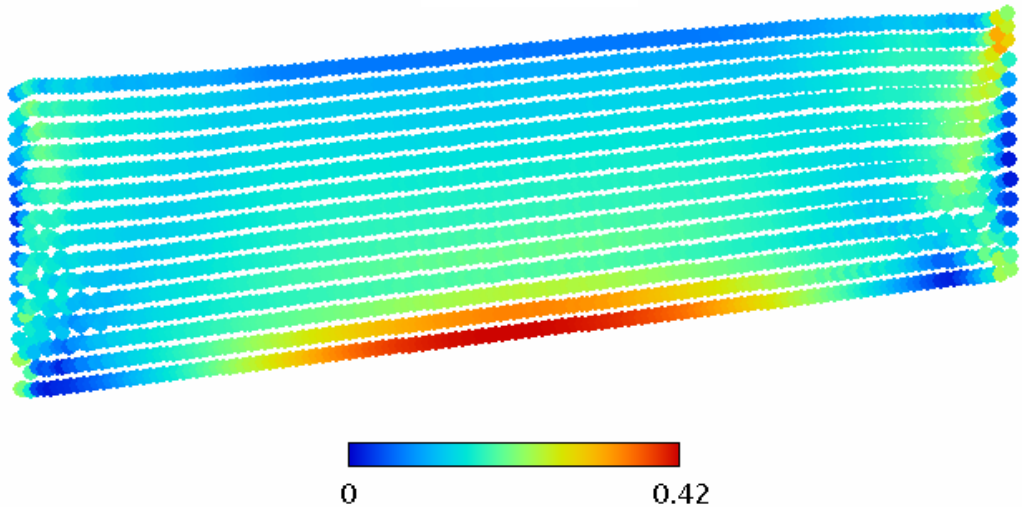

Fig. 4. 26: Spatial distribution of the shear strain at t = 1 s, t = 3 s, t = 6 s and at t = 12 s respectively

- Summary of the simulations results

In the numerical simulation of the liquefaction induced lateral spreading, the SPH representation of the problem succeeded, to a certain extent, in reproducing the results derived during the 1 g shaking table experiment performed by Hamada and Wakamatsu (1998).

Although the shape of the free surface did not fit exactly the observed one, the general trend was well simulated at the upstream and downstream particularly for Case 1. However, the central part did not keep the same inclination as the observed one. In Case 1, the central part experienced a slight rotation with respect to the initial position; in Case 3, the rotation was somehow more prominent. As for the time history of the ground flow velocity, the maximum value for both cases was closer to the observed one. However, the velocities at the bottom part were overestimated. On the other hand, the liquefied soil continued flowing with a magnitude ranging between 1/20 and 1/30 of the maximum value. This result is not consistent with the experiment in which the liquefied soil ceased to flow after the soil recovered its rigidity. Regarding the time history of the induced lateral ground displacements, neither the general observed trend nor the magnitude of the displacement do fit the observed one in Case 1, where the minimum undrained shear strength was kept constant throughout the height. This caused the upper part of the liquefied layer to move as a rigid body over the adjacent lower one. In Case 3, although the general trend of the ground displacement at the beginning was well simulated, the displacement increased continuously. Regarding the induced shear strain rate, the simulated results lay within a comparable range with respect to the value obtained by Hamada and Wakamatsu. The time history of the induced shear strain was also computed at the three respective elevations. However, only Case 3 seems to give closer results to the observed one.

As a conclusion, it appears that the dissipation of the pore water pressure which led the liquefied soil to recover its strength is an important factor to be taken into account to reproduce the observed experimental results in a consistent manner. The next section discusses basic results on the dilatancy properties of the liquefied soil and will introduce a rather simple constitutive model to account for the recovery of the rigidity.

4.3.4 Numerical simulations taking into account the recovery of the rigidity

- Fundamental aspect regarding the post liquefaction shear deformation

The mechanism of post-liquefaction shear deformation in saturated sands was experimentally investigated by Yasuda et al. (1995) using a torsional shear test apparatus. By conducting cyclic torsional shear tests on Toyoura sand under undrained conditions, followed by a monotonic loading when the specimen reached a prescribed value of an excess pore water pressure or a certain value of the severity of the liquefaction, Yasuda et al. have shown that the liquefied sand gradually regains part of its shear strength when it is sheared beyond some threshold shear strain value γ_L. They termed this threshold value "reference strain at resistance transformation". Yasuda et al. have shown that this value is a function of the relative density of the liquefied soil, the confining pressure, the pore pressure ratio as well as the severity of the liquefaction. A liquefied soil having a relative density larger than D_r = 50 % recovers its strength for a threshold value of shear strain less than 20 % if confined with a pressure σ_0' larger than 100 KPa, and with a threshold value less than 10 % if confined with a pressure equals to 25 KPa.

In the same manner, Hamada and Wakamatsu, in their 1g shaking table experiment, have computed a critical strain γ_c beyond which the liquefied soil behaves as a solid body again denoting a regain in its rigidity. The results of their investigation already shown in Table 4.1 are replotted in Fig 4.27.

Using these results to derive a stress-dilatancy model that could be used in the framework of this study seems to be a difficult task, since the SPH approach is introduced in the framework of a fluid dynamics based concept. In this respect, we propose a simple phenomenological model which expresses the behavior of the liquefied soil as understood from the shaking table experiment. This recovery model expresses the relationship between the yield viscosity and the critical shear strain of the liquefied soil by a bilinear curve as seen in Fig. 4.28. The first branch of the curve depicts the yield viscosity coefficient which is constant for values of shear strain smaller than the critical shear strain, while the second branch is a function of the shear strain for values greater than the critical shear strain. Accordingly this

curve is expressed by the following equation:

$$\eta_y = A \quad \text{if} \quad \gamma \le \gamma_c$$
$$\eta_y = (B\gamma + C) \quad \text{if} \quad \gamma > \gamma_c \tag{4.4}$$

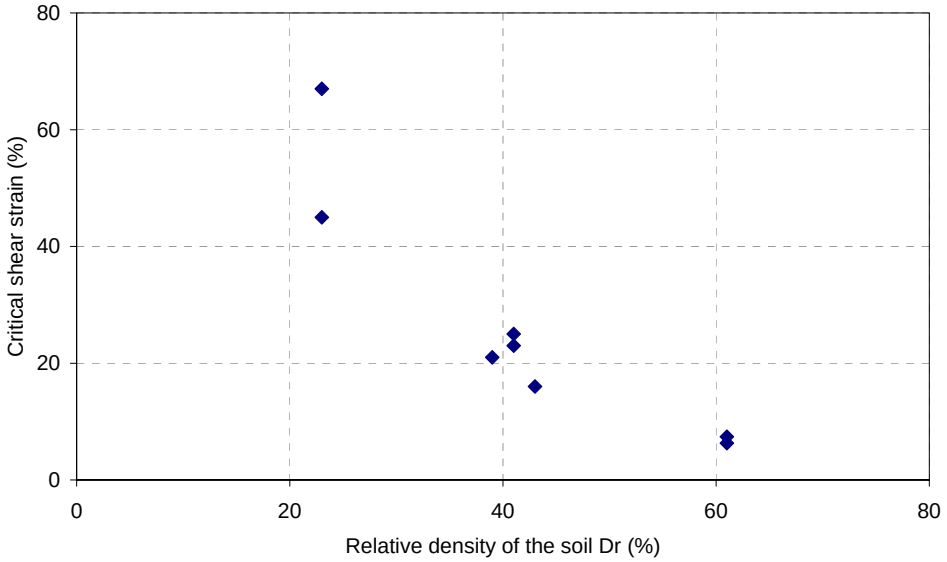

Fig. 4. 27: Relationship between the critical shear strain and the relative density of the soil

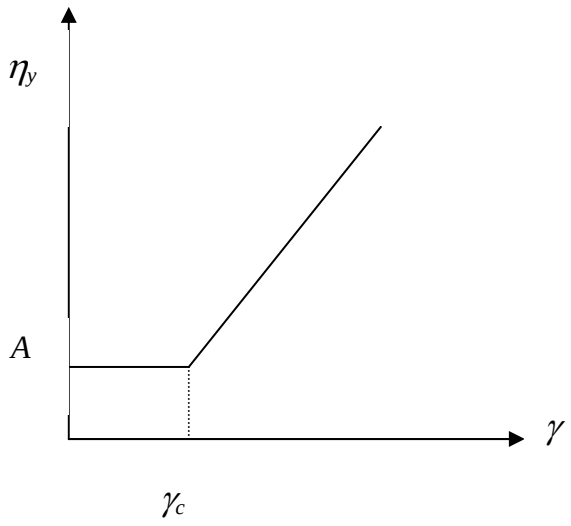

Fig. 4. 28: Proposed constitutive model for the recovery of the rigidity

- Numerical parameters of the recovery model

There are no established rules on how to select the suitable parameters for the constitutive recovery model since the model is not based on a physical test. The parameters were adjusted by successive trials with respect to the obtained results. In this respect, two constitutive models were used to simulate the recovery of the rigidity for the lateral spreading experiment whose parameters are given in Table 4.4 below.

Table 4. 4: Parameters for the constitutive recovery model

	Model 1	Model 2
A (η_y)	0.10	0.10
B	1.1×10^4	1.1×10^5
C	-1.1×10^3	-1.1×10^4

Taking into account the previous results of the induced level of shear strain as well as the obtained results of the critical shear strain given by Hamada and Wakamatsu, the critical shear strain beyond which the soil regains its rigidity is fixed to γ_c = 10 % in the following simulations. Fig. 4.29 illustrates the constitutive models for the simulation of the recovery of rigidity.

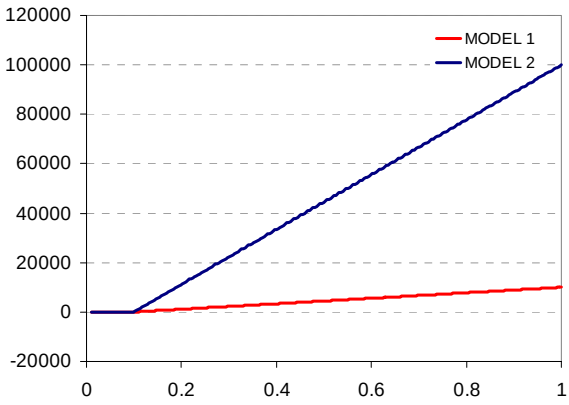

Fig. 4. 29: Constitutive model for the recovery of rigidity

- Free surface shape

Fig.4.30 illustrates the simulated final free surface with and without considering the regain of the rigidity for Case 1 using Model 1. It can be seen that the

simulated free surface is similar to the previously one without considering the recovery of rigidity.

Fig. 4.31 depicts the simulated final free surface for Case 3 using Model 1 and compares it with the free surface obtained when the recovery of rigidity is disregarded. The improvement is observed and the limited flow is well distinguished. In addition, the subsidence in the upstream part and the heaving in the downstream part are reproduced although the final shape is a little different from the observed free surface. The central part keeps the same inclination as the observed one in the downstream part while in the upstream region; the curve has a slight rotation with respect to the initial ground surface.

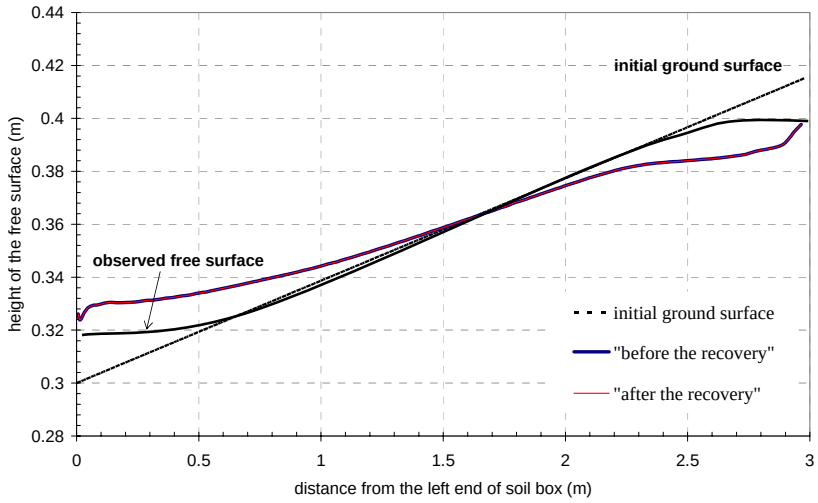

Fig. 4. 30: Simulated free surface before and after the recovery of rigidity for Case 1

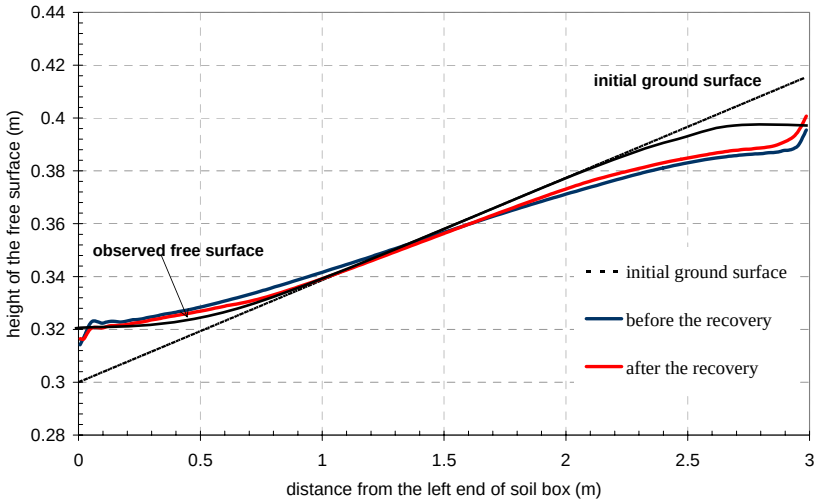

Fig. 4. 31: Simulated free surface before and after the recovery of rigidity for Case 3

- Time history of the ground flow velocity.

The time history of the ground flow velocity for Case 1 obtained with the recovery model 1 is illustrated in Fig.4.32. As it is seen, the curves at the three respective elevations exhibit similar pattern as in Fig. 4.11 particularly in the range 0 - 2 s. The maximum flow velocity is closer to the value assessed by Hamada and Wakamastsu. On the other hand, the velocity at the bottom part is still overestimated, and the soil continues experiencing a moderate flow with reduced velocity of about 1/30 of the maximum velocity. The inability of the constitutive model to reproduce in a consistent manner the recovery of the rigidity may be attributed to the constant value of the minimum undrained shear strength. The obtained results are similar for both Model 1 and Model 2 of the recovery of rigidity. It should be mentioned that only the decrease in the magnitude of the flow velocity after it reaches its peak is expected when simulating the regain of the rigidity with Model 2.

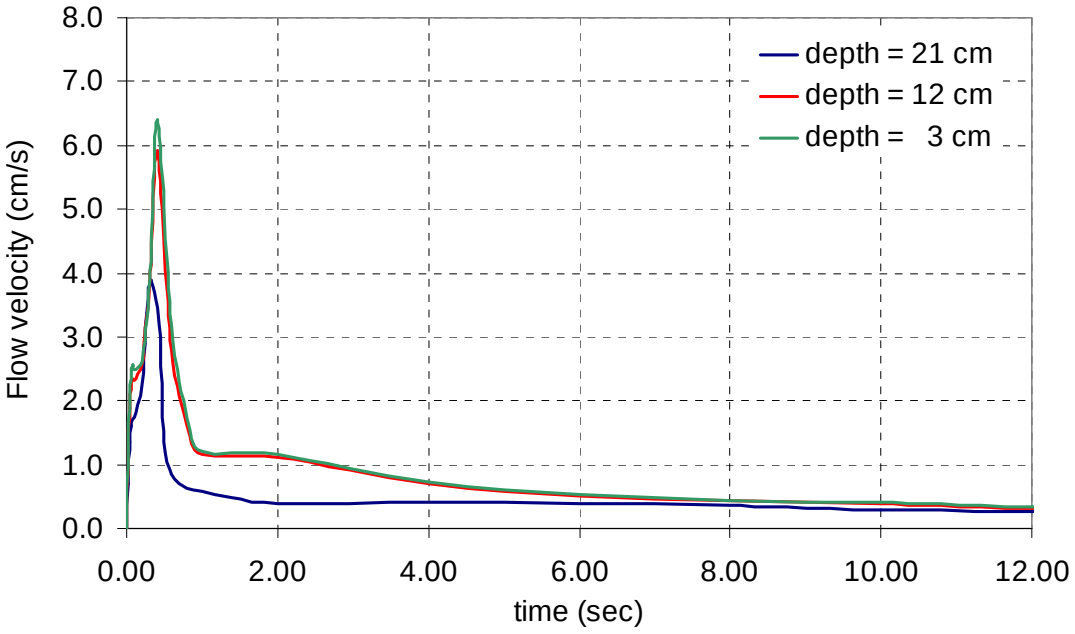

Fig. 4. 32: Time history of the ground flow velocity for Case 1

Similarly, Fig. 4.33 depicts the time history of the ground flow velocity for Case 3 using Model 1 of the recovery of rigidity. The maximum flow velocity is very close to the value of 7 cm/s derived by Hamada and Wakamatsu. Although we still observe the continuous flow after the peak point, the flow velocity decreases sharply

to a value equal to 1/40 of the maximum magnitude. This denotes that the liquefied soil regains slowly its rigidity 4 seconds after the start of the simulation.

Likewise to the previous case, the result obtained for Model 2 was slightly improved without fitting completely the experimental results. Since the minimum undrained shear strength in this particular case depends on the confining pressure and thus on the height at the specific elevation, this discrepancy may be attributed to the wall boundaries. This conclusion is mainly based on the findings obtained from the simulation of a gravity flow of a water-clay mixture presented in Chapter 3, where the flowing mass reaches a freezing profile when the induced shear stress drops below the yield Bingham shear stress.

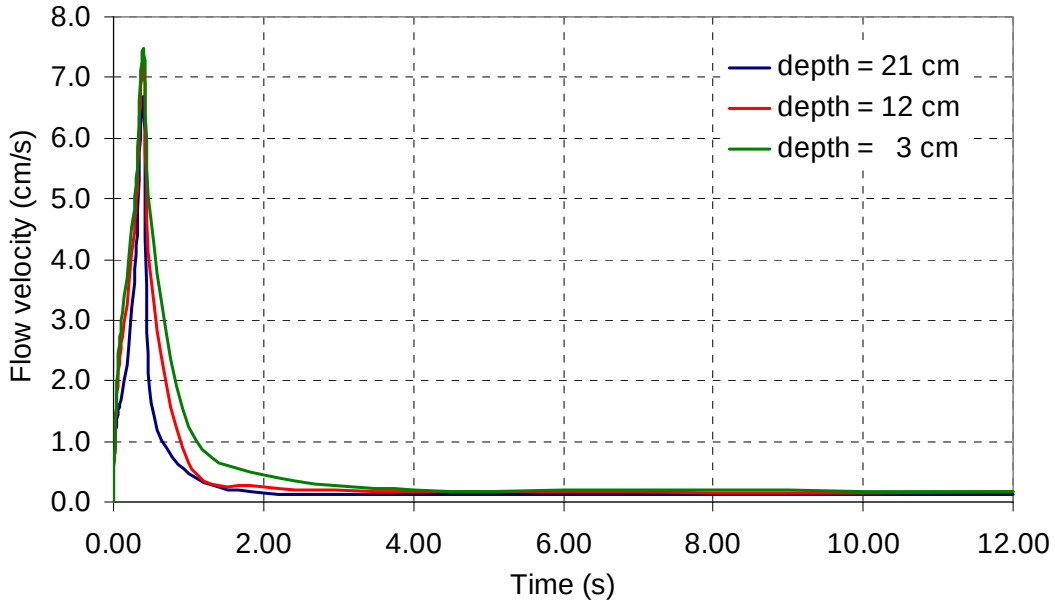

Fig. 4. 33: Time history of the ground flow velocity for Case 3

- Time history of the ground flow displacements

Figures 4.34 and 4.35 show the time history of the ground flow displacement for Case 1 and Case 3 respectively using Model 1 of the recovery of rigidity.

As expected, the constitutive model for Case 1 was unable to reproduce the regain of the rigidity although a slight decrease is observed at depth h = 3 cm and at h = 12 cm. Moreover, the trend of the evolution of the curve is inconsistent with the experimental results, and the liquefied soil still undergoes a high viscosity at small

strain rate. The bottom part of the liquefied layer caused the upper part to move as a rigid body.

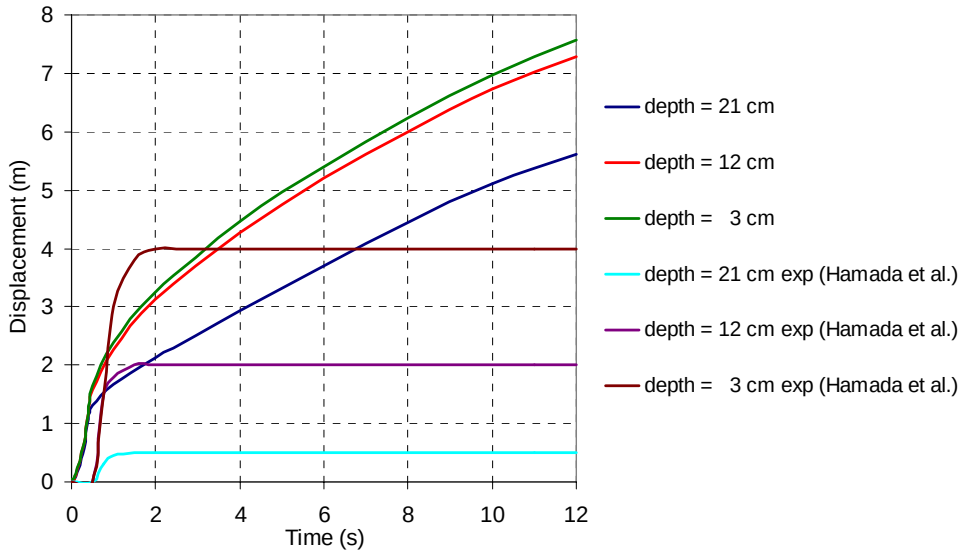

Fig. 4. 34: Time history of the ground flow displacement for Case 1 using Model 1 of the recovery of rigidity

Unlike Case 1, the simulated time history of the flow ground displacement for Case 3 reproduced the trend of the derived experimental results. However, the introduction of the recovery of the rigidity was only able to decrease slightly the induced displacement at the three elevations without reaching a final asymptotic shape as observed during the experiment. Moreover in the bifurcation region, the induced displacement at depth h = 21cm is twice the value observed during the experiment and accordingly incompatible since the related particle is closer to the bottom of the soil box. By plotting the time history of the induced displacement at depth h = 28 cm as depicted in Fig. 4.36, the induced displacement reaches a maximum value of 1cm and keeps a constant value till the end of the simulation. This result is qualitatively consistent with the derived experimental results. Nevertheless, it is quantitatively incoherent and the discrepancy might be attributed to the wall boundary effect, particularly to the nature of the boundary particles simulated with Lennard-Jones potential. This latter exert a driving force on adjacent particles which cause them to experience a large displacement during the early stage

of the simulation. In this respect, more investigations on the boundary wall effect deserve further attention to improve the results with respect to the experimental findings.

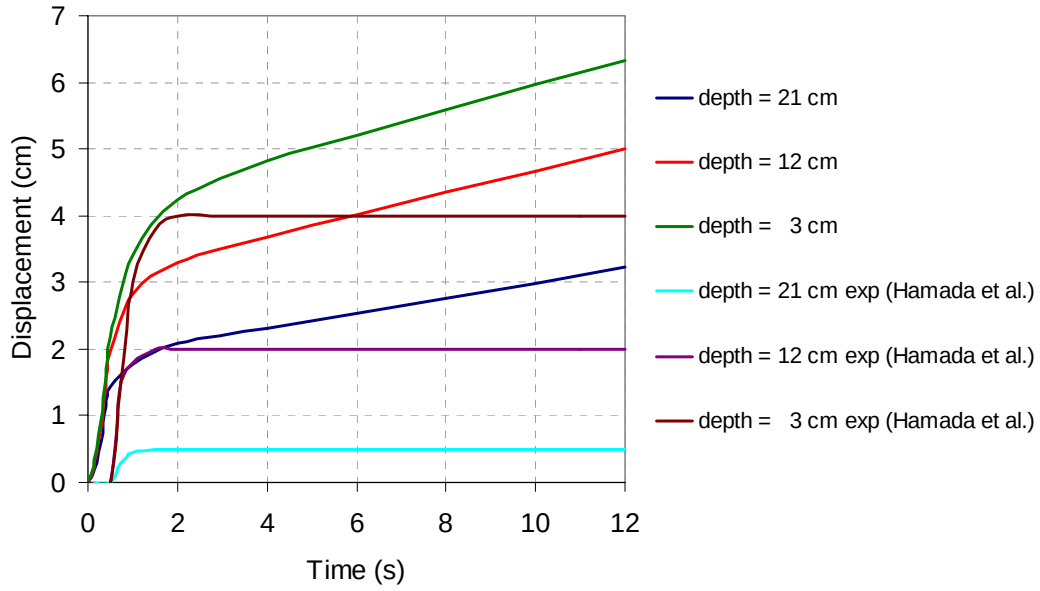

Fig. 4. 35: Time history of the ground flow displacement for Case 3 using Model 1 of the recovery of rigidity

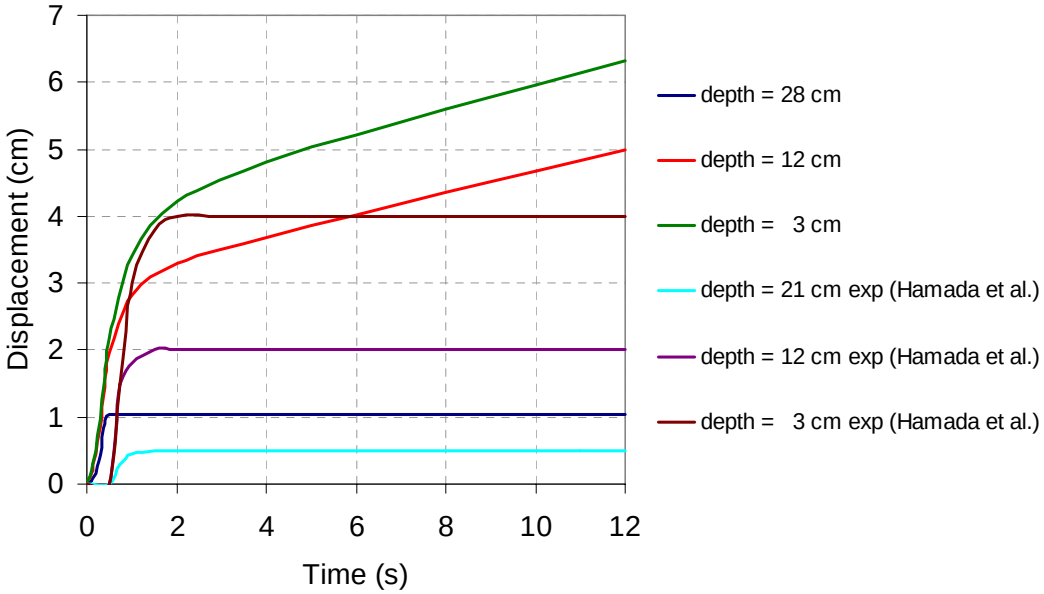

Fig. 4. 36: Time history of the ground flow displacement for Case 3 at depth h = 28 cm using Model 1 of the recovery of rigidity

Similarly, Fig. 4.37 depicts the time history of the flow ground displacements using Model 2 for the recovery of the rigidity where it is observed that the magnitude of the induced displacements slightly decreased without reaching an asymptotic final shape.

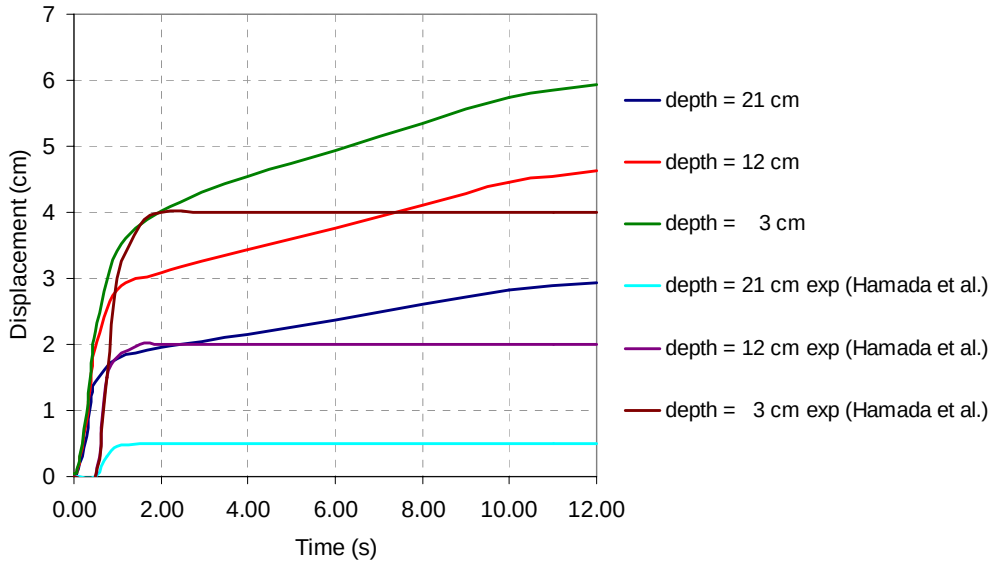

Fig. 4. 37: Time history of the ground flow displacement for Case 3 using Model 2 of the recovery of rigidity

Further numerical simulations using steeper slopes for the recovery model were unable to improve the results, leading sometimes to a numerical instability attributed mainly to the abrupt change of the behavior of the liquefied soil materialized by the bilinear constitutive model. One of the solutions to overcome this instability consists in decreasing the time increment of the numerical simulation. In this respect, a smaller time increment equals to $\Delta t = 10^{-5}$ s was adopted to perform further simulations using both Model 1 and 2 for the recovery of rigidity.

Figures 4.38 and 4.39 illustrate the time history of the flow ground displacement for Case 3 corresponding to Model 1 and Model 2 respectively. From these figures, we can observe that the time evolution of the induced displacement at the three respective elevations tend towards an asymptotic shape at the late stage of the simulation. Moreover, the steeper is the slope of the recovery Model; the smaller is the induced displacement as observed in Fig. 4.39. However, a slight numerical instability still exits as observed at depth h = 12 cm for Model 2. This can be

resolved by adopting a smaller time increment which leads to a large time consuming of the numerical simulations. Finally it should be emphasized that besides the time increment and the gradient of the slope of the bilinear Model, the difference in the final shape is attributed to the dissipation of the pore water pressure which is not accounted for in the bilinear recovery model.

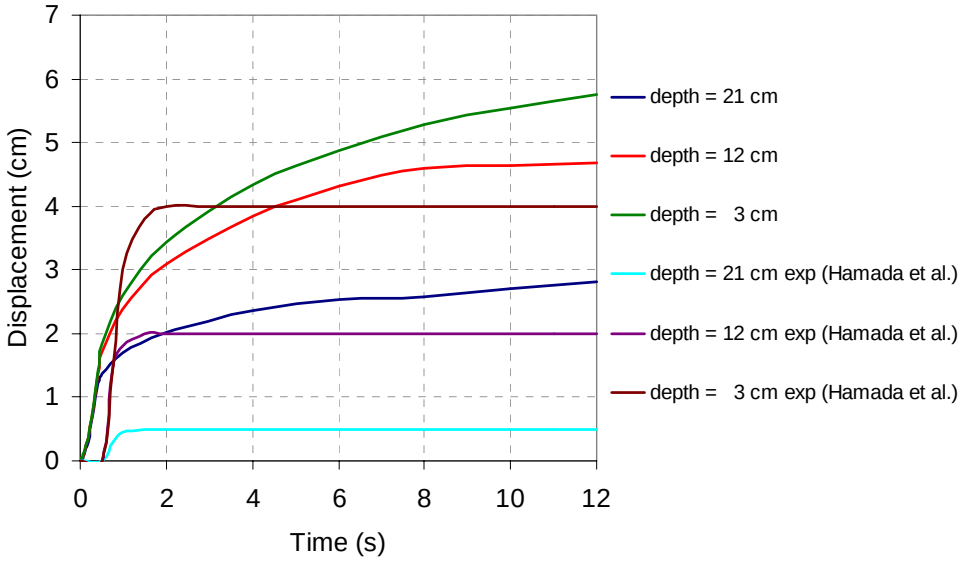

Fig. 4. 38: Time history of the ground flow displacement for Case 3 using Model 1 of the recovery of rigidity corresponding to $\Delta t = 10^{-5}$ s

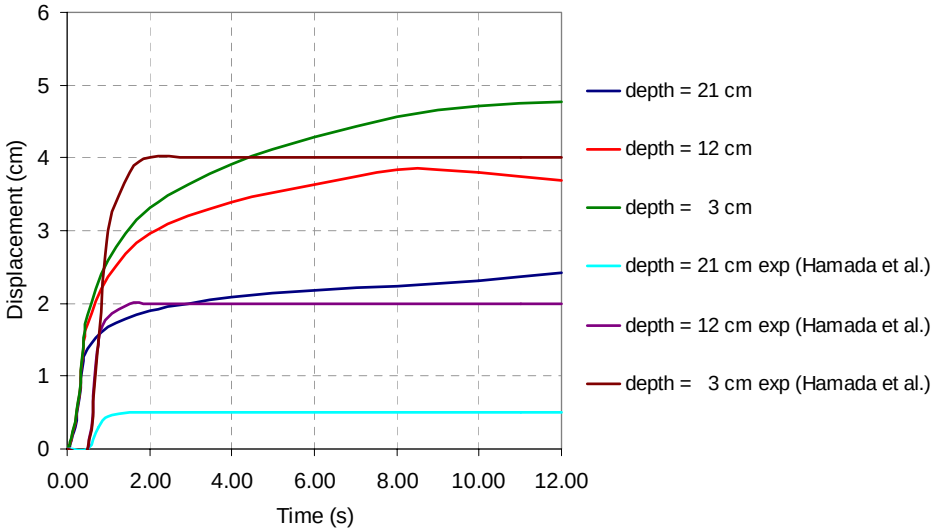

Fig. 4. 39: Time history of the ground flow displacement for Case 3 using Model 2 of the recovery of rigidity corresponding to $\Delta t = 10^{-5}$ s

- Distribution of the ground flow displacements along the height

This section discusses the distribution of the ground flow displacements at the central cross section along the height. The main purpose is to investigate the effect of the recovery model on the distribution of the induced displacement at the central cross section for Case 1 and Case 3.

Fig. 4.40 illustrates the distribution of the ground flow displacement for Case 1 at eight different time steps derived by using Model 1 of the recovery of rigidity. This distribution resembles to a curve which looks as one fourth of a sinusoidal wave. This results is consistent at the beginning of the simulation up to t = 1 s. If the soil has regained its rigidity, the distribution should have been a triangular one. However, the ¼ sinusoidal distribution of the ground flow displacement suggests that the upper layers of the liquefied soil move as a rigid body over the lower liquefied layers. This result is in accordance with the previous conclusions related to the time history of the flow velocity as well as the ground flow displacement for Case 1.

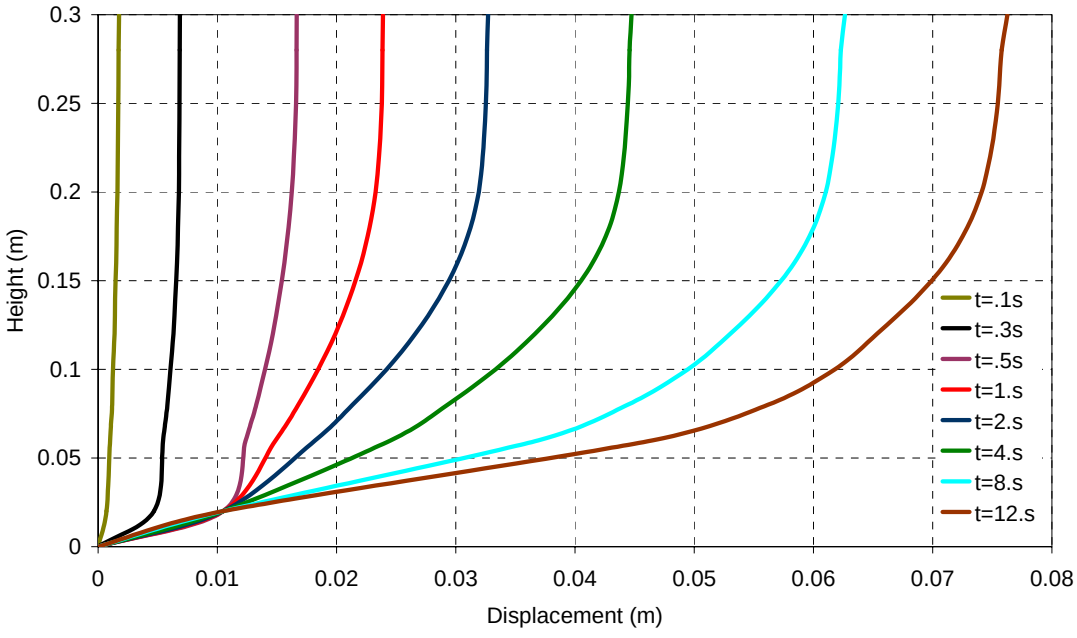

Fig. 4. 40: Distribution of the ground flow displacement at the central cross section at eight time reference

Fig. 4.41 depicts the same distribution of the ground flow displacement for Case 3 derived by using Model 1 of the recovery of rigidity. Similarly to Case 1, the distribution of the displacement for time span less than t = 2 s looks like a ¼ of a sinusoidal wave. However, as the soil regains its rigidity, the sinusoidal distribution moves towards a triangular one. This suggests that each liquefied layer moves separately without exhibiting a rigid body behavior. Finally, the simulated trend is consistent with the physical test results derived by Hamada and Wakamatsu, and consistent with the simulated time history of the ground flow displacement.

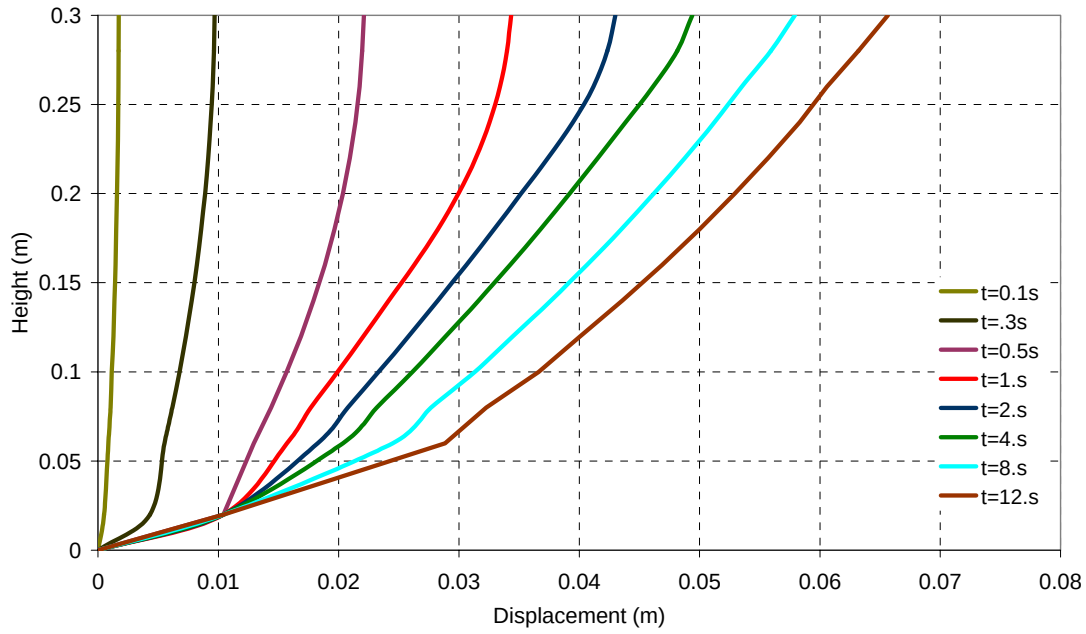

Fig. 4. 41: Distribution of the ground flow displacement at the central cross section at eight time reference

- Maximum ground displacements

The maximum ground displacement at three elevations computed at three distinct locations was also simulated and compared with available results given by Hamada and Wakamatsu for Case 3. In fact, the liquefied soil in this simulated case seems to have regained its rigidity with a level smaller than the observed one.

Fig. 4.42 shows the distribution of the maximum ground displacement at three elevations at distances equals to 0.5 m, 1.5 m and 2.5 from the left side of the soil box obtained using Model 1 of the recovery of rigidity.

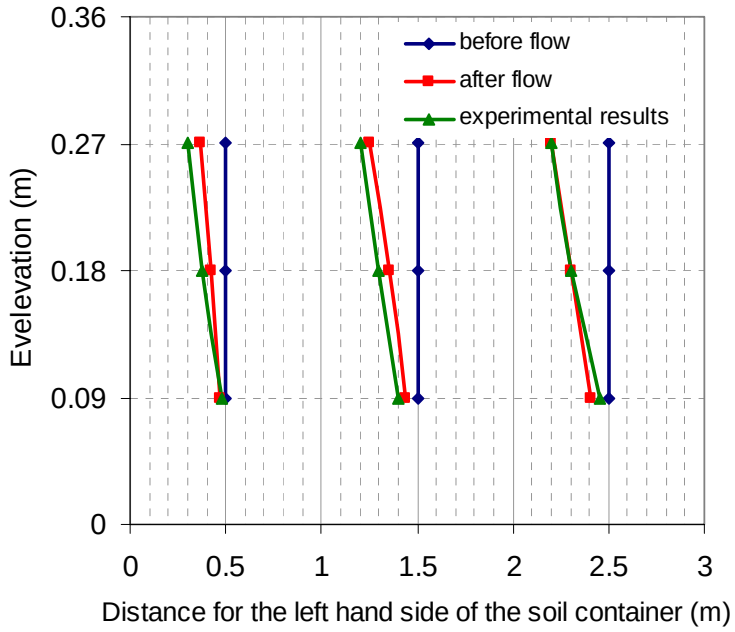

Fig. 4. 42: Maximum ground displacement

Fig. 4.42 shows that the simulated maximum ground displacements are consistent with the experimental results. At a distance of 2.5 m from the left hand side, the simulated maximum ground displacement is well reproduced at the three respective elevations corresponding to depth h = 3 cm, h = 12 cm and h = 21 cm. However in the central part and at a position equals to 0.5 m from the left side of the soil container, the simulated ground displacements are smaller than the experimental ones. This expresses the fact, that the liquefied soil recovered its rigidity.

- Time history of the induced shear strain rate

The time history of the induced shear strain rate was also assessed for the simulated Case 1 and Case 3 using Model 1 of the recovery of rigidity. The results were compared with the experimental findings given in Table 4.1.

Figures 4.43 and 4.44 illustrate the relationship between the viscosity and the induced shear strain rate for Case 1 and Case 3 respectively. The level of the induced shear strain rate in case 1 is almost similar to the case where the recovery of the rigidity is not accounted for. However for Case 3, the simulated induced shear strain

rates are found in the small strain rate region compared with the values given by Hamada and Wakamatsu.

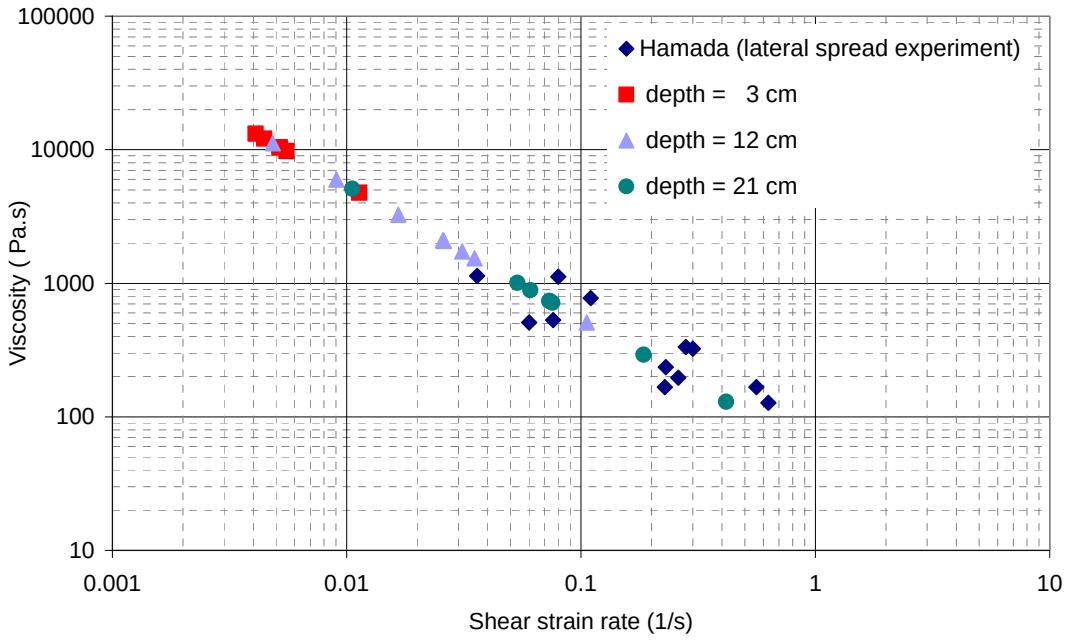

Fig. 4. 43: Relationship between the equivalent viscosity and the induced shear strain rate for Case 1

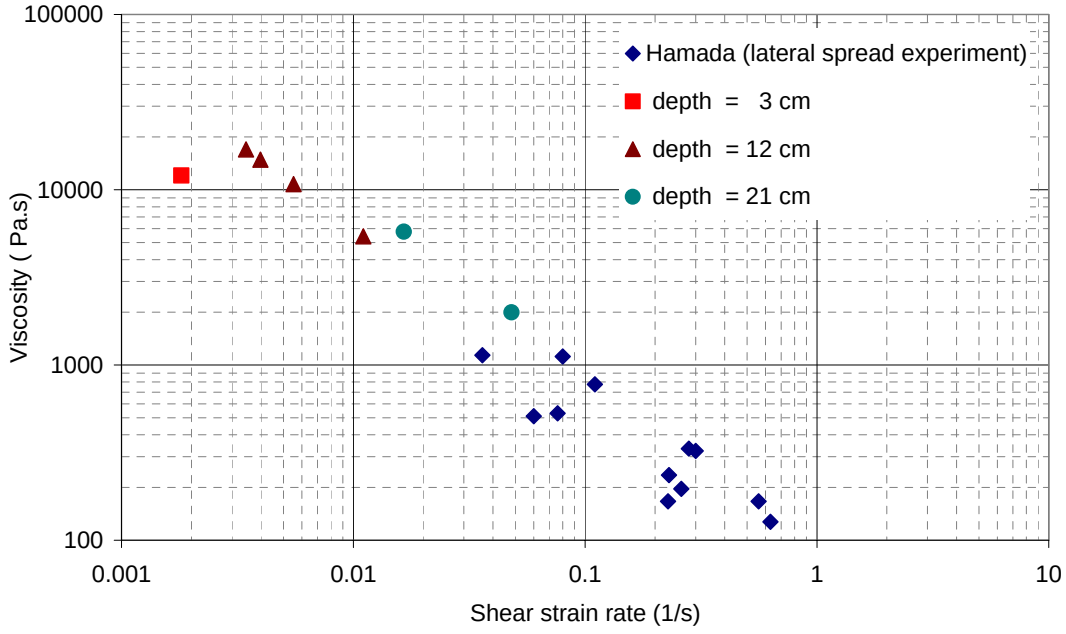

Fig. 4. 44: Relationship between the equivalent viscosity and the induced shear strain rate for Case 3

- Time history of the induced shear strain

The time history of the induced shear strain has been derived for Case 1 and Case 3. However unlike the previous simulations highlighted in section **4.3.3**, only the time history of the second invariant of the strain tensor will be discussed and compared with the previous results. Fig. 4.45 depicts the time history of the second invariant of the strain tensor derived for Case 1 at three different elevations using Model 1 of the recovery of rigidity. From this figure, we can observe that only the bottom part of liquefied soil regained its rigidity, while the middle part and the upper part were insensitive since the maximum shear strain distribution was below the critical shear strain γ_c.

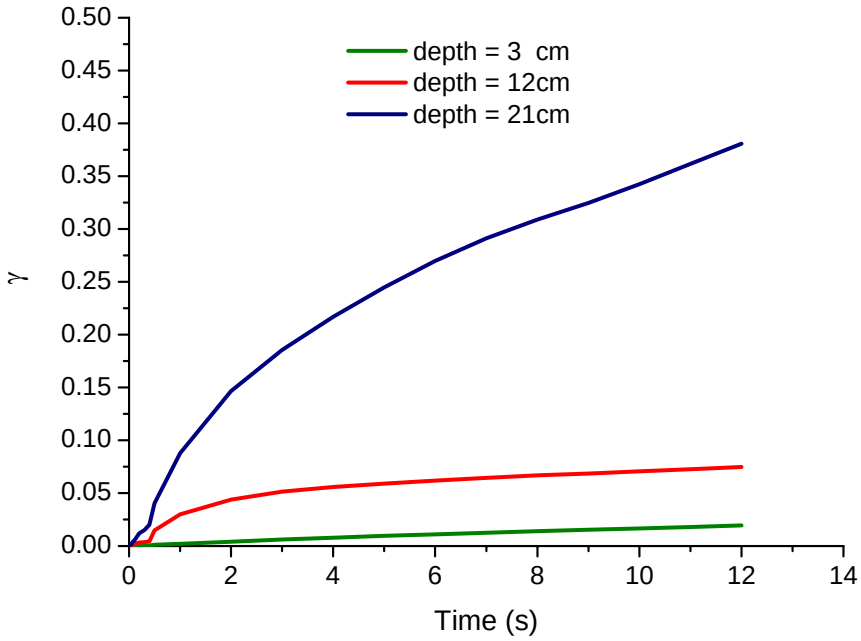

Fig. 4. 45: Time history of the second invariant of the deviatoric strain tensor for Case 1

Fig. 4.46 shows the time history of the second invariant of the strain tensor computed at depth h = 21 cm by considering and disregarding the recovery of the rigidity.

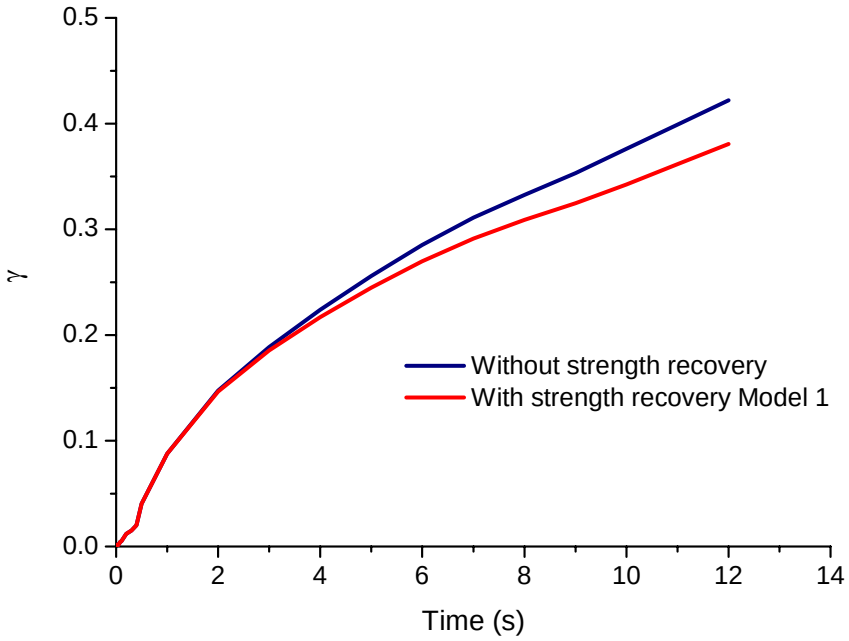

Fig. 4. 46: Time history of the second invariant of the strain tensor for Case 1 at depth h = 21 cm

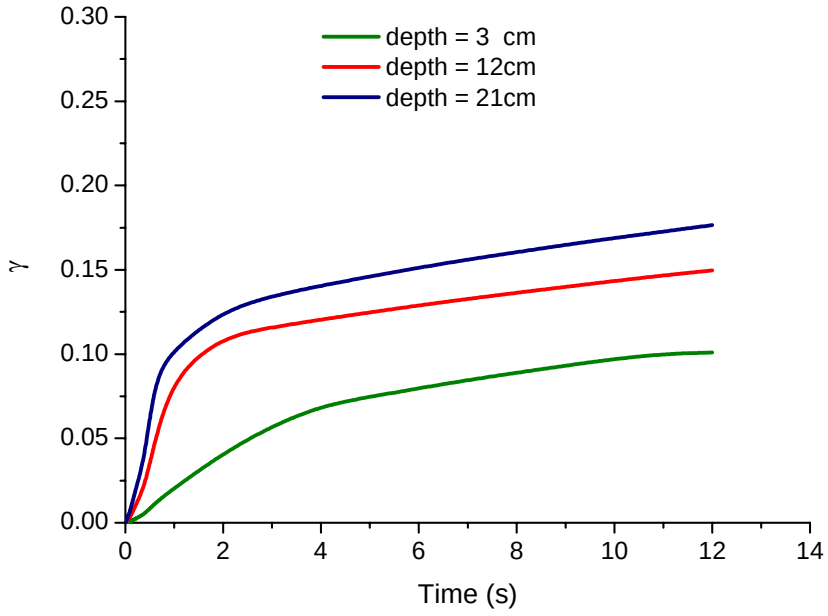

Fig. 4. 47: Time history of the second invariant of the strain tensor for Case 3

Likewise Case 1, the time history of the second invariant of the strain tensor for Case 3 using Model 1 of the recovery of rigidity is shown in Fig. 4.47. In this case, the liquefied soil regains its rigidity at the bottom as well as the middle part, since the induced shear strain is greater than the critical shear strain. Fig. 4.48 illustrates the time history of the second invariant of the strain at depth h = 21 cm with and without considering the recovery of the rigidity.

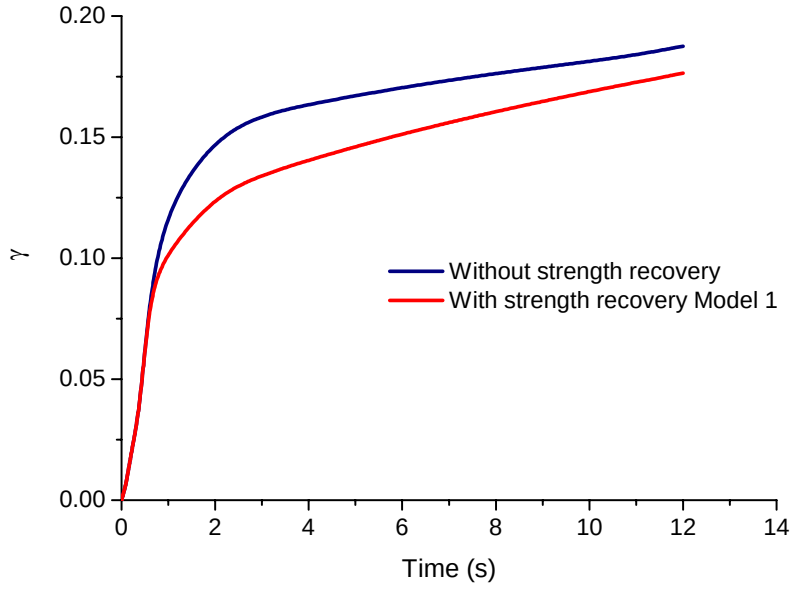

Fig. 4. 48: Time history of the second invariant of the strain tensor for Case 3 at depth h = 21 cm

- Summary of the simulations results taking into account the recovery of the rigidity

In this section a simple phenomenological constitutive model was introduced to account for the recovery of the rigidity. Since this study uses the concept of fluid dynamics to simulate the liquefaction induced lateral ground displacement, it was rather difficult to derive a dilatancy stress model based on the experimental results conducted on the post-liquefaction shear deformation, like those obtained by Yasuda et al. In this respect, we introduced a bilinear model based on the dual behavior of the liquefied soil as introduced in Chapter 2.

However, there are no specific rules on how to select the parameters related to this model as it is not based on a physical testing. The appropriate parameters were selected by successive trials using the derived experimental results.

Although the shape of the free surface in Case 1 did not experience any improvement after introducing the recovery constitutive model, this modification was able to reproduce the general trend in Case 3. Nevertheless, the central part of the free surface kept similar inclination as the initial surface in the downstream region only. As for the time history of the ground flow velocity, the maximum value for both cases became closer to the observed one. However, the liquefied soil continues flowing with a small velocity even after it recovers its rigidity. Since this tendency was even observed in Case 3 for which the minimum undrained shear strength is function of the confining pressure, and having in mind the results of the gravity flow of the water-clay mixture, it was concluded that this discrepancy may be attributed to the boundary wall effect. Regarding the time history of the induced lateral ground displacements, similar trend was observed for Case 1 when the recovery of the rigidity was not taken into account. However, a consistent trend was observed for Case 3 which was able to overcome the high viscosity at small shear strain rate although the asymptotic shape is not reproduced for both recovery models. In this respect, additional simulations by adopting a smaller time increment were conducted. It was observed that the steeper is the slope of the bilinear model; the smaller are the induced displacements though the asymptotic shape is only observed at the final stage of the numerical simulation. This difference with respect to the experimental findings is related besides the wall effect and the time increment, to the dissipation of the pore water pressure which is not taken into account in the bilinear recovery model. The distribution of the ground displacement at the central cross section along the height was also derived for eight time intervals. A consistent distribution of the displacement along the height was simulated in Case 3, where the trend changes from ¼ of a sinusoidal wave to a triangular one when the liquefied soil regains its rigidity. Moreover, the maximum ground displacement at three different locations at three specific elevations was estimated. It was found that the maximum values of ground displacement fit the observed ones with a good accuracy at a distance equals to 2.5 m from the left side of the soil box.

4.4 Numerical simulation of the flow velocity with respect to the gradient of the ground surface and liquefied layer thickness

Once the mechanism of the liquefaction induced lateral ground displacement after the cease of the earthquake has been investigated and the nature of the liquefied soil has been clarified, Hamada and Wakamatsu (1998) used the same experimental setup depicted in Fig. 4.5 to perform several other experiments of a sloped ground model. In this respect, different layer thickness ranging between 15 and 38 cm and surface gradient varying between 1 and 5% were prepared in the same soil box. Hamada and Wakamatsu showed that the ground flow velocity is proportional to the square root of the layer thickness. By assuming a flow velocity distribution as ¼ of a sinusoidal wave, they proposed a relationship for the maximum velocity at the ground surface with respect to the soil layer thickness, ground slope and viscosity of the liquefied layer.

In this section, we do not intend to simulate this experiment but rather use the same experimental setup to investigate the relationship between the maximum flow velocity, the liquefied layer thickness and the gradient of the ground surface.

For this aim, we conducted numerical simulations using liquefied layer thickness ranging between 16 cm and 50 cm with a ground gradient slope of 3% and 5%. We attempt to focus on how the maximum velocity and the required time to reach this maximum do very with the layer thickness and the gradient of ground surface.

4.4.1 Numerical setup

We performed 10 simulation cases in total, considering a liquefied ground model of thickness varying between 16 cm and 50 cm with a ground slope of 3% and 5% inside a soil box of a 3m length.

The Bingham model is taken as the constitutive law for the liquefied ground considering a yield viscosity η of 1 Pa·s. The recovery of the rigidity was not taken into account since our main concern is related to the occurrence time of the maximum velocity which takes place much more earlier before the soil regains its rigidity.

The minimum undrained shear strength was assessed for each case at the middle of the soil layer. Fig. 4.49 shows the relationship between the surface gradient slope and the minimum undrained shear strength for each soil layer thickness.

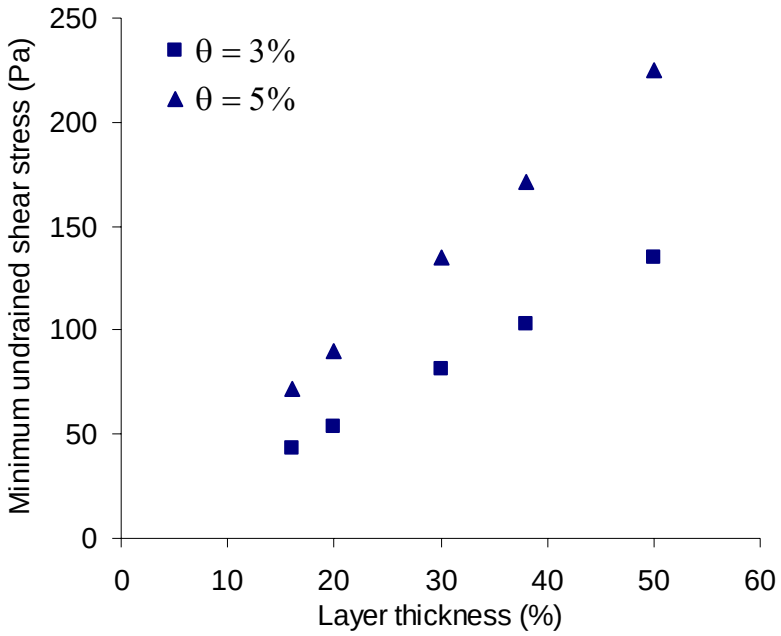

Fig. 4. 49: Relationship between the minimum undrained shear strength with respect to the liquefied layer thickness

4.4.2 Simulations results

Figures 4.50 and 4.51 show the time history of the ground flow velocity for each liquefied layer thickness for a ground slope θ = 3 % and θ = 5 % respectively. As expected, larger flow velocities occur for thicker layers with the steeper slope. By plotting the relationship between the ground flow velocities and the liquefied layer thickness for each ground gradient slope, we showed, as stated by Hamada and Wakamatsu (1998), that the flow velocity is a function of the square root of the liquefied layer thickness as illustrated in Fig. 4.52.

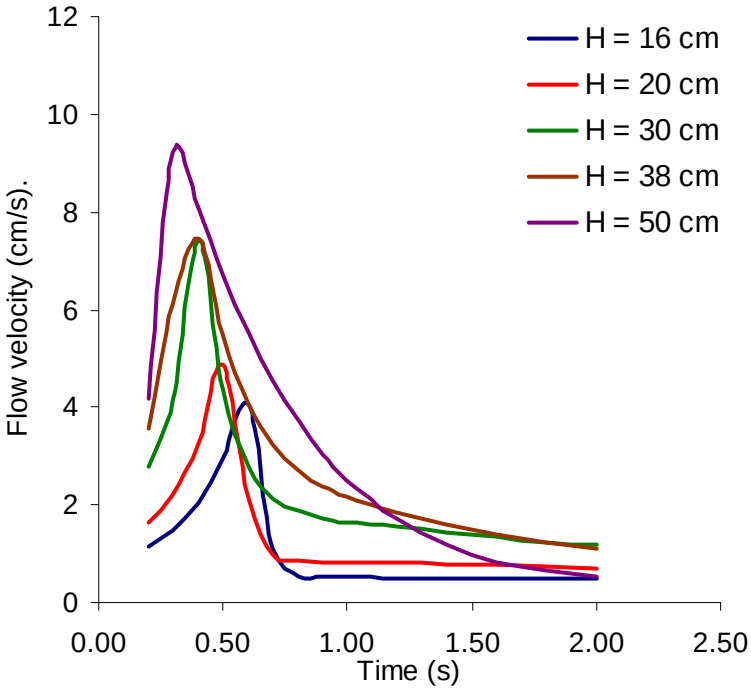

Fig. 4. 50: Time history of the ground flow velocity for slope gradient $\theta = 3$ %

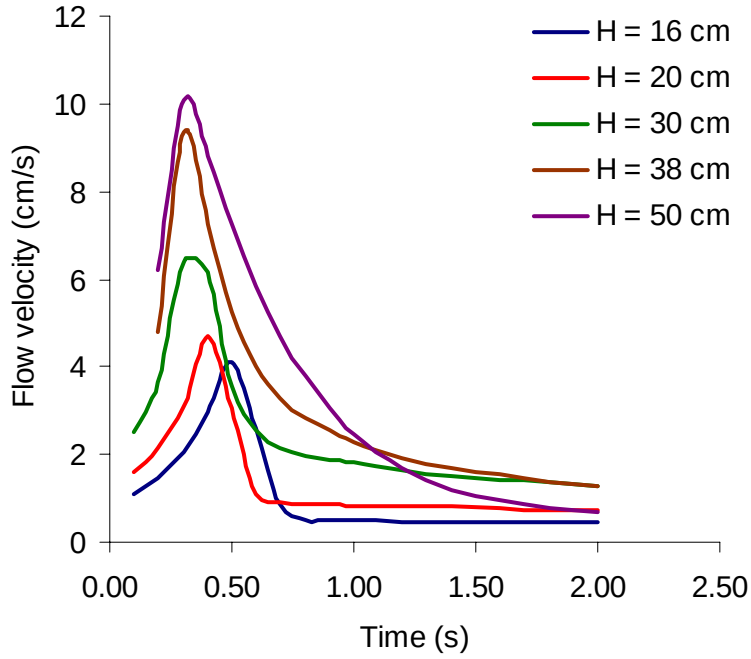

Fig. 4. 51: Time history of the ground flow velocity for slope gradient $\theta = 5$ %

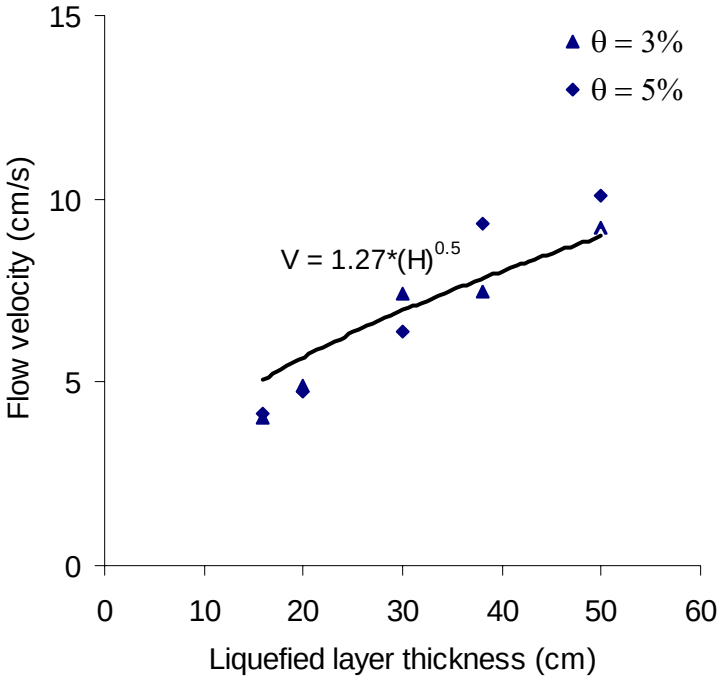

Fig. 4. 52: Relationship between the ground flow velocities versus the liquefied layer thickness

A regression analysis to express the relationship and find the best estimate between the flow velocities V (cm/s) and the liquefied layer thickness H (cm) was performed and the result is given by Eq. (4.5) as follow:

$$V = 1.27\sqrt{H} \qquad (4.5)$$

By analyzing the results shown in figures 4.50 and 4.51, we observe that the required time for the ground flow velocity to reach its maximum is a function of the liquefied layer thickness and the ground gradient slope as depicted in Fig. 4.53. A similar regression analysis enables us to find the best estimation of the required time T (s) for the ground flow velocity to reach its maximum value as a function of the liquefied layer thickness H (cm) and the ground gradient slope. This relationship is given by Eq. (4.6) and Eq. (4.7) for a ground gradient slope θ = 3 % and θ = 5 % respectively.

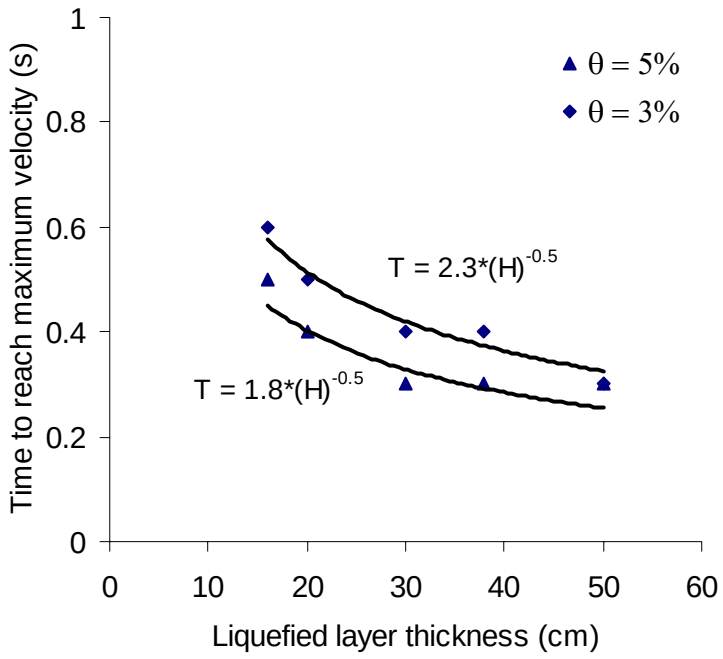

Fig. 4. 53: Required time to reach the maximum ground flow velocities as a function of the liquefied layer thickness

$$T = 1.8\sqrt{H} \quad (4.6)$$

$$T = 2.3\sqrt{H} \quad (4.7)$$

Fig. 4.53 states that the thicker is the liquefied layer, the shorter is the time required to reach the maximum flow. Conversely, the steeper is the ground slope; the larger is the required time to reach the maximum flow for the same liquefied layer thickness.

- Summary of the simulations results

In this section we conducted numerical simulations to investigate the relationship between the flow velocity, the liquefied layer thickness and the ground slope gradient by using the experimental setup developed by Hamada and Wakamatsu. The results showed that the both the ground flow velocity and the time required to reach the maximum velocity is the function of the square root of the liquefied layer.

4.5 Numerical simulation of the liquefied flow around a model pile

This section discusses the ability of the SPH method to simulate the flow of a liquefied soil around a model by using the experimental setup developed by Hamada et al (1992). It is worth to mention that this problem represents a fundamental aspect in the assessment of the drag force applied by the liquefied flow and hence in the design of piles subjected to the exerted forces due to lateral spreading.

In this respect, Hamada et al. conducted a 1g shaking table experiment to assess the effect of the liquefaction induced ground displacement on an acrylic model pile. A model ground 3 m long, 1 m wide and 25 to 31 cm deep was constructed inside a soil box with a surface gradient of 2 %. The model foundation pile of acrylic resin, 28 cm in length and 22 mm in diameter, was placed at the center of the soil box after fixing its lower part. The experimental setup is depicted in Fig. 4.54. The liquefaction was induced by subjecting the soil box to sinusoidal waves with a frequency of 5 Hz in the shorter direction for 10 seconds and thus the soil started moving due to the gradient surface inclination without any effect of the inertial forces.

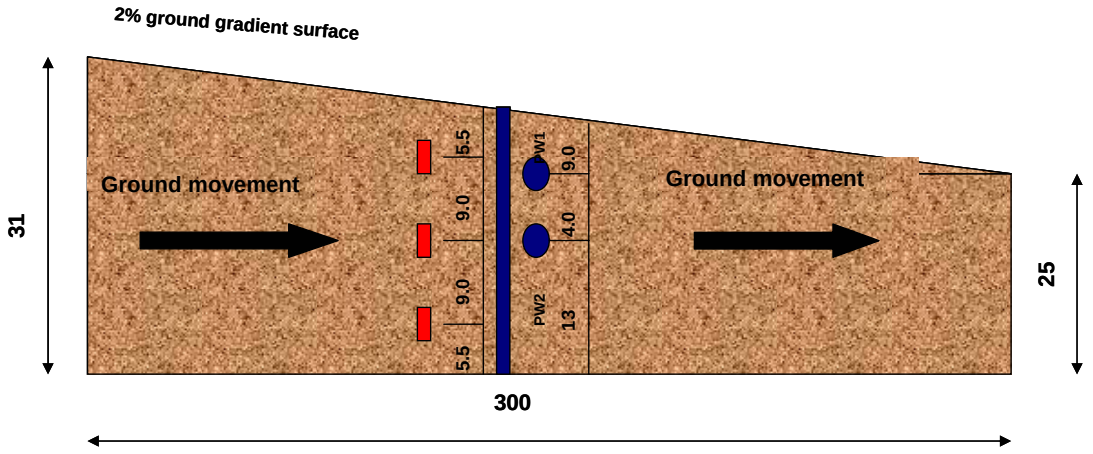

Fig. 4. 54: Experimental setup for flow around a model pile
(after Hamada et al., 1992)

4.5.1 Numerical setup

The experimental setup developed by Hamada et al. is used to simulate the flow induced by the liquefied soil around the model pile by considering and disregarding the recovery of the rigidity. Since the SPH method has not been extended in the present study to account for solid problem, our interest is limited to investigate the distribution of the flow velocity, as well as the strain and stress field around the pile. In this respect, the problem resumes to a 2D representation of the induced flow around the pile at the top of the free surface. For a better efficiency of the SPH method, the problem is modeled using periodic boundaries in the direction of the flow by choosing a representative volume around the pile. For this purpose, a model of square lattice of 1 m × 1 m is taken around the model pile as illustrated in Fig. 4.55.

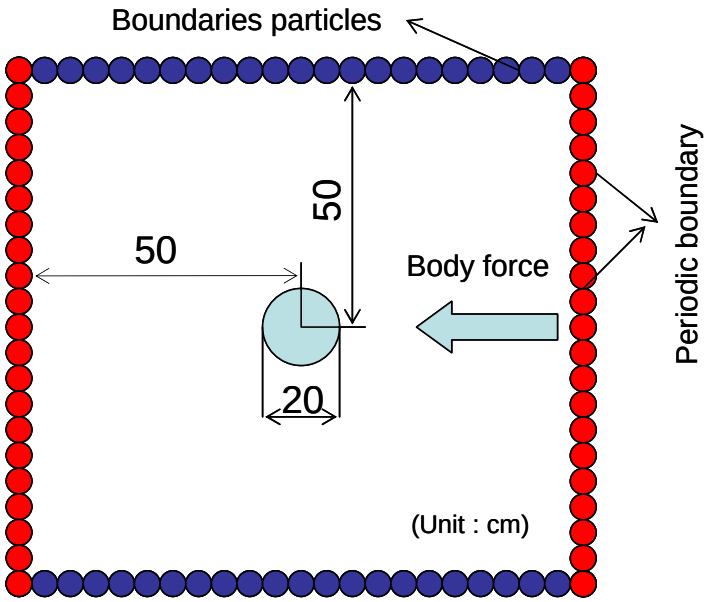

Fig. 4. 55: Numerical setup

In Total, 2500 particles equally spanning the channel with an initial spacing of 1 cm were used to represent the domain. These particles were subjected to a body force equivalent to $F = g\sin(\theta)$ where $\theta = 2$ %. The model pile was represented by a set of particles exerting a Lennard-Jones potential on surroundings medium.

Table 4.5 summarizes the numerical parameters used in the simulations.

Table 4. 5: Numerical parameters

Model dimensions	1 x 1m
Number of particles	50 x 50
Initial spacing	0.01 m
Density of particles	1800 kg/m^3
Yield viscosity	0.1 Pa·s
Minimum shear strength τ_{min}	10 Pa
Time increment	10^{-4}s
Sound speed	0.01 m/s
ε (XSPH)	0.3

4.5.2 Simulation results

To investigate the nature of the liquefied flow around the model pile, two sets of numerical simulations were performed by disregarding and considering the recovery of the rigidity. Since the model is not subjected to any confined boundaries in the direction of the flow, the simulations present a good means to check the assumption so far made on the limitation of the bilinear constitutive model to represent the recovery of the rigidity.

1. Simulation without recovery of rigidity

The simulation was conducted during a time span of 12 s. The flow velocity profile in the longitudinal and transversal direction along three paths as depicted in Fig. 4.56 is illustrated at t = 0.5 s and t = 12 s in figures 4.57, 4.58 and 4.59 respectively. The flow velocity profile along paths A, B and C is only illustrated at t = 0.5 s as the flow acts toward the longitudinal direction. The wraparound effect due to the periodic boundaries as well as the symmetry of the flow is well depicted.

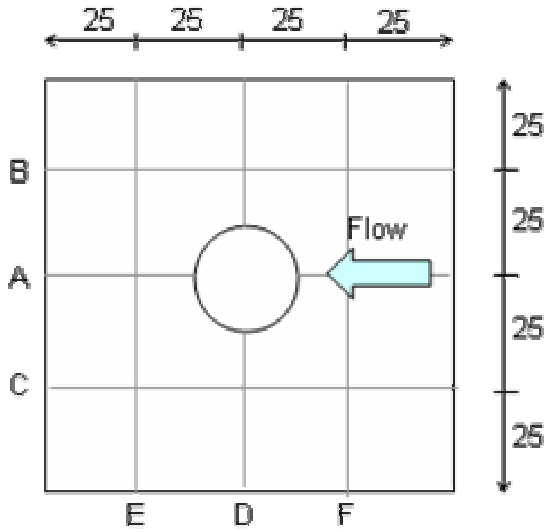

Fig. 4. 56: Schematic representation of the paths along which the flow velocity profile is assessed

Fig. 4.57 shows the velocity profile along path A, B and C at time t = 0.5 s. The maximum flow velocity is depicted at the center of the channel along path A and is equals to 0.012 m/s. Starting from X = 1 m, the velocity decreases as the flow approaches the pile and reaches zero at the contact boundaries. It starts increasing again behind the pile and gains its maximum value at X = 0 m. The flow velocity exhibits similar profile and intensity along path B and C due to the symmetry of the flow along the channel.

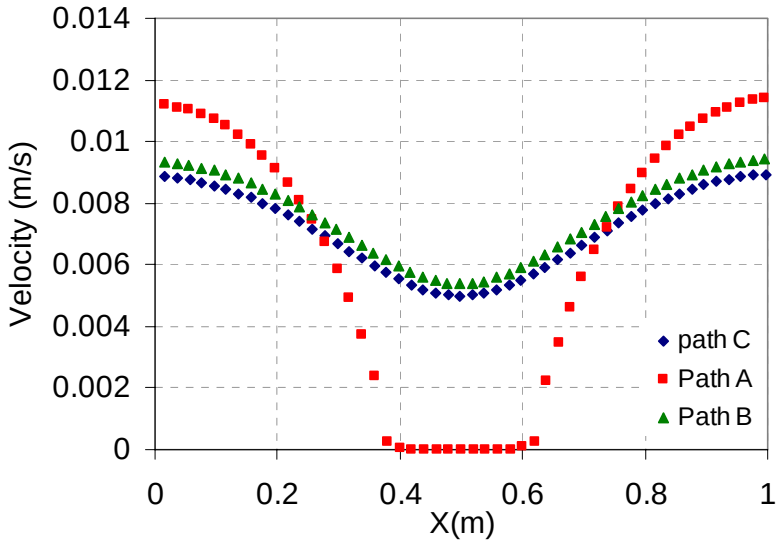

Fig. 4. 57: Flow velocity profile along paths A, B and C at time t = 0.5 s

Fig. 4.58 illustrates the flow velocity profile along path E, F and D at t = 0.5 s. The maximum velocity is observed along path E and F and describes a flow which did not reach the stationary regime yet. Along path D, the velocity profile exhibits a symmetric shape with two peaks along the channel. It became null when the flow approaches the model pile.

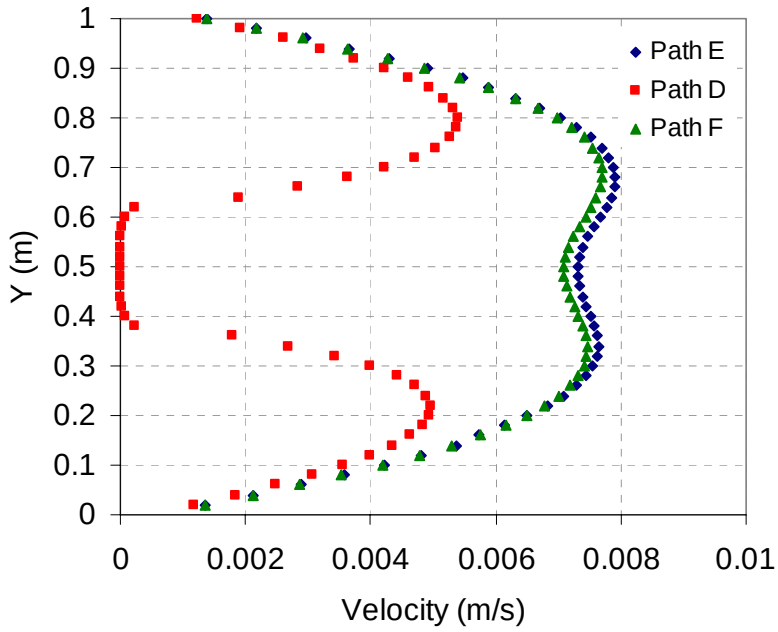

Fig. 4. 58: Flow velocity profile along paths E, F and D at time t = 0.5 s

Similarly, Fig. 4.59 depicts the flow velocity profile along path E, F and D at t = 12 s. The flow along path E attains the stationary regime with a magnitude equals to 0.085 m/s. Along path D and F, the flow velocity profile is identical to t = 0.5 s with a reduced magnitude along path F due to the appearance of the yield/ unyield region.

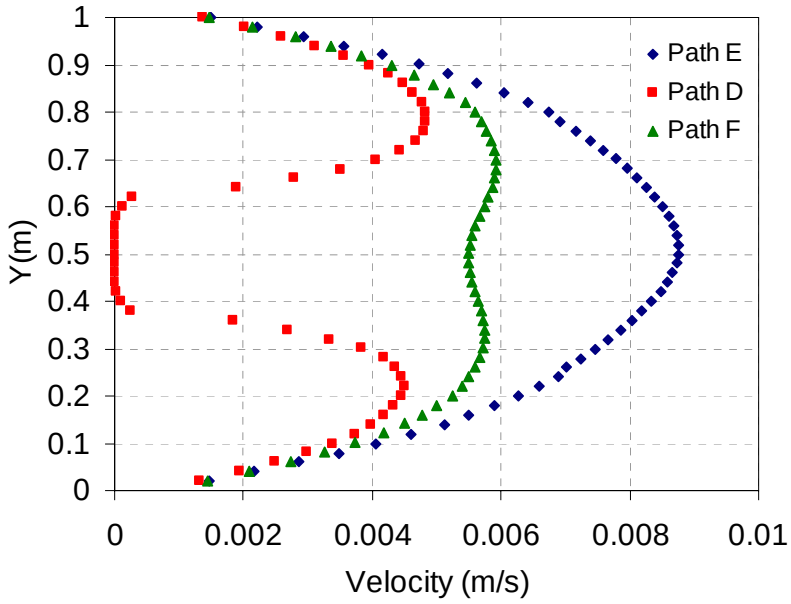

Fig. 4. 59: Flow velocity profile along paths E, F and D at time t = 12 s

The spatial distribution of the flow velocity, the second invariant of the strain tensor and the shear stress is depicted for 3 time intervals corresponding to t = 1 s, t = 6 s and t = 12 s. To respect the essence of the SPH method, the spatial distribution uses a discrete color representation for each particle.

Figures 4.60, 4.61 and 4.62 illustrate the simulated spatial distribution of the flow velocity, second invariant of the strain tensor and shear stress around the pile respectively. In all the figures, the wraparound effect of the periodic boundary is clearly observed.

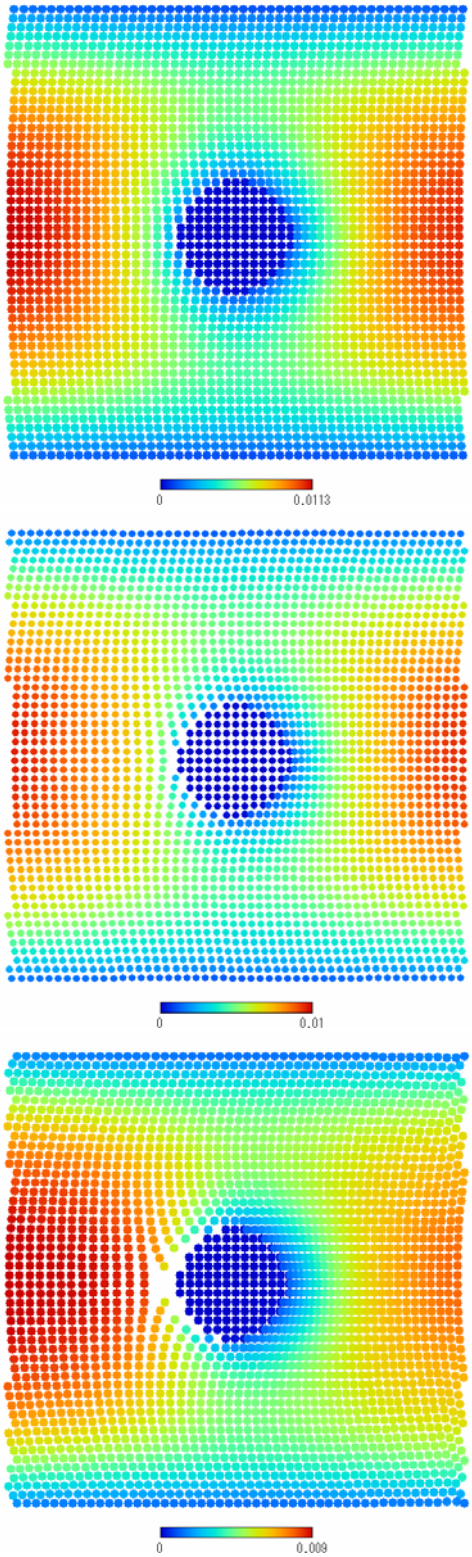

(a) t = 3 s

(b) t = 6 s

(c) t = 12 s

Fig. 4. 60: Flow velocity distribution around the pile at t = 3 s, t = 6 s and t = 12 s respectively

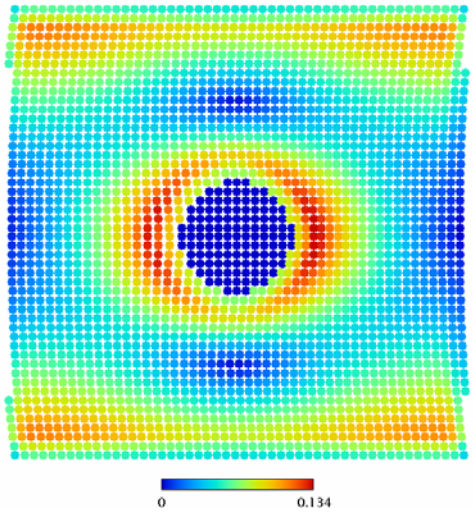

(a) t = 3 s

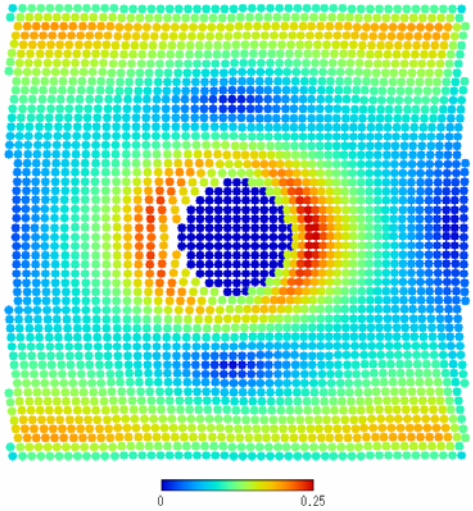

(b) t = 6 s

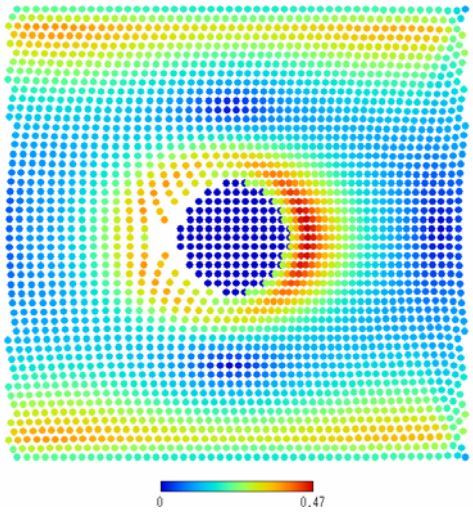

(c) t = 12 s

Fig. 4. 61: Distribution of the second invariant of the strain tensor around the pile at t = 3 s, t = 6 s and t = 12 s respectively

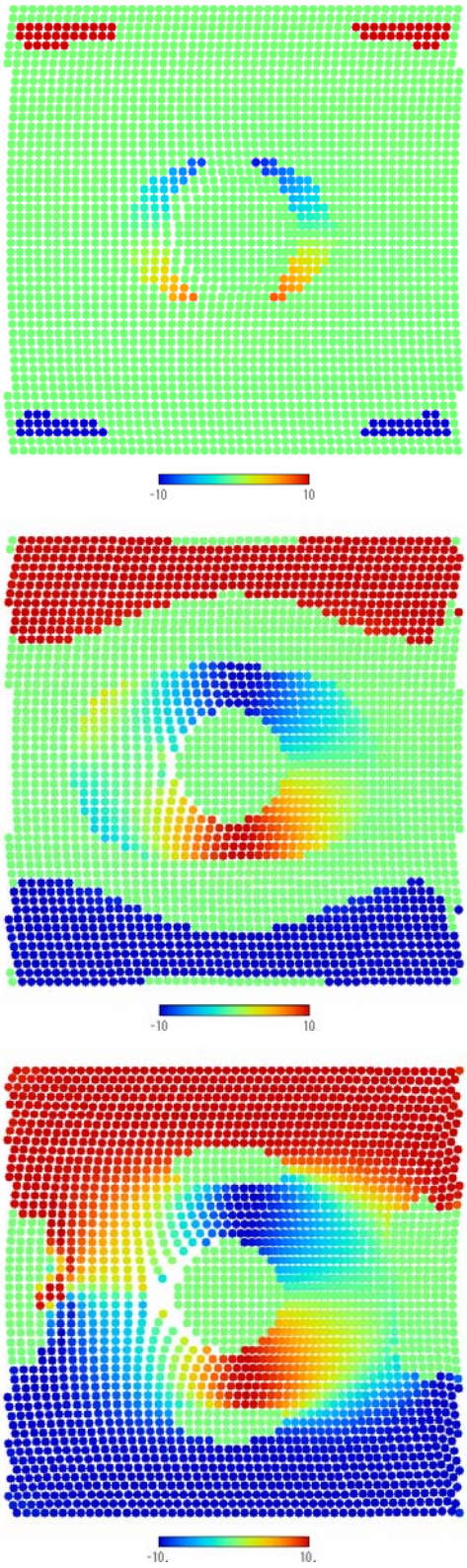

(a) t = 3 s

(b) t = 6 s

(c) t = 12 s

Fig. 4. 62: Shear stress distribution around the pile at t = 3 s, t = 6 s and t = 12 s respectively

Fig. 4.60 illustrates the flow velocity distribution profile along the channel for three respective time span. The maximum flow velocity is of the order of 1 cm/s as it is observed in the upstream and downstream regions at the center of the channel or near the equator as termed in the fluid mechanics terminology. Near the boundary, the velocity is almost negligible. Near and around the pile, the velocity is almost negligible since it corresponds to the yielded zone.

Fig. 4.61 depicts the spatial distribution of the shear strain along the channel. Starting from t = 3 s, the progressive increase of the shear strain near the boundaries and the pile is clearly observed. The maximum induced shear strain is 47% which is similar to the value computed during the lateral spreading simulation performed in Section 4.3 for Case 1. This result is also in accordance with physical testing and other numerical simulations using FEM approach showing the same tendency near the wall and around the cylinder, e.g., Zisis and Mitsoulis (2002).

Fig. 4.62 illustrates the distribution and time evolution of the induced shear stress. Starting from an unyielded profile at t = 3 s, the progressive occurrence of the yield zone is well observed as long as the induced shear stress is smaller than the Bingham yield stress or the minimum undrained shear strength. The maximum shear stress is observed near the boundary wall and around the pile. At the stationary regime, a polar cap around the pile and an island are clearly distinguished.

2. Simulation taking into account the recovery of the rigidity

The previous simulation confirmed the ability of the SPH method to simulate the flow of a liquefied soil around a model pile. The obtained results were qualitatively consistent with physical testing as well as other numerical simulations using FEM. In this section, the constitutive bilinear model for the recovery of rigidity will be introduced to simulate the flow of a liquefied soil around the model pile. In this respect, slightly larger parameters than that used in section 4.3.4 will be applied in this section. They are as follow:

$$\gamma_c = 10\%$$

$$A = \eta_y = 0.10 \text{ Pa·s}$$

$$B = 1.1 \times 10^{5}$$

$$C = -1.1 \times 10^{4}$$

Similarly to the previous results, the spatial distribution of the flow velocity, shear strain and shear stress along the channel are given for the same time points at t = 3 s, t = 6 s and t = 12 s respectively.

Figures 4.63, 4.64 and 4.65 illustrate respectively the simulated spatial distribution of the flow velocity, shear strain and shear stress around the pile taking into account the recovery of the rigidity.

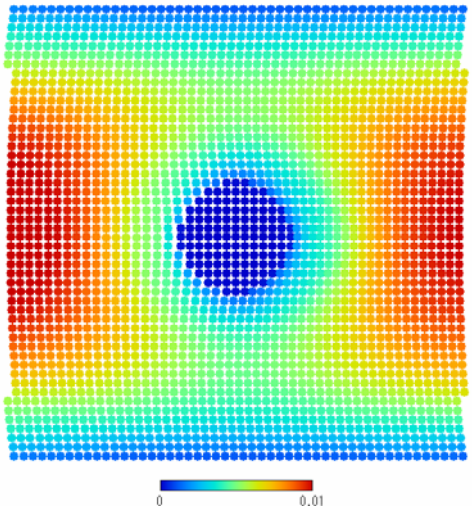

(a) t = 3 s

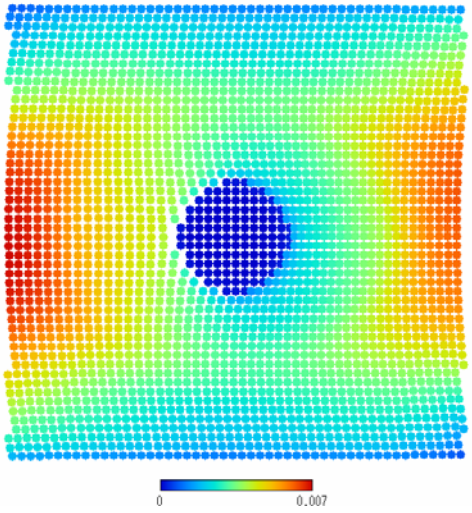

(b) t = 6 s

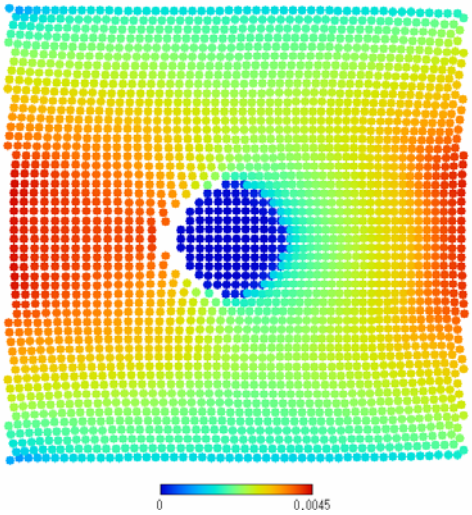

(c) t = 12 s

Fig. 4. 63: Flow velocity distribution around the pile at t = 3 s, t = 6 s and t = 12 s respectively

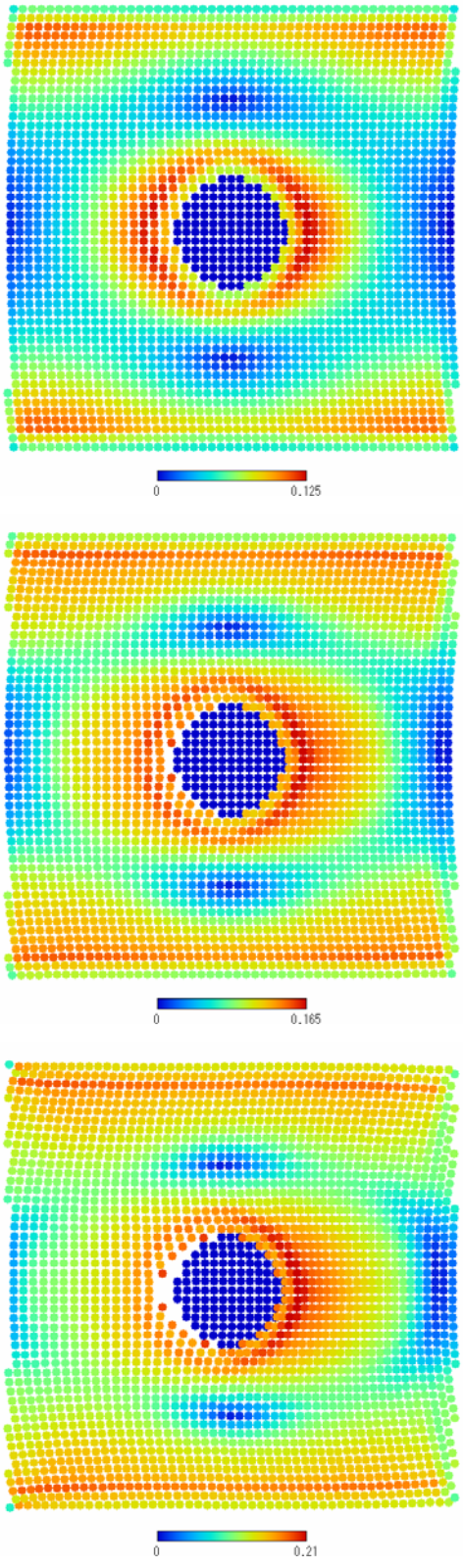

(a) t = 3 s

(b) t = 6 s

(c) t = 12 s

Fig. 4. 64: Distribution of the second invariant of the strain tensor around the pile at t = 3 s, t = 6 s and t = 12 s respectively

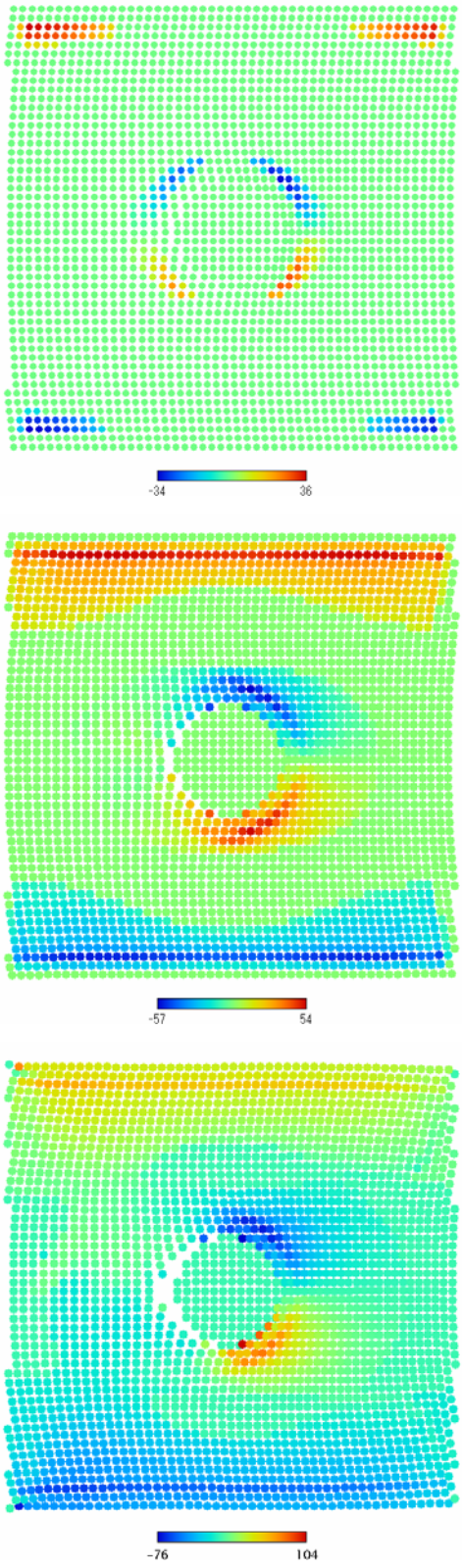

(a) t = 3 s

(b) t = 6 s

(c) t = 12 s

Fig. 4. 65: Shear stress distribution around the pile at t =3 s, t = 6 s and t = 12 s respectively

Fig. 4.63 depicts the flow velocity distribution along the channel at three respective times. The profile of the velocity in the upstream region suggests that the soil starts regaining its rigidity gradually. In fact, the maximum flow velocity of 1 cm/s at t = 3 s decreases sharply and becomes half of the maximum value at t = 12 s. Similarly the spatial distribution of the shear strain is shows in Fig. 4.64. It is clearly observed that the level of the shear strain is lower compared to the case where the recovery of rigidity was not modeled. Moreover, the magnitude of the strain decreases by about half when considering the regain of the stiffness: it is only 25 % compared to 47 % at t = 12 s for the previous simulations. Unlike the previous simulation, the spatial distribution of the shear stress do not exhibits any yielding/unyielding regions since the maximum induced shear stress at t = 3 s is larger than the minimum undrained shear strength. This is confirmed by plotting the shear stress distribution at t = 1 s as shown in Fig. 4.66, and allow us to state that the liquefied soil regained its rigidity between t = 1 s and t = 3 s.

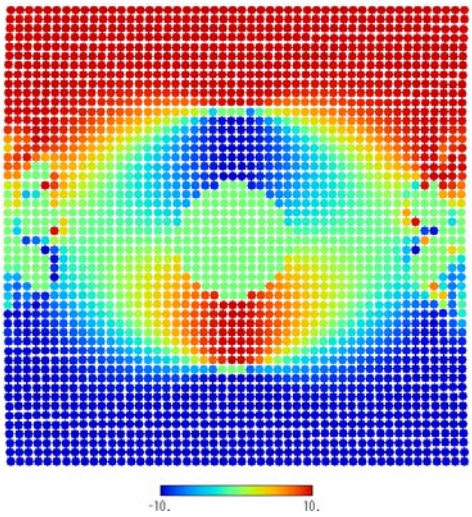

Fig. 4. 66: Shear strain distribution around the pile at t = 1 s

3. Summary of the simulations results

In this section, numerical simulations of the flow characteristic of the liquefied soil around a model pile were carried out on the basis of the experimental setup used by Hamada et al. (1992) in their investigation of the applied lateral load on an embedded model pile foundation.

In this respect, two type of numerical simulation were performed by considering and disregarding the recovery of rigidity. If the recovery of rigidity is not accounted for, the obtained results are similar to a viscoplastic flow around a pile, which is materialized by the appearance of the yielding/unyielding zone. The results resemble qualitatively to those published by Zisis and Mitsoulis (2002) using the FEM approach.

The bilinear model considering the recovery of the rigidity so far introduced in Section 4.4 was used to simulate the regain of the soil stiffness and confirm some of the statements regarding the sensitivity of the model on the wall boundary. The simulated results showed clearly that the velocity profile distribution depends on the intensity of the induced shear strain and shear stress. In this particular case, the maximum flow velocity and maximum shear strain was almost half of those obtained in the case without considering the rigidity recovery. As for the shear stress distribution, the appearance of the yielding/unyielding zone is observed as long as the shear strain is smaller than the critical shear strain. Beyond the critical shear strain, the soil recovers its rigidity and the induced shear stresses are larger than the minimum undrained shear strength.

Chapter 5

Conclusion and perspectives

5.1 Summary of the obtained results

This research deals with the analysis of liquefaction induced lateral ground displacement using Smoothed Particle Hydrodynamics (SPH) in the framework of fluid dynamics.

Because liquefaction induces large displacement and large shear strain that can not be simulated by ordinary methods (FEM, FDM), the primary objective of this research was to investigate the applicability and the feasibility of a Lagrangian meshfree particle method to simulate and analyze problems involving large ground displacements.

On the basis of field observations and laboratory tests findings on the mechanism of liquefaction induced lateral spreading and the nature of the liquefied soil, the viscous fluid analogy and the Bingham constitutive model was used to represent the behavior of the liquefied subsoil.

An existing educational SPH code was extended to model hydrodynamics problems involving material with strength.

The ability and the efficiency of the SPH code to simulate Newtonian and non-Newtonian flow was first checked using three benchmark problems for which exact solution and experimental results exist. These problems consist of a Poiseuille flow, a dam break of a water column and a water-clay mixture. The findings can be summarized as follow:

1. The SPH results obtained for the Poiseuille flow are in good agreement with the time series solutions derived by Morris.
2. The numerical instability during the simulation of the dam break problem of a water column was resolved using the artificial viscosity term. Since there are no clear rules on how to select the coefficients α and β introduced in the artificial viscosity term, a parametric study was conducted to find out the appropriate range without altering the physical phenomenon. It was concluded that provided smaller values of α and β are correctly selected, the numerical scheme is stable and the results fit the experimental observation. An appropriate range for β can be taken between 0.1 and 3 if α is to be neglected, or between 0.1 and 1 if α is accounted for. In general, since the physical viscosity is already there, the term α can be omitted as it brings additional viscosity to the problem.
3. Similar parametric study was conducted for the dam break flow of a water-clay mixture by considering the artificial viscosity terms as well as the XSPH technique proposed by Monaghan. The XSPH seems to have some physical meaning with respect to the SPH essence, and thus deserved further investigation in the framework of this study. The results suggest that the parameter ε of the XSPH is to be chosen in the range 10^{-3} to 10^{-2} for this particular case. On the other hand, if α is to be included in the artificial viscosity expression, then the additional viscosity is clearly perceptible, and hence should be disregarded. In this respect values between 0.1 and 1 for β seem to give good results.
4. The quintic spline kernel function derived by Morris was used. It was found that a smoothing length 0.9 to 1.2 times the initial spacing between the particles gives sufficient number of particles (20 to 30) to perform the averaging without smoothing out the particles physical quantities.
5. A typical value of sound speed between 1/10 and 1/75 of the actual sound speed of water constrains the density fluctuation within 1% if the velocity of the problem can not be predetermined. If the velocity is known through

exact solutions, a value equals to 1/10 the Mach number constrains the density fluctuation within 1%.

6. For problems involving wall boundaries, the density continuity approach is preferred to the summation density approach.

The SPH method was then extended to simulate the liquefaction induced lateral ground displacement.

The main results can be summarized as follow:

1-1– Numerical simulation of lateral spreading experiment performed by Hamada and Wakamatsu.

- The method reproduced the general trend of the observed free surface to a certain extent, particularly at the upstream and downstream region. At the central part, the surface did not keep the same inclination as the initial surface but rather experienced a slight rotation in the upstream. In the downstream, the free surface keeps the same inclination as the initial surface.
- The maximum ground flow velocity at depth h = 3 cm is well close to the experimental result in all the simulated cases. However, the velocities at the bottom part were overestimated and the liquefied soil continues flowing with a rate ranging between 1/20 and 1/30 of the maximum velocity. Similarly, the general trend of the time history of the ground displacement was simulated at the beginning of the simulation only in Case 3 whether the recovery of the rigidity is taken into account or not. However, the magnitude of the simulated displacement was larger than the observed one.
- The simulated induced shear strain rate lies within a comparable range with respect to the value obtained by Hamada and Wakamatsu.
- The distribution of the displacement along the height at the central cross section is consistent by the introduction of the recovery of rigidity. At the beginning of the simulation the displacement profile

looks like a ¼ of a sinusoidal wave; as the soil regains part of its rigidity, the distribution moves towards a triangular one.

- The distribution of the maximum displacement was also computed at three elevations at three different positions and compared with experimental results. The obtained results are close to the observed one with an acceptable confidence.
- On the basis of these findings along with the results of the gravity flow of a water-clay mixture, the discrepancy of the results may be attributed to the wall effect and particularly to the nature of the boundary particle represented by Lennard-Jones potential.

1-2– Numerical simulation of the flow velocity with respect to the liquefied layer thickness and ground slope gradient.

- The SPH simulations confirmed the similitude law proposed by Hamada and Wakamatsu for the liquefied soil.
- The flow velocity is proportional to the square root of the liquefied layer thickness.
- The time required for the liquefied soil to reach the maximum flow velocity is a function of the square root of the liquefied layer too.

1-3– Numerical simulation of the liquefied flow around a model pile.

- When the recovery of the rigidity is not taken into account, the flow of a liquefied soil around a model pile is equivalent to a typical viscoplastic flow around a cylinder placed in the middle of parallel plates.
- The appearance of the yielded/unyielded zone is well materialized by the SPH simulation. The results resemble qualitatively to those published by Zisis and Mitsoulis (2002) using FEM approach.
- The maximum value of the ground flow velocity is observed at the center of the channel.
- The model pile is subjected to high strains and stresses at the polar caps in the upstream region.

- By introducing the bilinear constitutive model for the recovery of the rigidity, both the magnitude of the velocity and the shear strain decrease as the soil regains its rigidity.
- The development of the yielded/unyielded zone is only observed when the induced shear strain is smaller than the minimum undrained shear strength.
- Since the simulation uses the periodic boundary, the effect of the wall is not observed and the recovery model leads to a consistent qualitative results.

5.2 Perspectives

This research work investigates the applicability and the feasibility of the SPH method to simulate the lateral ground displacement induced by liquefaction. The approach represents a promising tool for the simulation of the problem involving large displacement and large strain. Even though a simple constitutive model for the behavior of the liquefied soil and for the recovery of the rigidity was considered, the simulated results were consistent to a certain extent with the experimental findings. However in the present state, the method needs more improvement to be applied to real problems. The following aspects deserve further investigations:

- Clear criteria on the consideration of the artificial viscosity or the XSPH technique to stabilize the numerical scheme.
- Simulations of the dissipation of the pore water pressure by considering the fluid-solid phase in the framework of SPH to improve the recovery of the rigidity.
- Further investigations on the boundary wall effect and the necessity to represent the boundary particles with a potential other than Lennard-Jones.
- Extension of the SPH to treat solid material and hence assess the drag force acting on a model pile induced by the flow of the liquefied soil.

REFERENCES

1. Aydan O, Mechanical and numerical modelling of lateral spreading of liquefied soil. *Proc.1st Int Conf on Earth-Geo Eng, Tokyo 881-886,* 1995.
2. Bartlett, S.F, Youd, T.L, Empirical prediction of liquefaction-induced lateral spread, *Journal of Geotechnical Engineering*, Vol. **121**(4), 316-329, 1995.
3. Benz, W, Asphaug, E, Simulation of brittle solids using smooth particle hydrodynamics, *Computer Physics Communications*, **87**, 253-265, 1995
4. Doi, M.and Hamada, M., A summary of Case Studies on Liquefaction-induced Ground displacements, Proc. 4th US-Japan workshop on Earthquake Resistant Design of Lifeline Facilities and Countermeasures against Soil liquefaction, Technical report NCEER 92-0019, 115-129, 1994.
5. Gingold, R.A, Monaghan, J.J, Smoothed particle hydrodynamics: Theory and Application to Non-Spherical stars, *Monthly notices of the Royal Astronomical Society*, Vol.**181**, 375-389, 1977.
6. Hadush S, Yashima A., Uzuoka R , Importance of viscous fluid characteristics in liquefaction induced lateral spreading analysis, *Computers and Geotechnics*, **27**, 199-224,2000
7. Hamada H., Sato H., Kawakami T., A consideration of the mechanism for liquefaction-related large ground displacement. *Proc. 5th US-Japan workshop on Earthquake Resistant Design of Lifeline Facilities and Countermeasures against Soil liquefaction, Technical report NCEER 94-0026, 217-232, 1994.*
8. Hamada H., Ohtomo, K, Sato, H., Iwatate, T., Experimental study of the effect of liquefaction-induced ground displacement on in-ground structures. *Proc. 4th US-Japan workshop on Earthquake Resistant Design of Lifeline Facilities and Countermeasures against Soil liquefaction, Technical report NCEER 92-0019, 481-492, 1992.*
9. Hamada, M. and Wakamatsu, K., A study on ground displacement caused by soil liquefaction, *Journal of Geotechnical Engineering, JSCE,* III-43(596),189-208,1998
10. Hamada, M., Isoyama, R, Wakamatsu, K., Liquefaction-induced ground displacement and its related damage to lifelines facilities, *Special issue of Soils and Foundations*, 81-97,1996
11. Hamada, M., Yasuda, S., Isoyama, R, Emoto, K., Study on liquefaction induced permanent ground displacement. Published by the Association for the Development of Earthquake Prediction in Japan, p87, 1986
12. Inagaki, H., Susumu, I., Sugano, T., Yamazaki, H., Inatomi, T., Performance of caisson type quay walls at Kobe port, *Special issue of Soils and Foundations*, 119-136,1996

13. Ishihara, K., Liquefaction and flow failure during earthquake, *Géotechnique*, Vol. **43**(3), 351-415, 1993.

14. Kawakami T., Suemasa N., Hamada H., Sato H.,Katada T., Experimental Study on Mechanical Properties of Liquefied Sand. *Proc. 5th US-Japan workshop on Earthquake Resistant Design of Lifeline Facilities and Countermeasures against Soil liquefaction, Technical repor*t *NCEER 94-0026,* 285-299, 1994.

15. Kawakami F., Asada A., Damage to the ground and earth structures by the Niigata earthquake of June 16, 1964. *Soils and Foundations,* Vol. **6**, p14, 30, 1966.

16. Komatina D., Jovanovic M, Experimental study of steady and unsteady free surface flows with water-clay mixtures. *J of Hydraulic research, **35**(5), 579-590,* 1997.

17. Lucy, L.B, A Numerical approach to the testing of the fission hypothesis, *Astronomical Journal*, Vol.**82**(12), 1013-1024, 1977.

18. Lui, G.R, Liu, M.B, Smoothed Particle Hydrodynamics, World Scientific Publishing, 2003.

19. Miyajima, M, Kitaura, M, Koike, T, Hasegawa, M, Experimental study on characteristics of liquefied ground flow, *Proc.1st Int Conf on Earth-Geo Eng, Tokyo* 969- 974, 1995

20. Maeda, K, Sakai M., Development of seepage failure analysis procedure of granular ground with Smoothed Particle Hydrodynamics method, *Journal of Applied Mechanics*, JSCE, Vol.**7**, 775-786, 2004

21. Monaghan J.J., Simulating free surface flows with SPH. Journal *of Computational Physics*, **110**, 399-406, 1994.

22. Monaghan J.J., On the problem of penetration in particle methods, *Journal of Computational Physics*, **82**, 1-15, 1989

23. Monaghan J.J., Kocharyan A., SPH simulation of multi-phase flow, *Computer Physics Communications*, **87**, 225-235, 1995

24. Morris, J.P, Fox, P.J., Zhu, Y., Modeling low Reynolds Number Incompressible flows using SPH, *Journal of Computational Physics*, **136**, 214-226, 1997.

25. Naili, M, Matsushima, T, Yamada, Y., Numerical simulation of liquefaction induced lateral ground displacements using smoothed particles hydrodynamics, *Proc of 2004 convention of the Japan Association for Earthquake Engineering,* 400-401, 2005

26. Nishimura, S, Towhata, I, Honda, T., Laboratory shear tests on viscous nature of liquefied sand, *Soils and Foundations*, Vol. **42**(4), 89-98, 2002.

27. Newmark, N.M, Effect of earthquakes in dams and embankments, 5th Rankine lecture, *Géotechnique*, Vol.**15** (2), 139-159, 1965.

28. Orense, R, Towhata., Prediction of liquefaction-induced permanent ground displacements: A three dimensional approach, Proc. 4th US-Japan workshop on Earthquake Resistant Design of Lifeline Facilities and Countermeasures against Soil liquefaction, Technical report NCEER 92-0019, 335-349, 1994.

29. Randles P.W., Libersky L.D, Smoothed particle hydrodynamics: Some recent improvements and applications. *Comput Methods Appl Mechanics Engrg, 139-375,* 1996.

30. Rauch, A.F, EPOLLS: An Empirical Method for Predicting Surface Displacements Due to Liquefaction-Induced Lateral Spreading in Earthquakes, PhD thesis, Virginia Polytechnic Institute, pp 332, 1997

31. Saomoto H., Experimental observation and direct simulation of particle-fluid system, PhD thesis, University of Tsukuba, pp142, 2004.

32. Sasaki Y, Towhata I., Tokida K., Yamada K, Matsumoto H., Tamari Y., Shoichi S, Mechanism of permanent displacement of ground caused by seismic liquefaction. *Soils and Foundations, **32**(3), 79-96,* 1992.

33. Tamate S, Towhata I., Numerical simulation of ground flow caused by seismic liquefaction, *Soil Dynamics and Earthquake Engineering*, **18**, 473-485, 1999.

34. Towhata I, Material Properties of Liquefied Sand Undergoing Shaking and Large Deformation, *US-Japan Workshop on Seismic Disaster Mitigation In Urban Area By Geotechnical Engineering* 2002.

35. Towhata I, Vargas-Monge, W, Orense, R.P, Yao, M, Shaking table tests on subgrade reaction of pipe embedded in sandy liquefied subsoil, *Soil Dynamics and Earthquake Engineering*, **18**, 347-361, 1999

36. Towhata I., Sasaki Y.,Tokida K., Matsumoto H., Tamari Y., Yamada K, Prediction of permanent displacement of liquefied ground by means of minimum energy principle. *Soils and Foundations, **32**(3), 97-116,* 1992.

37. Uzuoka R., Yashima A.,Kawakami T.,Konrad J.M.,Fluid dynamic based prediction of liquefaction induced lateral spreading. *Computers and Geotechnics, **22**(3/4), 243-282,* 1998.

38. Yamada, G., Damage to earth structures and foundations by the Niigata earthquake of June 16, 1964. *Soils and Foundations*, Vol. **6**, 1-13, 1966.

39. Yasuda S., Nagase H.,Kiku H.,Uchida Y, The mechanism and a simplified procedure for the analysis of permanent ground displacement due to liquefaction. *Soils and Foundations, **32**(1), 149-160,* 1992.

40. Yasuda S., Yoshida N., Masuda T., Nagase H., Mine K., Kiku H.,.Stress-strain relationship of liquefied sand, *Proc.1st Int Conf on Earth-Geo Eng, Tokyo* 811-816, 1995

41. Zisis Th., Mitsoulis E., Viscoplastic flow around a cylinder kept between parallel plates, *J. Non-Newtonian Fluid Mech.*, 105, 1-20, 2002

42. Zhu, Y., Fox, P.J., Morris, J.P, A Pore scale numerical model for flow through porous media, *Int. J. Numer. Anal. Meth.Geomech*, **23**, 881-904, 1999

LIST OF PUBLICATIONS

Refereed journals

- M.Naili, T.Matsushima, Y.Yamada, 2005, "A 2D Smoothed Particle Hydrodynamics method for liquefaction induced lateral spreading analysis". *Journal of Applied Mechanics, JSCE,* Vol. **8**, pp 591-599.

Refereed conferences

- M.Naili, T.Matsushima, Y.Yamada, 2005, "Liquefaction induced lateral ground displacement: numerical investigation using SPH". *Proc of the 11th International Conf on Computer Methods and Advances in Geomechanics, Vol. **3**, pp 289-296.*

Non refereed journals/conferences

- M.Naili, T.Matsushima, Y.Yamada, 2005, "Smoothed particles hydrodynamics for numerical simulation of soil-structure problem due to liquefaction". *Proc of the* 40th *Convention of JGS, pp2257-2258.*
- M.Naili, T.Matsushima, Y.Yamada, 2005, "Numerical simulation of liquefaction induced lateral ground displacements using smoothed particles hydrodynamics". *Proc of the 2004 convention of the Japan Association for Earthquake Engineering, pp* 400-401.